Synthesis and characterisation of conductive metal-organic framework materials

A thesis submitted for the degree of Doctor of Philosophy

Yu Wang

St. Catherine's College

Department of Materials, University of Oxford

Hilary Term 2025

Preface

The work described in this thesis was carried out by the author, under the supervision of Prof. Martin R. Castell, at the Department of Materials, University of Oxford, from October 2020 to April 2025. All the work is original and has not been previously submitted for any degree or qualification at this university or any other institute of education. Where the work of other researchers is drawn upon, it has been referenced and acknowledged. Parts of the work described in Chapters 4, 5, 6, and 7 have been presented at international conferences and/or published in peer-reviewed journals as follows:

Conferences

Yu Wang, Abigail M. Lister, and Martin R. Castell. ‘‘Orientation-dependent gas sensing behaviour of $Cu_3(HHTP)_2$ MOF film”, **7th Annual UK Porous Materials Conference**, Liverpool, UK., 2024. (Oral)

Yu Wang, Abigail M. Lister, and Martin R. Castell. “Orientation-dependent gas sensing behaviour of $Cu_3(HHTP)_2$ MOF film”, **1st Mediterranean conference on porous materials**, Crete, Greece., 2023. (Poster)

Yu Wang, Abigail M. Lister, and Martin R. Castell. “Electrochemically synthesized oriented $Cu_3(HHTP)_2$ thin film as Chemiresistive gas sensor”, **8th International Conference on Metal-Organic Frameworks and Open Framework Compounds (MOF2022)**, Dresden, Germany., 2022. (Poster)

Approximate word count of this thesis: 40,000 words.

Acknowledgments

Firstly, I would like to express my deepest gratitude to my supervisor, Professor Martin Castell, for his continuous support, insightful advice, and patient guidance throughout my DPhil. I deeply appreciate every conversation with him, through which I learned to think more rigorously as a scientist. I am especially grateful for his mentorship in developing critical thinking, an invaluable skill that has helped me address my weaknesses in research.

I would also like to thank my friends and colleagues from the Surface Nanoscience group. I am lucky to be in such a friendly and supportive environment. Thanks to Abi, for her guidance at the start of my DPhil and for all the things we began to explore together. I thank Weishuo for the many scientific discussions we shared, and for encouraging me through a difficult time. I am also grateful to Tairu, Liren, Axel, Sparsh, and Runze for their support and friendship.

I'm incredibly lucky to have shared this journey with my family, Yi, for all the laughter, tears, and memories; for her trust and for never judging.

I am beyond grateful to have Kate by my side, and for all the butterflies. My courage has grown because of her presence in my life, and I thank her for joining me in this adventure.

Finally, I owe my deepest thanks to my mom, for giving me life and her love, and for everything we've been through together.

The past is but a prologue to all that is yet to come, and I'm grateful that tomorrow is always another day.

Abstract

Electrically conductive metal-organic frameworks (MOFs) have emerged as a promising new class of materials for use in applications ranging from organic electronics to chemical sensing. However, integration of MOFs into functional devices remains limited in part because of a variety of synthesis and processing challenges. For example, the growth of large oriented MOF crystals is difficult, and there are substantial challenges in creating MOF nanoparticle suspensions. In this thesis novel synthesis strategies are reported that enable control of the morphology, orientation, and processability of conductive MOFs. The application of these materials as chemiresistive gas sensors is investigated, and their paramagnetic spin activity is explored. These findings contribute to the broad goal of advancing the fundamental understanding of these new electrochemically-grown materials with a view to integrating them into novel electronic devices.

An electrochemical deposition strategy was developed to fabricate highly oriented $Cu_3(HHTP)_2$ MOF films on ITO glass using a dual-working-electrode approach. A systematic investigation into the electrochemical synthesis mechanism reveals how ligand concentration and synthesis conditions influence film orientation. This method enables precise control over crystal orientation, which directly impacts charge transport behaviour. The anisotropic electrical conductivity of these films was analysed.

Electrochemically-grown oriented $Cu_3(HHTP)_2$ films were used as the active material in chemiresistive gas sensors. By selecting the film orientation the sensors were optimised for

ammonia detection with a limit of detection in the parts-per-billion (ppb) range. A direct correlation between MOF film structure and sensing response is shown. Structural and spectroscopic analyses (XRD, XPS, and FT-IR) before and after gas exposure provide insights into gas adsorption and charge transport mechanisms.

To improve the processability of MOFs for scalable device fabrication, two solution-based synthesis methods were developed: a modulator-assisted and a surfactant-based approach. Highly dispersible $Cu_3(HHTP)_2$ nanocrystals with morphology control were created. These solution-processable conductive MOFs were successfully deposited onto interdigitated electrodes via spray-coating, yielding good gas sensing behaviour.

Finally, the thesis describes experiments on redox-state tuning in MOFs. A 3D conductive MOF (Cu-DBC) was synthesized, where electrochemical oxidation-state modulation induces the formation of organic radicals. Pulsed electron paramagnetic resonance (EPR) measurements reveal spin characteristics with long spin-lattice relaxation times.

Contents

Preface **2**
Acknowledgments **3**
Abstract **4**
1. Introduction **9**
2. Literature review **13**
2.1 Introduction 13
2.2 Two-dimensional conductive metal organic frameworks 14
2.2.1 Design strategies of 2D MOFs 14
2.2.2 Introduction to HXTP-based 2D MOFs and their analogues 15
2.2.3 Redox-active properties of HXTP 19
2.3 Synthetic control of 2D MOFs 22
2.3.1 Solvothermal synthesis and device integration of 2D MOFs 22
2.3.2 Solution-processable synthesis of conductive MOFs 24
2.3.3 Thin film synthesis methods 27
2.3.4 Orientation Control in 2D MOF films 30
2.3.5 Future directions 33
2.4 Chemiresistive sensing of 2D MOFs 35
2.4.1 Chemiresistive sensors 35
2.4.2 Conductive MOFs as active material for chemiresistive sensors 36
2.4.3 Sensing mechanisms 38
2.5 EPR of MOFs 41
2.5.1 EPR characterization of MOFs 41
2.5.2 Design of MOFs towards long phase memory time 43
2.5.3 Incorporation of organic radicals in MOFs 47
2.6 Summary 50
3. Methodology **53**
3.1 Materials 53
3.2 Synthesis and deposition methods for conductive MOFs 54
3.2.1 Solvothermal synthesis of conductive MOFs 54
3.2.2 Electrochemical synthesis of conductive MOFs 54

3.3 Sensing chamber setup 56
3.4 Characterisation techniques 58
3.4.1 Electron microscopy 58
3.4.2 Atomic force microscopy 58
3.4.3 X-ray diffraction 59
3.4.4 UV-Vis-NIR spectroscopy 61
3.4.5 X-ray photoelectron spectroscopy 62
3.4.6 Fourier-transform infrared spectroscopy 62
3.4.7 Electron paramagnetic resonance spectroscopy 63
3.5 Summary 65
4. Orientation control of 2D MOFs 66
4.1. Introduction 67
4.2. Experimental section 68
4.2.1. Solvothermal synthesis of $Cu_3(HHTP)_2$ powder 68
4.2.2. Electrochemical synthesis of $Cu_3(HHTP)_2$ film 68
4.2.3. Cyclic voltammetry measurements 69
4.3. Results and discussion 69
4.3.1 Electrochemical synthesis using a dual-working-electrode setup 69
4.3.2 Orientation control 76
4.3.3 Oriented growth mechanism 81
4.3.4 Investigation of anisotropic conductivity and surface chemistry 87
4.4. Conclusion and outlook 89
5. Sensing behaviour of oriented films 91
5.1 Introduction 92
5.2 Experimental section 93
5.2.1 Fabrication of oriented MOF film-based sensors 93
5.2.2 Sensing experiments 93
5.3 Results and discussion 94
5.3.1 Synthesis and Characterization of oriented MOF films 94
5.3.2 Chemiresistive gas sensing performance of oriented film 96
5.3.3 Interaction mechanisms between ammonia and MOF film 102
5.4 Conclusion and outlook 107
6. Solution-processable MOF nanomaterials for chemiresistive gas sensing 109
6.1 Introduction 111

6.2 Experimental section 114
6.2.1 $Cu_3(HHTP)_2$-Cat MOF preparation 114
6.2.2 $Cu_3(HHTP)_2$-PVP MOF preparation 114
6.2.3 Characterization 115
6.2.4 Spray-coating process for gas sensor fabrication 115
6.2.5 Sensing experiments 116
6.3 Results and discussion 117
6.3.1 Modulator-assisted synthesized $Cu_3(HHTP)_2$-Cat 117
6.3.2 Fabrication and performance of $Cu_3(HHTP)_2$- gas sensor 123
6.3.3 Surfactant-assisted morphology Control of $Cu_3(HHTP)_2$-PVP 125
6.3.4 Fabrication and performance of $Cu_3(HHTP)_2$-PVP sensor 131
6.3.5 Comparative discussion of $Cu_3(HHTP)_2$-Cat and $Cu_3(HHTP)_2$-PVP 133
6.4 Conclusion and outlook 135
7. EPR Studies of a Cu-DBC MOF 136
7.1 Introduction 137
7.2 Experimental section 139
7.2.1 Solvothermal synthesis of Cu-DBC 139
7.2.2 Electrochemical synthesis of Cu-DBC 139
7.2.3 General characterization 140
7.3 Results and discussion 140
7.3.1 Synthesis and Characterization 140
7.3.2 The charge state of Cu 144
7.3.3 Spin dynamic behavior 147
7.4 Conclusion and outlook 151
8. Summary and future look 153
8.1 Conclusions 153
8.2 Future outlook 155
References 158

Chapter 1

Introduction

Metal-organic frameworks (MOFs) are porous crystalline materials composed of inorganic nodes and organic linkers. Their high surface area and modular chemical functionality have made them attractive candidates for a broad range of applications, imcluding hydrogen and methane storage, gas separation such as carbon dioxide, hydrogen, and methane, and catalysis, such as the carbon dioxide reduction reaction.[1-2] However, their integration into electronic devices has been limited by their inherently low electrical conductivity. This limitation was overcome through the discovery of electrically conductive MOFs.[3-5] These materials are typically constructed by coordinating metal centres with planar π-conjugated ligands bearing chelating functional groups. The resulting 2D π-d conjugated planes stack via interlayer π-π interactions, creating extended charge transport pathways both within the layers and along the stacking direction. In addition, some non-planar π-conjugated ligands have been reported to form three-dimensional conductive MOFs. In both cases, the extended conjugation plays a critical role in enhancing electrical conductivity. Furthermore, some of these conductive MOFs incorporate paramagnetic metal centres and unpaired electron on the ligands, offering a combination of porosity, conductivity, spin activity, and modularity. As a result, they are increasingly being investigated for applications in electronics and spintronics.[6-8]

The functional performance of conductive MOFs is highly dependent on their structural features, particularly morphology, stacking orientation, and particle size. Understanding the relationship between structure and function is essential for optimising their integration into devices. Synthetic control over film structure is therefore critical. Moreover, the redox state of metal centres and ligands plays a central role in determining the spin properties of these materials.

This thesis addresses these challenges by developing synthesis strategies to control the morphology, orientation and processability of conductive MOFs and by investigating how these factors influence their electronic and spin-related properties. This is achieved through the fabrication and characterisation of chemiresistive sensing devices and the application of pulsed electron paramagnetic resonance (EPR) spectroscopy.

The thesis begins with a literature review focused on extended conjugation MOFs, examining their structural and electronic properties. It then introduces various synthesis methods for MOF film deposition and discusses how these influence material characteristics. The structure-property relationships of electrically conductive MOFs are explored as active materials in chemiresistive sensors, along with a review of relevant sensing mechanisms. Finally, the chapter investigates the presence of paramagnetic metal centres and organic radicals in modulating MOF behaviour, and how factors such as metal-ligand combinations and synthesis conditions affect radical formation.

Chapter 3 outlines the materials and experimental techniques used throughout the thesis, including solvothermal and electrochemical synthesis methods, sensor fabrication protocols, and characterisation techniques such as X-ray diffraction (XRD), scanning and transmission electron microscopy (SEM, TEM), X-ray photoelectron spectroscopy (XPS), and EPR.

Chapter 4 introduces an electrochemical method for directly depositing 2D MOFs onto interdigitated electrodes. A dual-working-electrode setup was developed, which enabled control over film orientation. By tuning the ligand concentration in the electrolyte, both face-on and edge-on orientations of $Cu_3(HHTP)_2$ films were achieved. This structural control enables investigation of anisotropic charge transport and surface chemistry.

Chapter 5 explores the orientation-dependent sensing performance of $Cu_3(HHTP)_2$ films. Edge-on films demonstrated enhanced sensitivity for ammonia detection in the part-per-billion (ppb) range, while face-on films exhibited comparatively weaker responses. These results underscore the importance of film orientation in determining sensor effectiveness and gas-MOF interactions.

Chapter 6 describes a solvothermal synthesis method to produce solution-processable conductive MOF nanomaterials. The use of modulators and surfactants enabled control over crystal size and morphology, resulting in stable suspensions suitable for spray-coating. The resulting films demonstrated fast and reversible responses to ammonia, confirming the suitability of these nanomaterials for scalable sensor fabrication.

Chapter 7 focuses on the redox modulation of a three-dimensional conductive MOF, Cu-DBC. Electrochemical synthesis was used to generate ligand-centred radicals, and the resulting spin dynamics were investigated using pulsed EPR. Measurements of spin-lattice relaxation times confirmed room-temperature coherence, revealing how redox state tuning can modulate spin properties in conductive MOFs.

Chapter 8 concludes the thesis by summarising the main findings and discussing their implications. The results demonstrate that structural and redox control can be used to tune the

electronic and spin behaviour of conductive MOFs. Finally, the chapter outlines several promising directions for future research.

Chapter 2

Literature review

2.1 Introduction

Metal-organic frameworks (MOFs) are porous materials consisting of organic linkers and inorganic nodes, offering extensive chemical tunability and high surface area. These properties make MOFs promising for applications including gas storage, separation, and catalysis.[9-10] However, their application in electronic devices has been limited by their inherent low conductivity.[3, 9] Conductive two-dimensional MOFs have been developed by coordinating metal centre with planar π-conjugated linker consisting of chelating functional group to form 2D d- π conjugation planes, these planes are then assembled through interlayer π- π interactions.[5, 11-12] The resulting extended π-conjugation facilitates charge carrier delocalization throughout the 2D plane and the stacking direction, thereby enhancing electrical conductivity. Additionally, full conjugation within the redox-active ligand enables the delocalization and stabilization of unpaired electrons.[5, 13] Combining the electrical conductivity, spin centres, permanent porosity, and chemical modubility, two-dimensional extended conjugation frameworks have been explored as active materials in electronics and spintronics.[14]

In this thesis, various synthesis methods have been explored to control the structure of 2D MOFs and to understand their structure-property relationships. This chapter discusses the relevant progress achieved in this area. The first part reviews existing studies on the structural, electronic, and redox properties of 2D MOFs. This is followed by an introduction to various

synthesis routes for fabricating 2D MOFs and a discussion on how these synthetic methods influence their structural and electronic properties. In the third part, the application of these 2D MOFs as active materials for chemiresistive gas sensors is introduced, alongside synthesis methods for optimizing their performance. Then studies on the host-guest interactions between 2D MOF films and gas molecules are discussed. The final section demonstrates the spin properties of these MOFs, arising from the paramagnetic metal centres and the presence of stable organic radicals, which enables the investigation of their spin dynamics properties.

2.2 Two-dimensional conductive metal organic frameworks

2.2.1 Design strategies of 2D MOFs

The high intrinsic conductivity in MOFs is generally achieved based on through-bond and through-space strategies.[5] For through-bond strategy, charge transport occurs through the metal and the ligand functional group within the porous framework.[5] This strategy requires well-matched energy levels and good orbital overlap between metal and ligand, which can lead to small band gaps and increased charge mobility.[3, 5] The through space strategy allow charge moves through non-covalent interactions, such as π-π stacking between organic ligands.[3, 5, 15]

Combining these two strategies, some of 2D extended conjugation-based MOFs exhibits the highest conductivity among MOFs. As a special case of the through-bond strategy, the charge delocalization through the ligand backbone is essential for extended conjugation pathway.[5, 15] This strategy involves coordinating transition metals with ligands containing chelating groups and are conjugated with the organic core to achieve fully d-π conjugation in the ab plane. These 2D sheets are then stacked by π- π interaction to form 3D structures. As shown in Figure 2.1, the resulting layered materials have anisotropic in-plane and out-of-plane interactions. A single crystal study has reported that both π-d conjugation within the ab plane and the π-π stacking

cross plane serve as charge transport pathway, resulting in high conductivity.[16] However, most reported studies focus on the conductivity within the ab plane, only a few studies investigated the charge transport through the stacking direction.[17] The anisotropic charge transport pathways in 2D MOF films affect their conductivity and device performance, providing valuable insights into the structure-property relationship.[9, 16, 18]

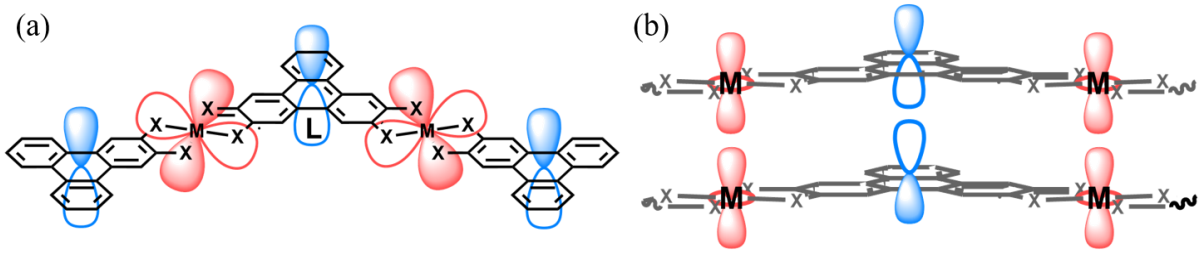

Figure 2.1: Schematic diagram of (a) through-bond and (b) through-space charge transport pathways. Red orbitals represent the metal-centred orbitals, and blue orbitals represent the ligand-centred orbitals.

2.2.2 Introduction to HXTP-based 2D MOFs and their analogues

One promising ligand for investigating the structure-property relationships of these 2D MOFs is hexa-substituted triphenylene (HXTP), including 2,3,6,7,10,11-hexahydroxytriphenylene (HHTP), 2,3,6,7,10,11-hexaaminotriphenylene (HATP), and triphenylene-2,3,6,7,10,11-hexathiol (HTTP).[4, 12] These functional groups are capable of stable d-π conjugation with transition metals forming planar M-X_4 (X= NH, O, S) subunits. In this family of layered MOFs, each layer possesses honeycomb lattice structure with hexagonal pores, these layers are held together by π-π interaction along the c axis. These MOFs can be categorized into two types based on their structures.[19] The first type is only based on 2D extended layers with chemical structure of $M_3(HXTP)_2$ (Figure 2.2a). The second type includes intercalated molecular complexes that are rotated 60° relative to the extended layer (Figure 2.2b), resulting in an overall chemical structure of $M_9(HHTP)_4$.[5, 12, 19]

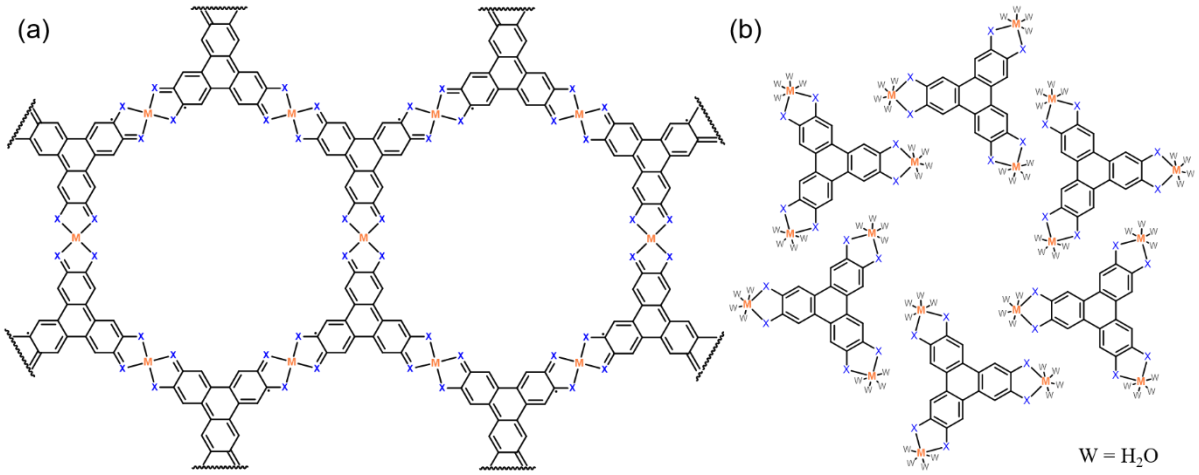

Figure 2.2: Structures of HXTP-based 2D MOFs with the representation of (a) extended single layer and (b) intercalated complexes. M can be Co^{2+}, Ni^{2+}, Cu^{2+}, Zn^{2+}, or Mg^{2+} ions. X represents the –OH, -NH_2, or -SH corresponding to HHTP, HATP, or HTTP, respectively.

In 2012, Hmadeh et al. reported the first 2D MOF by reacting the HHTP with Co^{2+}, Ni^{2+}, and Cu^{2+}.[12] The resulting MOFs characterized using high-resolution transmission electron microscopy (HR-TEM), powder X-ray diffraction (PXRD), and single crystal XRD. These results have shown that Co^{2+} and Ni^{2+} form the same crystal structure, each metal atom is coordinated to two HHTP linkers forming honeycomb lattice in the first layer with the formula $M_3(HHTP)_2(H_2O)_6$, with intercalating units of $M_3(HHTP)(H_2O)_{12}$, leading to overall chemical structure of $M_9(HHTP)_4$ (M=Ni, Co).[5-6] While each Cu^{2+} was found coordinating two linkers in a square planar for every layer, leading to chemical structure $Cu_3(HHTP)_2$. Both the Co/Ni and Cu based HHTP MOF structures have a near-eclipsed stacking mode, where the layers are almost perfectly aligned, with interlayer space ranging from 0.31nm to 0.33 nm.[5, 12, 16] The exfoliation of $Cu_3(HHTP)_2$ particles yields thin flakes and rods, enabling direct observation of structural details through HRTEM characterization (Figure 2.3). The HRTEM image of $Cu_3(HHTP)_2$ flakes reveals a clear hexagonal crystalline structure, and the image of $Cu_3(HHTP)_2$ rods shows an interlayer distance of 0.31nm with a continuous stacking offset.[16]

Among these three MOFs, the conductivity of pressed pellet for $Cu_3(HHTP)_2$ was measured to be 0.1 S/cm, which was the highest value from MOFs.[12]

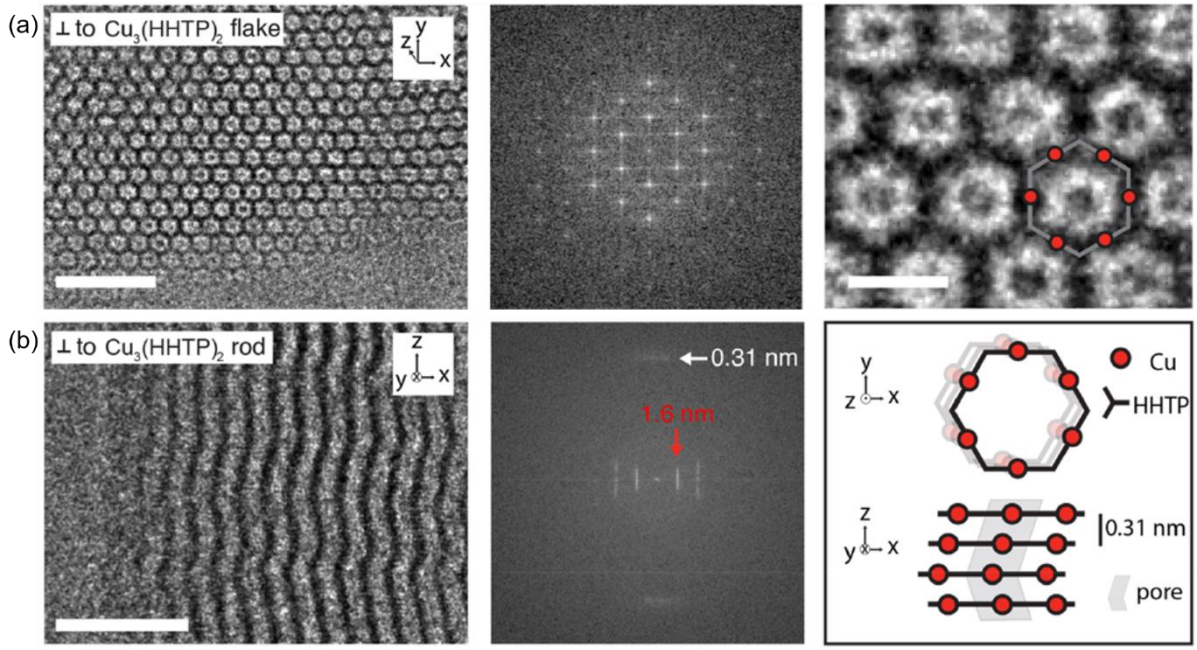

Figure 2.3: TEM images showing the crystalline structure of $Cu_3(HHTP)_2$ along the extended layer and stacking direction. (a) Left: TEM image of $Cu_3(HHTP)_2$ flakes. Middle: FFT from the left image. Right: HRTEM image of the porous structure. (b) Left: HRTEM image of the $Cu_3(HHTP)_2$ rod. Middle: FFT from left image. Right: Schematic of $Cu_3(HHTP)_2$ crystal structure showing the near-eclipsed stacking arrangement. Adapted from Reference 14.

Further research on HHTP has shown that coordination with Mg^{2+} and Ga^{3+} results in structures identical to $Ni_9(HHTP)_4$ and $Co_9(HHTP)_4$, while $Zn_3(HHTP)_2$ is isostructural with $Cu_3(HHTP)_2$.[20-22] Studies on HITP and HTTP-based MOFs indicate that $M_3(HITP)_2$ and $M_3(HTTP)_2$ (M=Cu, Ni, or Co) are isostructural with $Cu_3(HHTP)_2$.[4, 11] Apart from HXTP ligands, various triphenylene-based (HXTP) building blocks and their derivatives have been developed to build the 2D frameworks, such as hexahydroxybenzene (HHB), HHTP, 2,3,8,9,14,15-hexahydroxytrinaphthylene (HHTN), and dibenzo[g,p]chrysene-2,3,6,7,10,11,14,15-octaol (DBC) (Figure 2.4).[6, 23-24] The influence of the ligand size on the pore size and conductivity of resulting MOF was revealed by Meng et al.[25] The authors

synthesized $Cu_3(HHB)_2$, $Cu_3(HHTP)_2$, and $Cu_3(HHTN)_2$ with increased size of the ligand (Figure 2.4 a-c), resulting in an increasing pore size of 1.1 nm, 1.8 nm, and 2.5 nm, respectively. The $Cu_3(HHTN)_2$ exhibited electrical conductivity of 9.01×10^{-8} S/cm, which is lower than $Cu_3(HHTP)_2$, due to the weaker orbital interaction between Cu^{2+} and organic ligand and the large free void space in the ab plane. For the same ligand, the metal centre influences the interlayer stacking distance. For example, $Ni_3(HITP)_2$, $Cu_3(HITP)_2$, and $Co_3(HITP)_2$ possess an interlayer distance of 3.23, 3.16, and 3.29 Å, respectively.[26] $Cu_3(HHTP)_2$ and $Zn_3(HHTP)_2$ shows interlayer spacing of 3.18 and 3.13 Å, respectively.[27] More recently, non-planar aromatic ligands with catechol units, such as DBC, have been developed to introduce diverse properties and pore types in conjugated frameworks (Figure 2.4d). When coordinating with Cu, these ligands form three-dimensional MOFs, but they are also classified within the 2D MOFs family due to their extended metal-linker conjugation.[28-29]

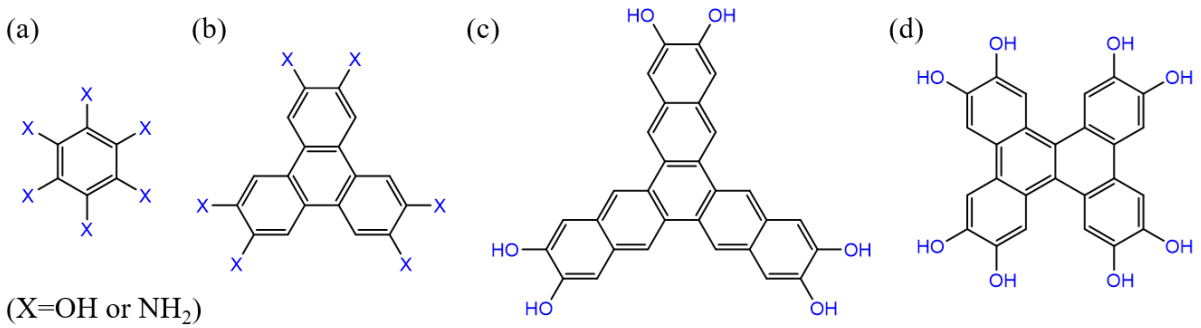

Figure 2.4: Structures of a series of analogous hexa-substituted conjugated ligands capable of forming d-π conjugated MOFs (a) HXB (b) HXTP (c) HHTN (d) DBC.

The layered anisotropic crystal structure of HXTP-based MOFs leads to intrinsic anisotropic charge transport pathways.[30] Day et al. measured the in-plane and cross-plane conductivity of $Cu_3(HHTP)_2$ using four-probe devices fabricated using electron-beam lithography.[16] Thin hexagonal flakes and needle shaped structure $Cu_3(HHTP)_2$ were exfoliated to measure the

conductivity in both in-plane and out-of-plane direction. The cross-plane conductivity was reported as 1.5 S/cm, stressing the importance of π-π stacking in the conductivity of 2D MOFs.

2.2.3 Redox-active properties of HXTP

The linkers discussed above in extended frameworks are based on conjugated organic core and redox-active chelating groups such as *ortho*-catechol, -phenylenediamine, and –dithiolbenzene groups. Each can undergo a reversible catecholate-semiquinonate-quinonate (cat-sq-q) redox sequence (Figure 2.5). As a result, valence tautomerism has been observed and explored in catechol-transition metal complexes.[31] The fully reduced catechol (Cat) and radical-containing semiquinone (SQ) states are the most common mode of coordination with Cu to form $Cu^{2+}(Cat^{2-})$ and $Cu^{+}(SQ^{\cdot -})$ complexes.[32] Though the fully oxidized quinone (Q) state is a weak donor and can be subjected to defects, especially in 2D MOFs, it has been reported that Cu^{+}(Q)-based complexes and MOF can be stabilized by $\pi - \pi$ interactions.[31, 33-35] The favoured form between Cu and catechol, along with its valence tautomeric transition depends on various parameters including ligand structure, temperature, and the presence of oxidants such as oxygen.[32, 34, 36-37] During this process, Cu itself can oxidize catechol-based-ligands and reduce quinone-based-ligand in an oxygen free atmosphere.[38-39] A similar electron transfer process was observed for other metal-catechol complexes such as cobalt and manganese.[31]

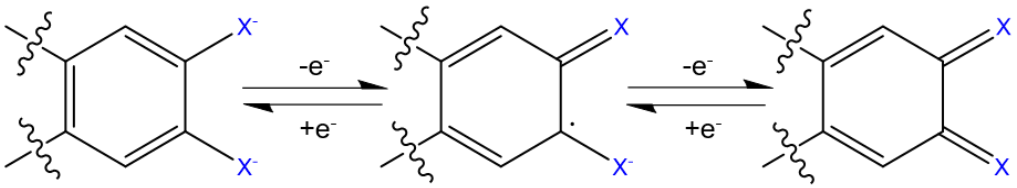

Figure 2.5: Redox state of 2- (catechol), 1- (semiquinone), and 0 (quinone) charge states of a deprotonated catechol structure. The black dot marks the possible radical location.

In principle, the three catechol arms of HHTP lead to seven oxidation states after deprotonation, ranging from fully reduced $HHTP^{6-}$ to the fully oxidized $HHTP^{0}$ state (Figure 2.6).[40] The charge state of HHTP can be affected by the coordinated metal. For example, the oxidation state of HHTP in $Co_9(HHTP)_4$ and $Mg_9(HHTP)_4$ was assigned to be -3 and -6 for the first layer and the intercalated complexes to maintain charge neutral, both Co and Mg are at +2 state. While $Cu_3(HHTP)_2$ possesses $HHTP^{3-}$ and Cu^{2+}. When HHTP coordinates with Fe, it constructs 3D MOFs with Fe at mixed valence state of +2 and +3, and HHTP in the -6-oxidation state.[41]

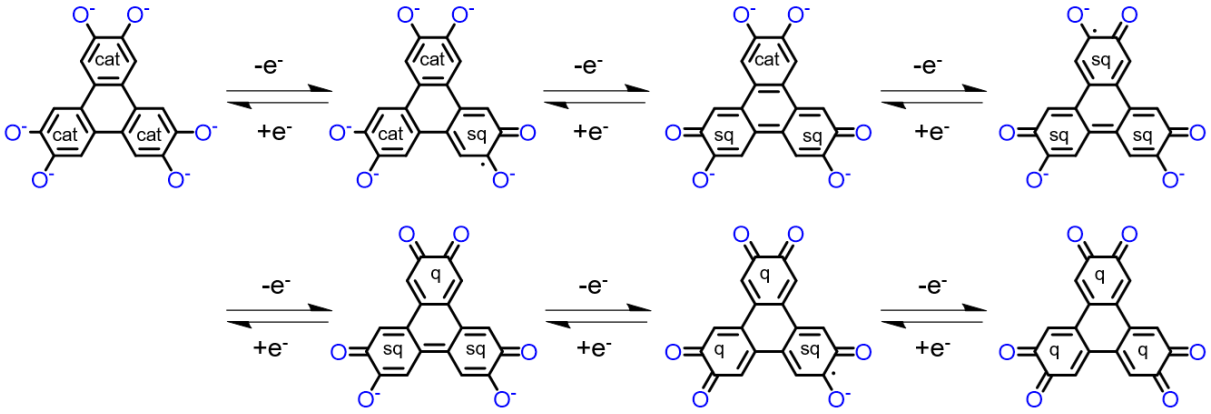

Figure 2.6: Redox sequences of deprotonated HHTP from fully reduced state [cat, cat, cat]$^{6-}$ to fully oxidized state [q, q, q]^{0}, with each site formal oxidation level labelled.

Recent experimental results from XPS and XANES spectra have indicated the presence of both Cu^{2+} and Cu^{+} in $Cu_3(HHTP)_2$.[42-43] Misumi et al. reported the existence of Cu^{+} as due to defects in $Cu_3(HHTP)_2$, which they suggest may not change the main spin characteristics of $Cu_3(HHTP)_2$.[42] Campbell et al. found that XPS result of $Cu_3(HITP)_2$ shows two types of copper. The authors excluded the presence of Cu metal based on the absence of Cu metal peak in PXRD data, suggesting a mixed valence state of Cu in $Cu_3(HITP)_2$. However, Chen et al. demonstrated that the synthesis of $Cu_3(HITP)_2$ containing only Cu^{2+} can be achieved using an improved synthesis approach.[26] Another argument suggests that Cu^{+} came from further oxidation of

catechol-based ligands by Cu^{2+}.[43-46] For example, Jiang et al. found that Cu metal is reduced from Cu^{2+} by catechol-based ligand when formed in argon.[44]

In addition, HXTP-based complexes have been isolated as the smallest unit to investigate the spin and electronic interaction in the 2D MOFs. Yang et al. demonstrated that only complex with Cu^{2+} and $HHTP^{3-}$ can be isolated for $Cu_3(HHTP)_2$ and $Cu_3(HITP)_2$.[47] HHTP with oxidation states -4, -3, and -2 can be isolated for Ni-HHTP based MOF, with no oxidation state change for Ni observed.[48] Evidence of Cu and Ni based metal-redox behaviour in 2D MOFs have rarely been proved. The metal-centred redox behaviour was observed along with ligand redox in complex $Fe_3(HPTP)_6$ and Co-HTTP, where HXTP is fully reduced at -6 state.[49-51]

These results indicate that the Cu^+ can be generated during coordination with HXTP due to the complicated redox process. However, in the final MOF structures, it is difficult to stabilize the Cu^+ as the metal node in the square planar structure. According to crystal field theory, the d^9 state in Cu^{2+} prefers a square planar coordination geometry, while the d^{10} state in Cu^+ prefers tetrahedral geometry.[31, 36] The presence of Cu^+, along with $HHTP^{2-}$ for charge neutrality in $Cu_3(HXTP)_2$, is highly likely to lead to a distorted structure and other defects in the square planar geometry, such as intralayer symmetry mismatch, and interlayer offset displacement.[52-53] Additionally, the presence of a high concentration of Cu^+ were observed in several Cu-based 2D MOFs, suggesting that Cu^+ may play a key role in enhancing conductivity.[34, 54-55] Investigation into defect engineering will provide insight into the formation of defects, their impact on the properties of MOFs, and enables developing strategies to control the defects. Using a combination of simulation methods, Debela et al. investigated the formation energies of hydrogenic defects in $Cu_3(HITP)_2$ and $Ni_3(HITP)_2$ and their effect on the electronic properties of the MOFs.[53] For the monolayer of $Cu_3(HITP)_2$, the authors found that the addition of extra

electrons are not likely responsible for the presence of Cu^{+}. However, experimental results related to compositional and structural defects in 2D MOFs remain unexplored.

2.3 Synthetic control of 2D MOFs

Due to the unique redox-active properties of these ligands and the anisotropic structure of the resulting MOF, synthesis methods significantly influence the material characteristics, including interlayer stacking distance, stacking orientation, morphology, crystallinity, domain size, oxidation state, and defect level.[14, 52-53] Therefore, this section emphasizes the synthetic control achieved during the growth process of conductive 2D MOFs.

2.3.1 Solvothermal synthesis and device integration of 2D MOFs

The first reported solvothermal synthesis of $M_3(HXTP)_2$ involved mixed metal salts and ligands in solution that were heated at 85°C to obtain the MOF powder.[12] It was found that the synthesis of catechol-based MOFs requiring a unique ligand oxidation step. Du et al. demonstrated solid-solid synthesis of $Cu_3(HHTP)_2$ and observed that $Cu_3(HHTP)_2$ cannot be formed in Ar, suggesting the critical role of oxygen.[39] Also, for the M-HITP (M=Ni, Cu, Co) MOFs, the presence of air during synthesis is critical.[26, 56] Jiang et al. found that Cu metal forms along with the catechol-based MOF when synthesis is in argon, suggesting that Cu ions can be reduced by HHTP when lacking oxygen.[44] However, the exact role of O_2 in the coordination process between Cu and HHTP remains unclear.

Solvothermal synthesis studies revealed that the morphology of HHTP-based MOFs can be tuned by incorporating additives.[12] Snook et al. employed oxidant additive 2,6-dimethy-1,4-lbenzoquinone (DBQ) to investigate the relationship between the oxidation state of HHTP and

morphology of $Cu_3(HHTP)_2$. By controlling the amount of the DBQ, the oxidation state of the ligand was tuned, rod, block and flake morphologies were achieved.[57] However, the exact mechanism of oxidized HHTP during the formation of $Cu_3(HHTP)_2$ with various morphologies was not fully understood.[57-59] The effect of other additives was further investigated, the addition of ammonia resulted in the formation of flake-like structures in $Cu_3(HHTP)_2$, while the introduction of DMF and pyridine led to rod and spherical aggregations, respectively.[58, 60] The authors proposed that these additives function as modulators during the solvothermal synthesis of $Cu_3(HHTP)_2$. However, the ammonia may also deprotonate the HHTP, which could contribute to the formation of the observed flake structure. Furthermore, the addition of these modulators not only changed the morphology, but also resulted in different phases. Compared to the addition of ammonia and pyridine, increased stacking offset was observed when $Cu_3(HHTP)_2$ was synthesized in the presence of DMF.[60] The resulting powders with flake-like structure show better capacitive performances than the rod and sphere like powders, probably due to the presence of short pores.[60]

The effect of deprotonation degree on the structure of 2D MOFs was investigated by Shan et al. on Cu-TBTT (TBTT= octahydroxyltetraphenylthieno[3,2-b] thiophene). The authors demonstrated that by controlling the degree of deprotonation, different topologies of the resulting MOF can be achieved. A 1D structure forms when ethanol and deionized water are used as solvent, while a 2D Kagome structure forms when using DMF, water and ammonia. This change in solvent conditions also affects the charge state of Cu, the 2D Kagome Cu-TBTT exhibits a higher ratio of Cu^+ compared to 1D Cu-TBTT, probably due to the rapid deprotonation and reaction.[61]

For the solvothermal synthesized MOF powders to be integrated into electronic devices, the MOF is dispersed in a solvent as a MOF suspension and then drop-cast on a desired substrate.

However, the large powder size of MOFs results in inhomogeneous film, aggregation of particles, and high crystal domain contact resistance, and poor contact resistance.[14, 59] Additionally, the intrinsic structural rigidity of MOFs leads to poor fluidity and processability, which limits their performance and industrial applications in electronics and membranes.[62] The challenge lies in achieving precise control over the morphology, crystal size, and thickness of the resulting film, and decreasing contact resistance between the rigid structure and the electrode for enhanced performance of the device.

2.3.2 Solution-processable synthesis of conductive MOFs

One straightforward solution is to develop solution-processable MOF crystals at the nanoscale. Compared to MOF powder suspension, the small crystal size of solution-processable MOF enables colloidally stable particles (Figure 2.7 a, b). After being left undisturbed for several days, sedimentation can be observed on the bottom of the vial for MOF powders, while the stable MOF colloid maintains its dispersity. When fabricated as a film, the bulk material shows voids between the electrode and the film, as well as between particle boundaries. In contrast, the solution-processable MOFs exhibit dense inter-particle packing and close film-electrode interface contact (Figure 2.7 c, d).[63] The solution-processable MOFs can be processed into a uniform film using various straightforward solution processing methods such as spin-coating and drop-casting. These MOFs with high specific surface areas, controllable size, and dense packing have shown potential in scalable production and enhanced performance in applications such as gas separation, chemiresistive sensing, and batteries.[64-66] Additionally, the solution-processable state of MOFs enables fundamental investigation such as spectroscopic analysis in the solution state, which remains relatively unexplored for conductive MOFs.[63]

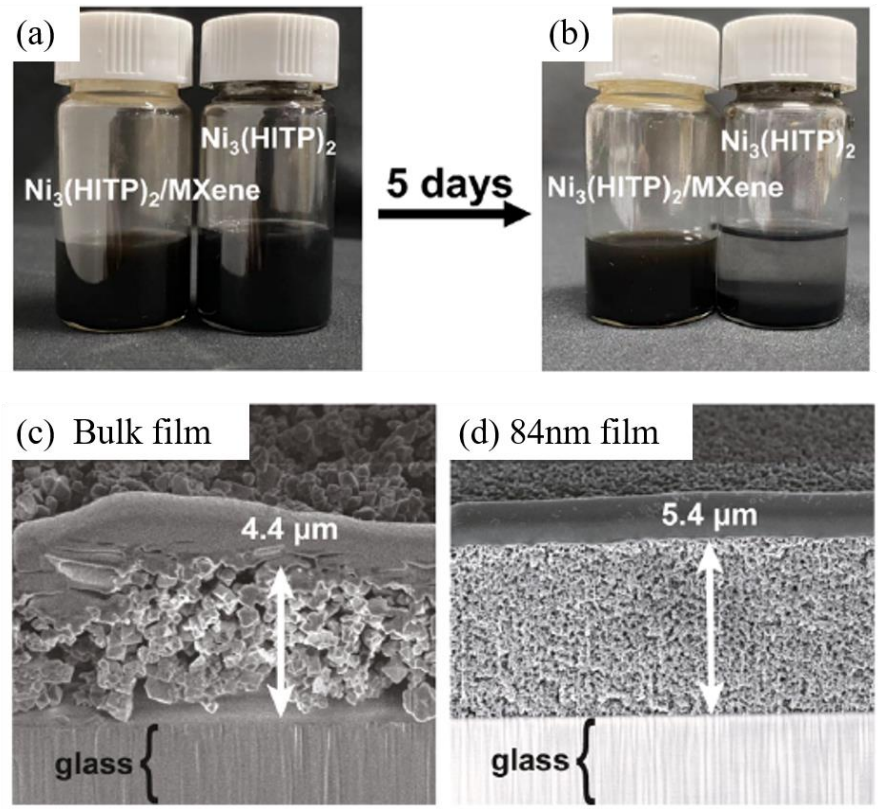

Figure 2.7: Optical photographs of $Ni_3(HITP)_2$/ MXene and $Ni_3(HITP)_2$ suspensions both (a) as-synthesized and (b) after being left at room temperature for five days with no visible sedimentation. Adapted from reference 64. FIB-SEM image of a cross-section of (c) $Fe(TA)_2$ bulk film (d) film from particle size of 84nm, showing dense packing. Adapted from reference 63.

Various strategies have been explored to achieve solution-processable conductive MOFs. Top-down strategies such as microwave exfoliation and centrifugation use extra energy to break weak interlayer interactions to obtain MOF nanosheets. Jo et al. obtained $Cu_3(HHTP)_2$ flakes of varied sizes through centrifugation.[67] By varying the centrifugation speed, they were able to produce supernatants composed of small flakes of $Cu_3(HHTP)_2$ ranging from 155 to 430 nm. The sensor fabricated using these nanoflakes showed higher response to NO_2 compared to the powder sample, likely due to the increased interaction sites between the gas and the MOF crystals. Although this method enables the separation of nanoscale flakes, it results in a low yield and uncontrollable thickness.

The bottom-up strategy aims to achieve control over the growth process of these solution-processable crystals via modifying the standard bulk synthesis methods, such as template-assisted strategy, surfactant-assisted synthesis, and modulator-assisted synthesis.[63-65] The addition of surfactant such as polyvinylpyrrolidone (PVP) and anionic sodium dodecyl sulfate (SDS) has proven to be an efficient strategy for limiting the growth of MOF crystals especially in the stacking direction.[59] PVP has been used to fabricate ultrathin MOF nanosheets by alleviating their stacking.[59, 68] The C=O group of PVP interacting with metal ions, capping, and adsorbing onto MOF planes. Wang et al. reported a method for synthesizing solution-processable 2D MOF nanosheets using SDS-assisted solution synthesis followed by sonication exfoliation.[65] This approach successfully produced Cu-HHTP, Cu-HHB, and Ni-HHB nanosheets with thickness of about 5 nm. However, a long sonication time is required for this method. Additionally, the SDS anion might act as counterion during the coordination between Cu and HAB, HATP, which leads to the electronic structure change of final product.[69] The crystal growth of MOFs along the *ab* plane can be regulated by the addition of modulators. Unlike long chain surfactants, modulators are small molecules that are typically monotopic analogues of the MOF ligands. Several molecules have been used as modulators, including pyridine, lauric acid, and 1-methylimidazole.[62-63, 66] These modulators facilitate bond formation with the metal nodes, competing with the metal-linker coordination and thereby influencing the directional growth and size of the MOF crystals.[62-63, 66] Marshall et al. reported a size-tunable synthesis method of Fe $(TA)_2$ (TA=1,2,3-triazolate) through the addition of 1-methylimidazole as modulator. By adjusting the amount of modulation, the crystal can be tuned from 5.5 nm to 130 nm. UV-vis spectroscopy results revealed that the electronic structure of $Fe(TA)_2$ changes with the particle size, enabling future insight into physical properties that are inaccessible in bulk materials.[63] Hard template methods enable precise morphology control depending on the choice of the templates. Very recently, solution-processable $Ni_3(HITP)_2$ using MXene (Nb_2C)

as nanosheets template was reported by Yuan et al.[64] These results have shown that the increased specific surface area leads to increased conductivity and improve sensor sensitivity. However, this method suffers from low purity of final product and inhomogeneous blending of the MOFs.

Despite their promising applications, this method still faces several challenges. The presence of additives limits purity and reduce active sites, while exfoliation methods offer only rough control over size and morphology. Furthermore, although the importance of size control has been demonstrated, research on solution-processable conductive MOF remains limited. Future research on developing synthetic strategies for improved purity and precise size control will enable the exploration of size-dependent properties in solution state and facilitate scalable synthesis for industrial applications.

2.3.3 Thin film synthesis methods

On the other hand, various in-situ deposition methods without drop-casting of 2D MOFs have been explored, including interfacial synthesis, layer-by-layer assembly, and electrochemical synthesis to produce high-quality MOF films. [70-79] Interfacial liquid-liquid surface synthesis involves dissolving the metal ions and organic ligands in two immiscible solvents, the MOF nanosheets can be formed at the interface.[79-80] This method enables formation of ultrathin film with high uniformity, but challenges lie in their weak crystallinity, limited size of the nanosheets, and complicated transfer process for device integration, which led to weak adhesion between electrode and the MOF. Layer-by-layer assembly can be classified as liquid-solid interface synthesis, which overcomes the limitation of MOF/electrode interface contact. Xu et al. demonstrated a spray layer-by-layer method to directly fabricate MOF film on the electrode (Figure 2.8a).[72] The substrate with an –OH functionalized surface was exposed to the solution

of metal salt and ligand alternatively. By tuning the spraying cycles, film with a thickness of 20 nm-100 nm can be achieved. This method requires polar reactants and functionalized substrates to ensure adsorption. Moreover, films obtained using this method show particle morphologies which are like bulk powders synthesized via solvothermal method, which might be due to the undirected interactions during the metal-ligand assembly process.[72, 81]

An emerging promising deposition method to fabricating high-crystallinity film directly on electrodes is electrochemical synthesis.[82-85] This method offers possibilities to achieve control over crystal size, film thickness, and reaction rate by modulating parameters including applied voltage, deposition time, and solution pH. For example, varying the applied voltage can tune the oxidation state and rate of the reactant. Electrochemical deposition of MOFs is usually conducted via a three-electrode setup and can occur at either the cathode or anode. Cathodic synthesis allows control over the ligand deprotonation, which has been employed for 3D non-conductive MOFs and Cu catecholate conducting MOFs. The underlying mechanism of cathodic electrosynthesis is generating hydroxide anions through the reduction of water or oxoanions. These generated HO- accumulate near the electrode surface, facilitating the deprotonation of ligands, and subsequent formation of MOFs on the electrode.[86-87] Several probases have been reported for the cathodic synthesis of MOFs, including nitrate anions (NO_3^-), triethylammonium (Et_3NH^+), water and oxygen.[87] Cathodic synthesis of $Cu_3(HHTP)_2$ film was developed by Li et al using O_2 as probase. However, only randomly oriented particles were observed.

Anodic deposition takes advantage of metal oxidation. When a voltage is applied on the anode, the metal starts to be oxidized to metal ions and react with the organic linker near the electrode surface. Liu et al. introduced an anodic approach wherein Cu ion was released from Cu foil, coordinating with ligands to form $Cu_3(HHTP)_2$ film on the Cu foil surface (Figure 2.8b). These

films exhibited a constrained thickness (~60 nm) and no specific orientation.[83] The anodic deposition of MOFs usually relies on anodic dissolution, which limits the choices of substrate, film thickness, and increase the risk of introducing metal oxides purity. To address this, Bradshaw et al. developed an anodic oxidation method, initially depositing a Cu layer onto a fluorine doped tin oxide (FTO) electrode, resulting in rod-like structures within the film.[77] However, the film thickness remains limited using this deposition method. Very recently, an electrochemical synthesis technique was reported, enabling precise control over the thickness of the face-on orientated $Cu_3(HHTP)_2$ films.[46] This method utilized copper salt, ligand, electrolyte and acid as precursor solution, with the oxidation state of the ligand was controlled by tuning the applied voltage and the pH of the precursor solution.

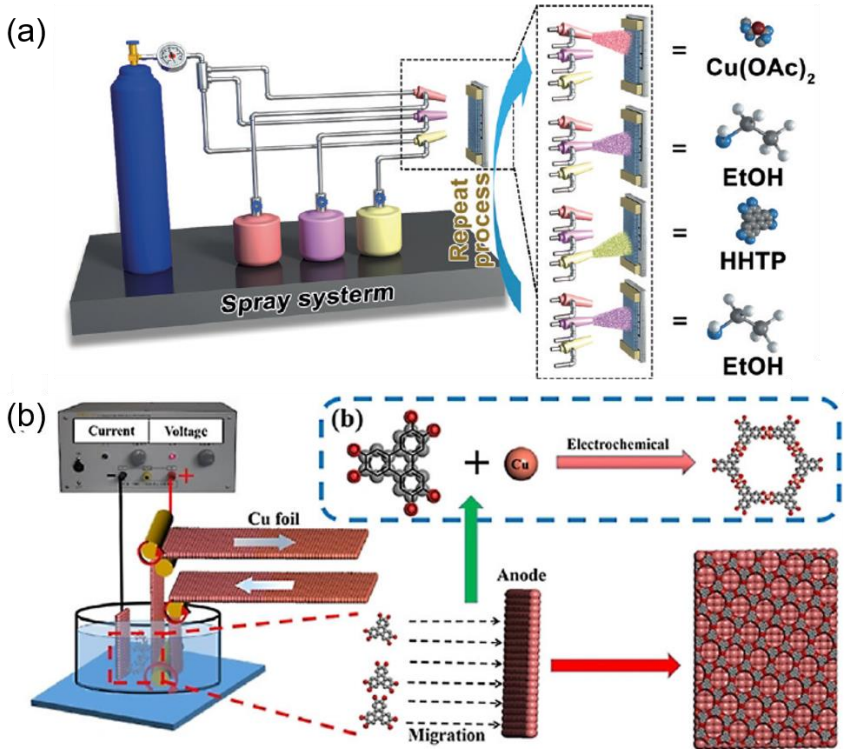

Figure 2.8: (a) Schematic illustration of the layer-by-layer fabrication process for $Cu_3(HHTP)_2$ thin-film gas sensors. Adapted from reference 72. (b) Electrochemical setup used for the deposition of a $Cu_3(HHTP)_2$ film on Cu foil. Inset: Schematic of the coordination reaction between Cu^{2+} ions and deprotonated HHTP ligands 76.

Despite progress in electrochemical synthesis, the exploration of its application for 2D MOF films remain limited. First, this strategy allows for control over the initial oxidation state of the metal and the ligand, which makes it highly promising for tuning the electronic and spin structures of MOFs. However, such control has not been achieved yet. Second, although one benefit of the electrochemical synthesis method is reported to be fast deposition at room temperature, the rapid electron transport and deprotonation often lead to random nucleation and growth of MOF particles on the electrode. Slowing down the reaction rate could enhance control over the deposition process. Third, developing new electrode setups that avoid the need for sacrificial anodes and could provide new insights into the application of this deposition method.

2.3.4 Orientation Control in 2D MOF films

Due to the structural anisotropy of 2D MOFs, charge transport pathway differs between the in-plane and out-of-plane directions, which makes it challenging to understand the structure-property relationship in these layered materials (Figure 2.9).[88] For example, chemical composition change in the HXTP family MOF can change interlayer stacking distances and offsets, which impact electronic and spin interactions in the out-of-plane direction. Establishing such correlations is challenging without orientation control. Additionally, when integrated into optoelectronic devices, their intrinsic anisotropic physical properties lead to different interaction with stimuli between of in-plane and out-of-plane direction. Therefore, exploring synthetic control on the orientation of 2D MOF films is essential for understanding on the structure-property relationship of these layered materials and achieve maximized device function.

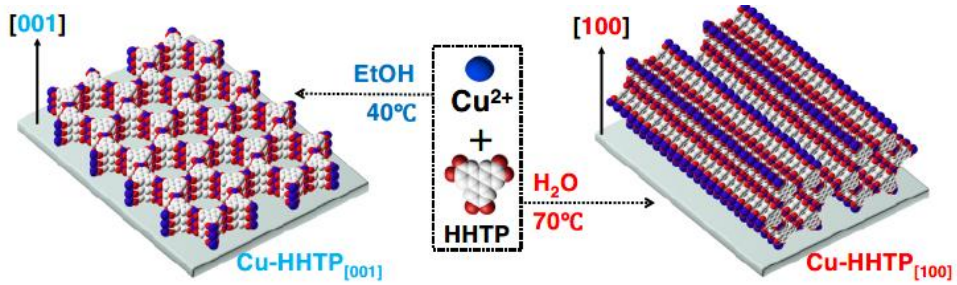

Figure 2.9: The schematic diagram showing the anisotropic structure of $Cu_3(HHTP)_2$ film. Adapted from reference [89].

Face-on HXTP-based MOF film has been reported achieved using vapour assisted conversion, electrochemistry synthesis, layer-by-layer method, and solid-liquid interface synthesis.[46, 84, 89-92] Mähringer et al. successfully synthesized face-on film of M-HHTP (M= Ni, Co, or Cu) using a vapor-assisted method.[90] They spread a solution containing metal acetate and HHTP ligand onto a substrate, then place it over a mixture of water and isopropanol solvents in a sealed vessel. The films were obtained after 3 hours heating at 85°C. The face-on orientation of M-HHTP (M= Ni, Co, or Cu) was achieved on a gold surface. However, when using ITO (Indium Doped Tin Oxide) as substrate, the MOF crystals tended to grow in the solution rather than directly on the substrate. To suppress the nucleation of MOFs in the solution, acetic or salicyclic acid was added to the precursor solution. Notably, only $Ni_9(HHTP)_4$ and $Co_9(HHTP)_4$ can be formed on ITO glass substrate. In contrast, large agglomerates of $Cu_3(HHTP)_2$ formed on ITO glass, indicating that the interaction between the metal centre and substrates is a key factor in this process. The formation of oriented $Cu_3(HHTP)_2$ may require different conditions compared to $Ni_9(HHTP)_4$. Chon et al. reported a pyridine vapor-assisted annealing method to achieve face-on orientation of $Cu_3(HHTP)_2$ on an α-Al_2O_3 (001) substrate.[91] In their method, the film was first deposited using infrared-pulse laser deposition, and then placed in a sealed cell containing pyridine in the air. The film was annealed at about 60°C for 24 hours, resulting in a face-on film on the substrate.

Shin et al. demonstrated a solid-liquid synthesis method for forming in-plane oriented $Ni_9(HHTP)_4$ nanorods at the solid-liquid interface on highly oriented pyrolytic graphite and copper.[92] This process involves dissolving HHTP and $Ni(OAc)_2$ in deionized water, followed by heating the mixture at 85°C for various time. The authors found that these nanorods became less ordered when the solvent was changed to a mixture of water and DMF, confirming the important role of solvent composition in the growth process of Ni-HHTP.[93]

An anodic synthesis method to was reported by Song et al. to achieve face-on orientation of $Cu_3(HHTP)_2$.[46] The precursor solution was initially prepared containing $Cu(NO_3)_2$, HHTP, nitric acid, and NaCl in a nitrogen saturated mixed solvent of DMF and water. The nitric acid suppressed the growth of MOF crystals in solution, while NaCl served as an electrolyte. By applying a potential voltage between 0.25 -0.35V (versus Ag/AgCl), face-on $Cu_3(HHTP)_2$ film were formed on substrates including gold, ITO, HOPG, and silicon, using an FTO (fluorine-doped tin oxide) counter electrode, after just 5 min. Cyclic voltammetry (CV) was used to investigate the electrochemical behaviour of $Cu(NO_3)_2$ solution, HHTP solution, and the precursor solution, providing insight to the anodic formation mechanism of $Cu_3(HHTP)_2$. For the ligand solution, three anodic peaks were observed at 0.35, 0.55, and 0.85V, which was assigned as one-electron-oxidation process of HHTP transitioning from CatCatCat to CatCatSq, and finally to SqSqSq, each corresponding to one subunit of the ligand.[46, 94] The authors suggest that the anodic formation of face-on $Cu_3(HHTP)_2$ may be related to the oxidation and deprotonation process of HHTP.

Edge-on films of 2D MOFs are less successfully synthesized compared to face-on films. One effective strategy for achieving edge-on orientation is to use the hydrophilic functional group, hydrophobic core of ligand, and π-π interaction between ligand and ligand. This approach can induce the ligand to stand upright on the surface the water and –OH functionalized ITO.[84, 89, 95]

Wang et al. achieved edge-on stacked $Cu_2[PcM{-}O_8]$ (M = Cu or Fe) 2D c-MOF films at an air-water interface.[95] Based on this principle, layer-by-layer synthesis was demonstrated as an effective way to control the orientation of $Cu_3(HHTP)_2$.[84, 89] Ma et al. synthesized $Cu_3(HHTP)_2$ films by sequentially immersing functionalized substrate in $Cu(OAc)_2$ and HHTP solution.[89] By changing the solvents and reaction temperature, edge-on and face-on film can be achieved. Specifically, face-on film was obtained using ethanol as solvent at 40°C, while edge-on film was synthesized using water as solvent and heating at 70°C. The thickness of the films was about 60 nm and 120 nm, respectively. Subsequently, a layer-by-layer spraying method was used to synthesize orientated Cu-HHTP film by tuning the ligand concentration. Results from molecule-level resolution frequency modulation atomic force microscopic (FM-AFM) revealed that when ultra-high ligand concentration were sprayed, the ligand tend to "stand-up".[84]

Another successful example is using chemical vapour deposition method to synthesize edge-on orientated $Cu_3(C_6O_6)_2$. Very recently, an on-liquid-gallium surface synthesis (OLGSS) method under chemical vapour deposition was reported for M-HHB and M-BHT (M=Cu, Ni, Co, Pd, V,and Pt) MOF.[96] Ultra flat (face-on) MOF film was observed on liquid Gallium substrate, while uneven (edge-on) film was observed on SiO_2 substrate. DFT simulation was carried out to investigate the adsorption energy and adhesion energy of ligand on SiO_2 and gallium surfaces. Results show that both adsorption energy and adhesion energy of Cu-BHT on the gallium surface are higher than that on SiO_2 surface.

2.3.5 Future directions

Apart from these synthesis methods for 2D MOF film deposition, the exact growth process of conjugated MOFs remains unclear. First, almost all the synthesis methods discussed above suggest that HXTP-based MOFs cannot form in the absence of oxygen.[26, 39, 44, 56] Based on these

findings, the presence of oxygen should be involved in the reaction equation of forming $Cu_3(HHTP)_2$. Using copper acetate as a representative reactant, the corresponding reaction is shown in Equation 1. In the reaction starting with Cu^{2+} and HHTP, HHTP may undergo oxidation by O_2, or Cu^{2+} might be reduced to Cu^{+} by HHTP, then oxidized by oxygen. In the latter case, the growth process of Cu_3HHTP_2 might involves an intermediate complex state consisting of both Cu^{+} and Cu^{2+} along with HHTP, which is subsequently oxidized by O_2. However, this process occurs rapidly, making it difficult to investigate the intermediate stages. Future work focusing on slowing down the reaction process, combined with in-situ characterization techniques, could provide deeper insights.

$$3Cu(CH_3COO)_2 + 2H_6HHTP + \frac{3}{2}O_2 \rightarrow Cu_3(HHTP)_2 + 6CH_3COOH + 3H_2O \quad (1)$$

Second, single crystals of most 2D MOFs have not been obtained. The synthesis of single crystals or high-quality 2D MOF film will enable investigation of potential fundamental physical phenomenon, minimizing defects and understanding their fundamental physical properties. Third, although several oriented films have been fabricated, the underlying mechanism remain poorly understood. Additionally, a synthetic method for depositing oriented edge-on and face-on film directly on electrode with controllable thickness has yet to be reported yet. Lastly, HXTP undergoes complicated deprotonation and oxidation during coordination with metal, leading to changes in its electronic density and spin state. However, synthetic control to tune the electronic and spin properties of the MOFs through the HXTP charge state remains challenging.

2.4 Chemiresistive sensing of 2D MOFs

2.4.1 Chemiresistive sensors

Developing highly selective and sensitive chemical sensors for the detection of gases is necessary in various fields such as environmental toxic gas monitoring, agriculture, medical diagnostics, and food processing.[55, 97] Chemiresistive sensors are a type of chemical sensors that undergo electrical resistance changes upon exposure to a target chemical environment.[98] Typically, a chemiresistor consists of a chemiresistive material deposited between two electrodes.[98] Then a constant voltage is applied, and the current through the sensing material can be measured. When exposed to the analytes of interest, the sensing layer interacts with analytes, leading to the transfer of electrons or holes and thus a current change, this process is followed by a recovery time.

Several key parameters are commonly used to describe this process, including sensor response, sensitivity, response time, recovery time, and limit of detection.

The response of sensor is given by

$$Response = \frac{\Delta R}{R_0} = \frac{R_{analyte} - R_0}{R_0} \times 100\% \quad (2)$$

Where R_0 is the resistance of the device bridged with sensing materials under an applied voltage V, and $R_{analyte}$ is the resistance upon exposure to the analyte. Sensitivity (S) is defined as the slope of the resistance change of sensors versus the concentration change of the specific gas molecules. The limit of detection (LOD) is determined as the lowest amount of an analyte can be detected, which is calculated as three times the standard deviation of the base line noise level

divided by the sensitivity. Response time is the time for the sensor to reach 90% of saturation response after analyte exposure. Recovery time is the time required for the sensor to recover to 10% of its response after removing the analyte.[99] Reversibility refers to the degree to which the signal recovers to the initial state after the analyte is removed.[100]

Chemiresistive sensing systems such as conducting polymers, carbon nanomaterials, and metal organic frameworks (MOFs) are being actively investigated for their potential to operate effectively at room temperature.[103] Among these materials, the structural and chemical diversity, high surface area, and tunable pore size make MOFs a promising candidate for developing room temperature efficient chemiresistive gas sensors.[104]

2.4.2 Conductive MOFs as active material for chemiresistive sensors

Combining conductivity, well-oriented interlayer space, one dimensional porous channel, and the active binding sites, 2D MOFs exhibited high-sensitive resistance change towards gas analytes. Furthermore, their anisotropic structure allows the exploration of sensing mechanism and design strategies for 2D conductive MOFs in chemiresistors.[105] Current research on MOF-based chemiresistive sensors explored the use of pure 2D MOFs, MOF-based composites, and MOF-on-MOF architectures.[101, 106] The development of MOF-based composite enhances the performance of 2D MOFs by increasing their exposed surface area.[107] MOF-on-MOF structures demonstrated good selectivity, making them promising for advanced sensing applications.[101] This section will focus on inherently conductive 2D MOFs synthesized from redox-active planar aromatic ligands with favourable chemiresistive sensing property.

The first chemiresistive sensor based on M-HXTP was reported by Campbell et al. in 2015.[45] $Cu_3(HITP)_2$ and $Ni_3(HITP)_2$ were synthesized using solvothermal method and dispersed in acetone as MOF suspension. As shown in Figure 2.10, the suspension was then drop cast onto

IDEs (interdigitated electrodes) as a gas sensing device. The $Cu_3(HITP)_2$ sensor was then placed in a sensing chamber, with a constant potential of 100mV applied, and the current was measured, allowing the resistance to be calculated. By measuring the resistance of the sensing material before exposure (R_1) and during exposure to ammonia (R_2), it was observed that the resistance of $Cu_3(HITP)_2$ decreased upon exposure. In contrast, $Ni_3(HITP)_2$ showed no response to ammonia. Furthermore, the authors developed a sensor array of structurally related 2D MOFs including $Cu_3(HHTP)_2$, $Cu_3(HITP)_2$, and $Ni_3(HITP)_2$.[108] These fabricated sensors were exposed to five classes of volatile organic compounds (VOCs), showing reliably selectivity.

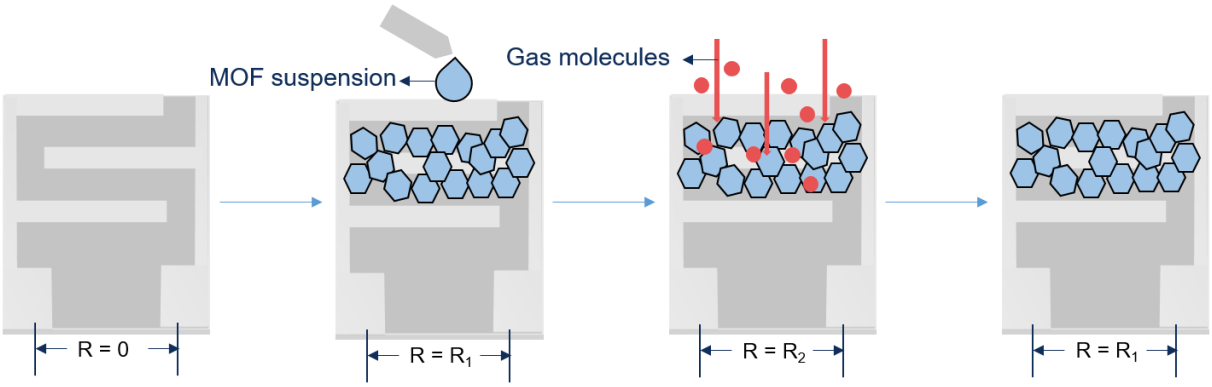

Figure 2.10. Schematic diagram showing the fabrication of a MOF-based gas sensor using drop-casting method.

The performance of MOF based chemiresistive sensor is closely related to the film morphology, thickness, grain size, and roughness.[72] The design strategy of achieve maximise sensing performance of a MOF involves high specific surface area, dense inter-particle packing, and low electrode-MOF interface resistance.[54, 64] Towards this end, various synthetic methods have been developed. Xu's group developed a spray layer-by layer method for controllable thin-film fabrication of $Cu_3(HHTP)_2$.[72] The substrates were treated with Piranha solution to obtain hydroxyl group functionalized surface firstly. Then ethanol solution of Cu acetate and HHTP ligand was sprayed on the electrode layer by layer for several cycles. The film achieved after 10 cycles synthesis exhibited a 129% response toward 100 ppm ammonia. The sensitivity and

response can be improved by increasing the exposed surface area of MOF toward analytes. For example, smaller nanoflakes of $Cu_3(HHTP)_2$ have been reported to exhibit a stronger response to ammonia compared to their larger segments.[67] Synthesizing $Cu_3(HHTP)_2$ on a TiO_2 nanowire array enhance the sensor's response due to the increased exposed area of $Cu_3(HHTP)_2$ for interaction with ammonia.[107]

Mirica's group explored the use of HXTP-based MOFs on textiles for the wearable chemireistive sensors.[71, 109] The group formed $Cu_3(HHTP)_2$ and $Ni_3(HITP)_2$ MOFs on textiles by submerging the textiles in a mixture of metal salt, ligand, and ammonia hydroxide and then heating them at 80°C. A different method was used to fabricate $Cu_3(HHTP)_2$ on textile.[89] First, the textiles were coated with copper nanoparticles, and then the copper-patterned textile was submerged in an HHTP solution in a mixture of water and ethonal. All these three MOFs grown on textiles showed conductivity change to NO and H_2S.[71, 109]

2.4.3 Sensing mechanisms

Two-dimensional electronically conductive metal-organic frameworks (2D-MOFs) have significant potential to be exploited as the active material in chemiresistive gas sensors. A crucial step to maximise the effectiveness of the device is to understand the interaction between the MOF and the analyte molecules that are being detected. However, understanding the exact mechanism of the interaction between analyte molecule and HXTP-based MOFs remains limited.

HXTP based MOFs have been reported to possess multiple possible interacting sites that can lead to conductivity change when exposed to gases.[110] In principle, charge transfer can occur between metal centres and exposed gases, even altering the oxidation state and affecting the

materials electronic properties.[108, 110] The ligand can also be engaged in electron withdrawing interactions with analyte.[111] The interlayer space, which serve as charge transport pathway, can lead to structural distortion when the gas interacts with metal ions.[112] Much effort has been made to characterize the electronic structural changes and surface chemistry shifts of 2D MOFs as chemiresistive sensors.[72, 110, 113] Several characterization methods are widely used to achieve such understanding, including in-situ diffuse-reflectance infrared Fourier transform Spectroscopy (DRIFT), Raman spectroscopy, XPS, and XRD. Both DRIFT and Raman spectroscopy provide insights into the shift of vibration modes, while XRD offer information on structural change. XPS is valuable for examining redox activity.

One strategy to study the interaction between MOF and analytes is to change the metal centre within isostructural MOFs. Campbell et al. synthesized a family of structurally analogous 2D MOFs and fabricated them as a chemiresistive sensor array. It was found that changing the metal centre from Cu to Ni lead to no response to ammonia, which probably due to the charge density difference between Cu and Ni based HXTP MOFs.[108] Combining simulation with infrared reflection absorption spectroscopy (IRRAS) and PXRD, Rubio-Giménez et al. proposed that the NH_3 interact directly with Cu^{2+}, leading to increased interlayer separation, thus distortions of the electronic structure.[112] Mirica and co-workers reported how the surface chemistry of 2D could affect the interaction between MOFs and analytes.[110] The Cu-HHTP has been found partial reversible structure change upon exposure to NH_3 due to the weak Bronsted acidity and Lewis acidity.[110, 112] The analysis of the XPS data shows that Cu^{2+} undergoes redox process in both HITP and HHTP-based MOFs. In $Cu_3(HITP)_2$, the Cu^{2+} is reduced. Conversely, in $Cu_3(HHTP)_2$, increased Cu^{2+} was observed.

Ligand centred interaction was suggested for HIB based MOFs.[69, 111] Park et al. observed that the peak of Cu-N for Cu-HIB exhibits no change when exposed to H_2O/N_2 instead of N_2. In contrast, peaks at 1510 and 1550 cm^{-1}, which were assigned to v(C=C)/ δ(N−H) vibrations, exhibited a shift toward higher frequencies. The authors therefore suggested that the interaction between H_2O and organic linkers in Cu-HIB could lead to changes in conductivity.[24] Yao et al. synthesized Cu_3(HHTP)(THQ) as a chemiresistive sensor that exhibited a LOD of 0.02 ppm on exposure to ammonia. After exposed to ammonia, IR peaks revealed the present of NH_3-Cu^+ and NH_3-Cu^{2+}. Furthermore, PXRD analysis indicated lattice expansion in the MOF.[114] Stassen et al. found that upon exposure to CO_2, imine-containing MOFs including $Cu_3(HIB)_2$, $Ni_3(HIB)_2$, and $Ni_3(HHTP)_2$ exhibited change in conductivity. However, no such change was observed for $Cu_3(HHTP)_2$. This confirms the significant role of imine group for the interaction between MOFs and CO_2.[111]

Overall, it is highly possible that there are competitive interactions responsible for the conductivity change of 2D MOFs towards gases. Both metal centre and the ligand can act as binding sites during exposure. Previous research provided valuable insights into the conductivity changes of M-HXTP when exposed to induced gases. However, explaining the underlying complexities remains challenging due to the intrinsic anisotropic conductivity, observed mixed valence of copper, the presence of defects, and the redox active ligand of these compounds. The interaction between $Cu_3(HHTP)_2$ and analytes can be influenced by several factors. First, previous studies analyse its response to ammonia without considering the anisotropic charge transport pathway and distinct surface chemistry of 2D MOFs.[95] The interaction between an analyte molecule and the crystal surface termination along the stacking direction is very different from the interaction perpendicular to the stacking direction, then the orientation of the crystals affects the sensing properties. Second, the interaction between

$Cu_3(HXTP)_2$ with ammonia involves the redox process of Cu^{2+}, the valence state of Cu appears to be an important factor in the interaction. A synthesis method for achieving high crystalline film is required to analyse the interaction reliably. Third, different responses toward the same concentration of analyte were often observed from 2D MOFs, indicating there might be structural change remaining an open question for further research. Further investigation of orientation control on the film orientation with good crystallinity and in-situ spectroscopic methods are promising to provide insight into the interactions.

2.5 EPR of MOFs

2.5.1 EPR characterization of MOFs

Apart from their rich electronic properties, conductive MOFs are promising candidates for spintronic applications due to the presence of paramagnetic spin centres and their redox activity. They have been proposed for use in devices such as spin valves, spin liquids, quantum sensing, and electronic qubits.[8] For example, in the HHTP-based MOF, the metal spins of $Cu_3(HHTP)_2$ are arranged in a Kagome lattice, which enabled its potential application in quantum spin liquid.[42] The first 2D MOF exhibiting ferromagnetic and remarkably conductivity named PTC-Fe (PTC=1,2,3,4,5,6,7,8,9,10,11,12-perthiolated coronene) was reported by Dong et al.[115] Electron paramagnetic resonance spectroscopy (EPR) has been employed to identify the spin centres, spin surrounding environment, and investigate spin relaxation of MOFs by looking into the unpaired electrons.[12] This chapter will focus on using EPR to investigate the properties of electronic spins in the π-conjugated ligand-based conductive MOFs. Specifically, continuous wave (CW) EPR measurement allows the investigation of redox state and chemical environment of MOFs, and the pulsed EPR studies the spin dynamics of the radicals in MOFs.[116]

The formation of organic radicals and their electronic state change in MOFs can be revealed by CW-EPR experiments. For example, in $Cu_3(HHTP)_2$, CW-EPR measurements show only broad Cu^{2+} signals due to the high concentration of Cu^{2+} spins and low concentration of organic radicals (Figure 2.11a).[17] $Zn_3(HHTP)_2$ was reported to be isostructural with $Cu_3(HHTP)_2$.[27, 42] Unlike Cu, which can exhibit both diamagnetic +1 valence state and paramagnetic +2 valence states, Zn is inactive and diamagnetic. This leads to the observation of HHTP-centred monoradicals in $Zn_3(HHTP)_2$, exhibiting a near-symmetric signal (Figure 2.11a).[21, 117] The peak positions in the spectra, plotted with the magnetic field on the x-axis, are related to experimental conditions. The g-factor can be calculated from the magnetic field as the fingerprint of a material to identify the spin centres (Figure 2.11b). By increasing the percentage of Zn in the bimetallic $Cu_xZn_{3-x}(HHTP)_2$ system, an increased intensity of radical peak was observed, suggesting the change in spin states in the bimetallic MOFs.[117] The HHTP-based radical is also observed in other diamagnetic metal-centred analogues, such as $Co_9(HHTP)_4$ and $Mg_9(HHTP)_4$ with intercalated layered ligand complexes.[12, 20, 40] The direct observation of radical formation using EPR enables investigation on the charge storage mechanisms, gas adsorption phenomena, and catalytic process.[21, 118-119]

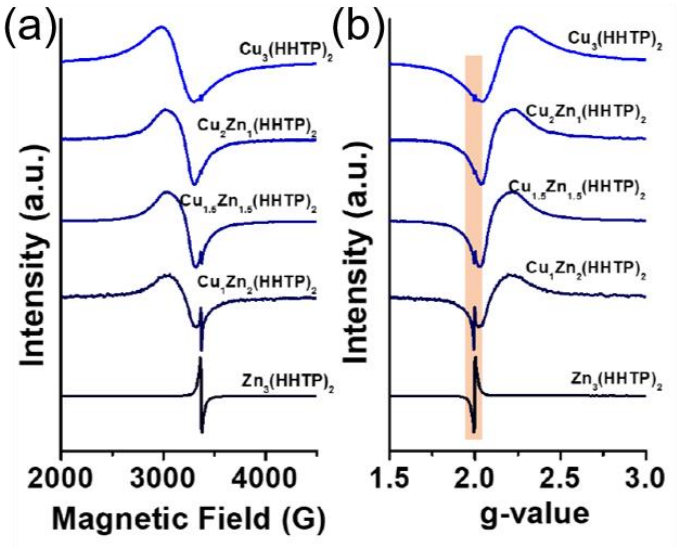

Figure 2.11: CW-EPR and pulse EPR spectra of HHTP-based MOFs demonstrating the application of EPR in MOFs (a) Room temperature EPR spectra and (b) calculated g-value spectra for $Cu_3(HHTP)_2$ (blue), $Cu_xZn_{3-x}(HHTP)_2$ and $Zn_3(HHTP)_2$ (black), with the highlighted area indicating the presence of organic radicals. Adapted from reference [117].

In pulsed EPR experiments, two key parameters describe the spin dynamics: the spin relaxation time T_1 and the phase memory time T_m.[120-121] T_m, also known as transverse relaxation time, describes the lifetime of an ensemble of spins maintain spin coherence before losing its phase relations.[121-122] T_m is measured using Hahn echo sequence ($\pi/2 - \tau - \pi - \tau$ – echo).[123] In this sequence, a $\pi/2$ pulse rotates the spins into the x-y plane, allowing precession for a time τ. A π pulse then refocuses the spins, producing an echo signal (Figure 2.12, green).[120, 124] Another important parameter is the longitudinal relaxation time T_1, which describes the relaxation of a spin population from an excited state to thermal equilibrium.[125] The inversion recovery pulse sequence (π – T – $\pi/2 - \tau - \pi - \tau$ – echo) is typically used for T_1 measurements (Figure 2.12, purple), where an initial π pulse inverts the longitudinal magnetisation.[124] Prolonging T_m and T_1 of electronic spins enable manipulation and application of molecular qubits.[126]

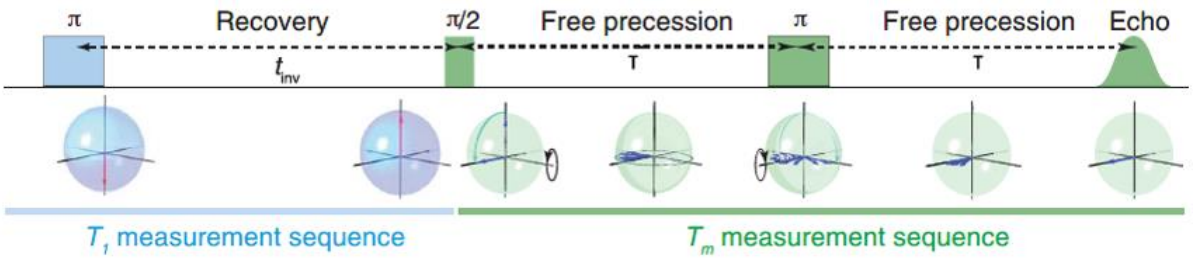

Figure 2.12: Pulse sequence of pulse EPR experiments measuring the spin relaxation times and the Bloch-sphere representation. Adapted from reference .

2.5.2 Design of MOFs towards long phase memory time

Molecular systems possessing long-lived paramagnetic spin centres have been investigated as molecular qubits, taking advantage of the electronic sub-levels under an applied magnetic field.

Chemical design allows fine-tuning of these solid-state spin qubit.[121, 127] Metal-based molecule systems have been reported showing millisecond-scale T_m at low temperature.[128] However, most of these molecules fail to maintain coherence at room temperature. The challenge with achieving long room temperature phase memory time in molecular systems lies in the random distribution of spin centres within diamagnetic matrices, making precise spatial control of qubits highly challenging.[121, 129-130] Constructing a predictable and well-defined periodic array of molecular spins is therefore a promising pathway to achieve control on molecular spin systems.[129-131] The chemical precision and periodicity of MOFs makes them promising for synthetic control of the chemical environment of the spin centre.[7, 43, 132-133]

Most reported MOF qubits are based on paramagnetic metal centres, including copper (II), VO (IV), and cobalt (II). For instance, one extensively studied molecule showing room temperature coherence is metal phthalocyanines.[134-135] To achieve spatial control of these molecular qubits, these molecules have been built into frameworks as qubit nodes.[129, 136] Zadrozny et al. reported a MOF qubit based on cobalt porphyrin units (TCPP = 5,10,15,20 tetrakis(carboxyphenyl) porphyrin), these units then were incorporated with diamagnetic Zn^{2+} porphyrin units and $[Zr_6O_4(OH)_4(H_2O)_6]^{6+}$ structural nodes.[132] In this way, the paramagnetic cobalt porphyrin units were diluted in the framework to increase the coherence time, T_m of 2μs was achieved at 15K. As shown in Figure 2.13 a, Yu et al. reported the first potential MOF qubit without spin dilution in diamagnetic frameworks, the Cu-PCN-224, a porous porphyrinic zirconium MOFs.[129] At 80K, the phase-memory time was measured as 25 ns, with ligand vibrations were reported to be the major cause to the spin-lattice relaxation. Then Yamabayashi et al. reported a porous 3D network based on vanadyl qubits, constructed by vanadyl tetra-carboxyl-phenyl-porphyrinate [VO(TCPP)] building block as spin centre and $[Zn_2(COO)_4]$ as connecting units.[133] Upon

dilution by [TiO(TCPP)], T_m of 0.15μs was achieved. However, most of these MOFs with only paramagnetic metal spin centres do not show a comparable coherence time at room temperature.

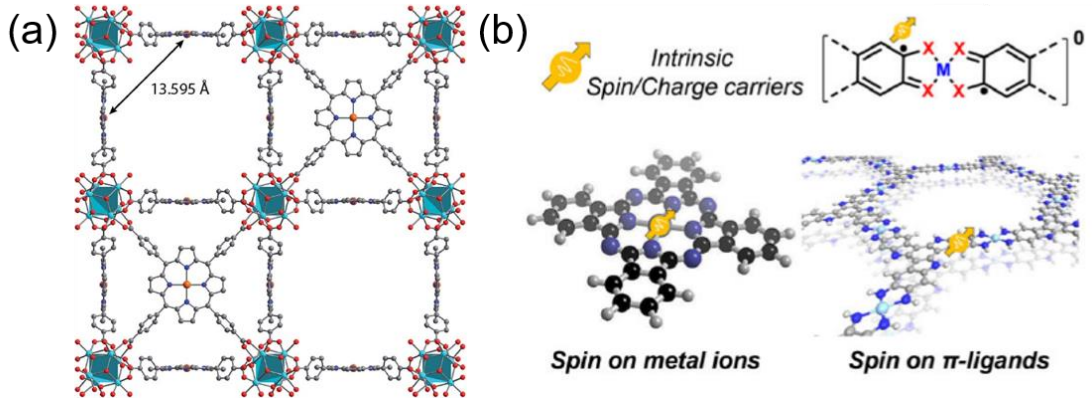

Figure 2.13: (a) Example of a MOF with spin localized on metal ions, illustrating the crystal structure of Cu-PCN-224 MOF. Cu, oxygen, nitrogen, and carbon are represented by orange, red, blue, and grey, respectively. The structure consists of a porphyrinic ligand metalated with Cu^{2+}, connected by Zr_6O_6 nodes. Reproduced from reference 129. (b) Example of an organic radical-based MOF, showing the presence of intrinsic radical in 2D MOFs. Adapted from reference 7.

Organic radicals, on the other hand, were found to maintain coherence at room temperature.[131] These ligands usually have (1) a planar structure with π conjugation, which can effectively promote long-range delocalization of the electrons. (2) multiple binding sites, generally containing nitrogen and oxygen donor group, connected with the π conjugated system and capable of forming strong π-d hybridization with transition metals.[13, 43, 137] The oxidation state of most of these organic radicals can be manipulated with minimal structural arrangement, enabling the study of changes in the electronic structure of the materials independent of morphological changes.[137] Some conjugated linker has been reported possessing radicals when forming MOFs, such as HXTP discussed above. Other ligands proposed to possess stable radicals include HXB, HXTT (2,3,7,8,12,13-hexa-substituted tetraazanaphthotetraphene), and HATI (2,3,7,8,12,13-hexaiminotriindole) (Figure 2.14a-d).[138-139] Despite the focus on planar ligands for constructing 2D MOFs, several non-planar catechol-based ligands have also been introduced, such as dibenzo[g,p]chrysene-2,3,6,7,10,11,14,15-octaol (DBC) and Contorted

hexabenzocoronene (c-HBC).[29, 140] Although stable radicals have been found existing in these ligand-based MOFs, experiments showing their qubit-like behaviour have rarely been presented.

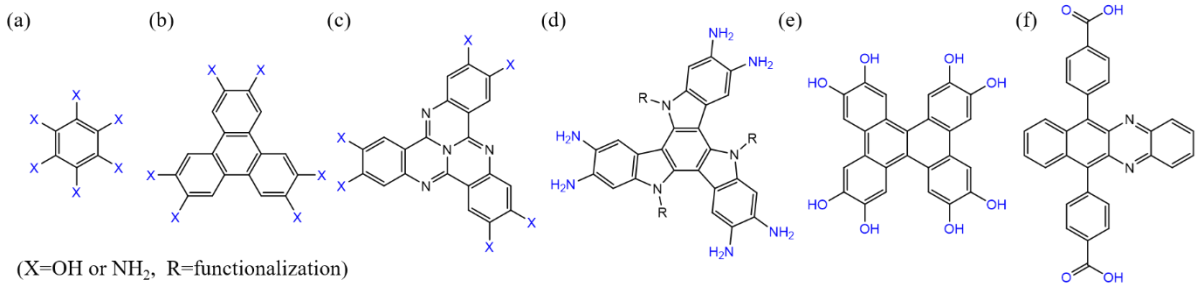

Figure 2.14. Examples of π radical containing ligands when constructed as MOFs. (a) HXB (b) HXTP (c) HXTT (d) HATI_R (e) DBC (f) DAT.

Several strategies have been reported to incorporate radicals into MOFs, including structural integration and incorporation as guest molecules in the pores.[137] Structural integration enables preservation of the porous and crystal structure of MOFs (Figure 2.13b). Very recently, a few studies have explored designing a MOF with organic radicals and diamagnetic metal centre to achieve long phase memory time at room temperature. Sun et al. synthesized Mg-HOTP with organic radicals as the only spin centre.[20] Such design enabled room temperature spin phase memory time ranging from 153 ns to 239 ns at 296 K. Lu et al. reported the synthesis and spin dynamics of $Ni_3(HATI\_R)_2$, (R=H, vPr, nPr, and iPr for hydrogen atom, allyl, n-propyl, and isopropyl groups), the R functional groups are modified to tailor the stacking distance of the 2D MOFs.[141] EPR analysis shows that the spin relaxation of $Ni_3(HATI\_R)_2$ was too rapid to be detected even at 5K. With an increased interlayer space and weakening interlayer interaction, the $Ni_3(HATI\_R)_2$ (R=vPr, nPr,and iPr) show T_m of about 100 ns at 80 K. Orihashi et al. reported a series of diazatetracene (DAT)-based MOFs by reacting DAT (Figure 2.13f) with $ZrCl_2$.[142] Room temperature T_m of 0.56μs was achieved. The resulting DAT-MOF show T_m change to chemical stimuli including hexane, toluene, and H_2O.[143]

2.5.3 Incorporation of organic radicals in MOFs

The structural incorporation of radicals into MOFs involves choosing the right metal-ligand combination, and synthetic control over the growth process of these MOFs. As discussed in chapter 2.2.3, the spin state of π-conjugated linkers is dependent on their oxidation state. The multiple redox states of the ligand allow for different binding sites and coordination geometries with metals, resulting in different morphologies and electronic properties.[57, 144-145] Therefore, synthetic control of the oxidation state may affect the in-situ redox process and preferred binding sites, ultimately affecting the electronic and spin properties of resulting MOF.[144] For example, in Mg-HHTP, the oxidation states of HHTP are assigned as -6, and -3. The $HHTP^{3-}$ possesses a mono-radical within its delocalized π-system. Notably, the presence of three semiquinone binding sites in $HHTP^{3-}$ does not result in a triradical, as any two of the three unpaired electrons can pair up.[40] Wang et al. reported the direct oxidation of HXTP by direct substitution of Fe^{3+} with Ni^{2+} in Fe_3HTTP_2 MOF, with the crystal structure unchanged.[146-147] The ligand HITT was found exhibiting different oxidation state when coordinating with different metal centres. For example, $Ni_3(HITT)_2$ possesses HITT at -3 state with the presence of radical, while $Cu_3(HITT)_2$ possesses HITT at -2 state due to the coexistence of Cu^+ and Cu^{2+}.[34] The coordination geometry change along with the spin state change was observed when coordinating HHTP with Fe (II, III), Ti (IV), and V(IV), it constructs 3D MOFs, specifically $Fe(THO).Fe(SO_4)(DMA)_3$, $Ti(THO)(DMA)_2$, $V(THO)(DMA)_2$.[41] In these 3D structures, HHTP is in the -6-oxidation state in absence of radicals, with DMA as counterions.

Similar and more detailed studies can be found in HXB (Figure 2.14). HXB possesses radicals in its -5, -3, and –1 state.[148] The HHB forms 2D frameworks with a formal charge state of -3 when coordinating with Cu and Ni (Figure 2.14e), while coordinating with Fe leads to 3D frameworks when results in mix-valence ligand state (Figure 2.14g). HAB forms square planar

structure with Cu, while tetrahedral structure with Zn (Figure 2.14f).[149] When coordinating with Fe, the initial oxidation state of HHB affects the preferred coordination and final oxidation state. By reacting Fe with HHB and its oxidized form THQ, $Fe_8(C_6O_6)_6$, and $Fe_5(C_6O_6)_3$ with various ligand charge states and different structures were obtained.[148, 150] The $Fe_5(C_6O_6)_3$ composes of 2D Fe-semiquinoid layer, these layers are bridged through Fe-O bonds, with a mixed-valence state of HHB^{5-} and HHB^{4-}. In contrast, $Fe_8(C_6O_6)_6$ features ligand in HHB^{4-} and HHB^{3-} states.

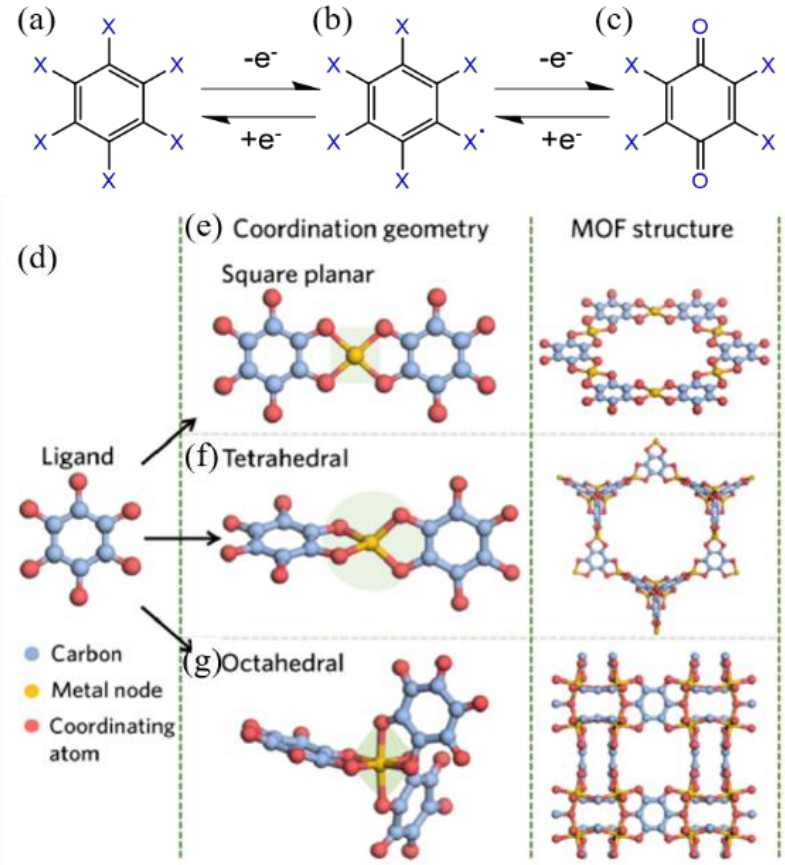

Figure 2.14: The redox process of HXB. (a) hexahydroxybenzene (HHB, where X=OH) and hexaiminobenzene (HIB, where $X=NH_2$). (b) Intermediate state. (c) tetraoxyquinone (THQ, where X=OH) and tetraamino-benzoquinone (TABQ, where $X=NH_2$). (d) Representative geometries of HXB formed when coordinating HHB with Cu and Ni (e). Coordination of HAB with Zn and Cu (f). Coordination of THQ with Fe (g). Adapted from reference 24.

When starting with ligand at the same oxidation state, adjusting the synthetic conditions also lead to change in the final oxidation states of the ligand, such as temperature control, conducting

the synthesis in ambient air or within an oxygen-free environment.[144, 151] For example, Fan et al. reported the synthesis of both 1D-CuTABQ and 2D-CuTABQ using the same ligand and metal salt but in different synthetic environments. Specifically, 2D-Cu-TABQ was synthesized in air at 120°C, while 1D-CuTABQ was synthesized in a sealed tube at room temperature, with the addition of ammonia. XPS results reveals that Cu^{2+} dominates in 1D-CuTABQ, whereas the ratio of Cu^{2+} to Cu^{+} is about 1:1 in 2D-CuTABQ. In these two structures, the 1D-CuTABQ is planar and more delocalized.[151]

Despite extensive research on the planar ligands shown in Figure 2.15, investigations into non-planar conjugated ligands remains limited. Several non-planar ligands have been developed for improved solubility and coordination geometries that differs from planar-based MOFs (Figure 2.15).[24, 28] When coordinating with Cu, these non-planar ligands forms 3D MOFs but are typically classified into 2D MOFs family due to their preserved extended conjugated structure.[28] For example, the ligand DBC, when coordinated with Cu, forms a 3D MOF with a four-fold interpenetration structure (Figure 2.15e).[152] Each Cu ion coordinates with four O atoms from two DBC ligands, forming distorted diamond networks instead of a hexagonal porous structure.[152-153] The cHBC-based MOFs includes cHBC-6O-Cu, cHBC-8O-Cu, and cHBC-12O-Cu, each forming different structures. Among these, cHBC-12O-Cu, with more metal coordination centres, exhibited higher electrical conductivity that the other two MOFs and comparable to many other conductive MOFs. The presence of organic radicals was observed in all these three cHBC MOFs (Figure 2.15d).[140] Additionally, another non-planar ligand, 4',5'-bis(3,4-dihydroxyphenyl)-[1,1':2',1"-terphenyl]-3,3",4,4"-tetraol (8OH-TPB), forms a rhombic structure in water and DMF, while a hexagonal and triangular dual-pores structure forms with the addition of ammonia (Figure 2.15f).[154]

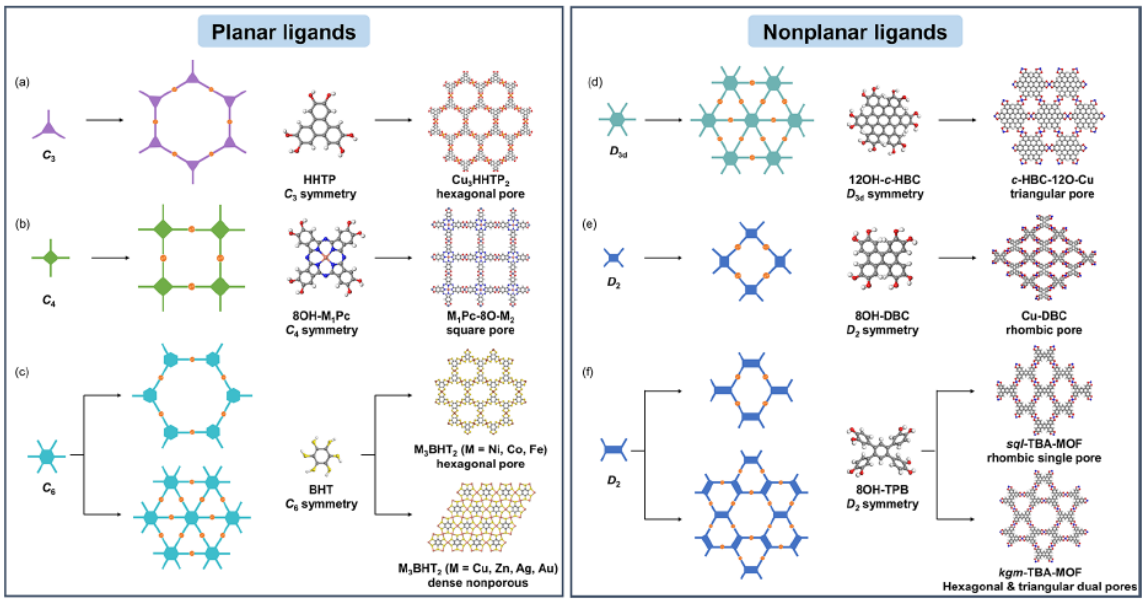

Figure 2.15: Basic topological diagrams and examples for designing conjugated MOFs. Left: Planar ligands and their corresponding MOF structures. Right: Non-planar ligands and their MOF structures (Single layer structure is shown for each case). Adapted from reference 28.

However, information on these non-planar ligands and the corresponding MOFs remains poor. Understanding on their redox active properties, synthesis method, and potential applications remains largely unexplored. Investigation into these frameworks is promising to offer design flexibility that is not accessible in planar ligand-based MOFs. Synthetic control such as electronic and spin property tuning which have not been achieved in planar ligand-based MOFs, might be achieved in these non-planar ligand-based MOFs.[154-156] For example, unlike HXTP-based MOFs, the Cu^+ is more likely to exist in 3D structures without leading to distortion of the square plane.[36, 157-158] The non-planar structure of these ligands and its distorted diamond network binding may minimize structural distortion of the framework during Cu reduction and ligand oxidation.[36] Future research on the non-planar ligand based conjugated MOF will provide deeper insight into their potential applications.

2.6 Summary

In summary, this chapter has reviewed the electronic, spin, and structural properties of 2D MOFs, emphasizing the structure-property relationship in these MOFs, which possess intrinsic anisotropic characteristics. The discussion focuses on various synthesis methods used to control film orientation, crystal size, morphology, and crystallinity in 2D MOFs, enabling investigation of their intrinsic electrical properties that are not accessible in bulk materials and achieving optimized performance for their application in electronic devices. Furthermore, the chapter explores the application of 2D MOFs as chemiresistive sensors and discusses the sensing mechanism. In addition to their conductive properties, the presence of metal paramagnetic spin centres and unpaired electrons on the organic ligands in these MOFs is described. Achieving precise control through synthesis methods and the selection of appropriate metal-ligand combinations are crucial for tailoring the electronic and spin properties of the resulting MOFs and understanding their structure-property relationships.

Despite this progress, key challenges remain in the synthesis and processing of two-dimensional conductive MOFs, particularly in achieving precise control over their morphology, orientation, and processability. While several methods have enabled the preparation of insulating MOFs in solution-processable form, equivalent strategies for conductive systems are still limited. This hinders the fabrication of uniform films through scalable deposition techniques. Furthermore, although different synthetic approaches have been employed to control film orientation, the growth of edge-on films with tunable thickness has not been fully realised, restricting the study of orientation-dependent charge transport and device performance. In addition, although many conductive MOFs contain spin-active centres and show theoretical promise for quantum and spintronic applications, their spin-related properties remain largely unexplored. These challenges define the motivation for this thesis, which develops electrochemical and solution-based synthesis strategies to control film morphology and orientation, investigates how

structural directionality influences sensing behaviour, and explores the redox and spin states of conductive MOFs to advance understanding of their charge and spin transport properties.

Chapter 3

Methodology

This chapter presents an overview of the general characterization methods used in this thesis, focusing on their fundamental working principles and their relevance to the studies discussed in experimental chapters 4-7. This chapter begins with a brief introduction to the materials and substrates used throughout the thesis. Next, the synthesis methods are introduced. Finally, the characterization techniques are discussed. Specific experimental procedures will be described in each of the experimental chapters.

3.1 Materials

The ligand 2,3,6,7,10,11-Hexahydroxytriphenylene (HHTP) was purchased from Fluorochem. The dibenzo-[g,p]chrysene-2,3,6,7,10,11,14,15-octaol (DBC) was purchased from BLD Pharm. Tributylmethylammonium methyl sulfate (TBMAMS) was purchased from Santa Cruz Biotechnology. The other chemicals were purchased from Sigma-Aldrich. All gases were purchased from BOC Gases UK.

Thin film platinum interdigitated electrodes (IDEs) with a width and gap of 5 μm on glass were purchased from MicruX Technologies. The dimensions of IDEs are 10 mm×6 mm ×0.75 mm, and the Pt thickness is 150 nm. Before use, the IDEs were rinsed with water and ethanol (without sonication to prevent damage to the electrodes). After use, the IDEs were recycled using piranha solution. Indium Doped Tin Oxide (ITO) coated glass slides with a surface

resistivity of 70 -100 Ω/sq were purchased from Sigma Aldrich. The dimensions of the ITO glasses are 75 mm×25 mm ×1.1 mm. The ITO glasses were sonicated with DI water, acetone, and ethanol for 10 min each. 3M copper tape (1181 series) was purchased from RS Components with acrylic adhesive. The counter electrode Platinum (Pt) coil was purchased from BASi, USA, the reference electrode Ag/AgCl electrode was purchased from CH Instruments, USA.

3.2 Synthesis and deposition methods for conductive MOFs

3.2.1 Solvothermal synthesis of conductive MOFs

Several solvothermal synthesis methods were explored in this thesis to produce conductive MOFs, followed by device integration through drop-casting. Traditional solvothermal synthesis for 2D MOFs involves reacting metal salts with organic ligands in suitable solvents, heating the mixture at 85 ℃ for 3 days under ambient conditions. These parameters were either maintained or slightly modified depending on the specific metal-ligand combination and preferred structural properties. Furthermore, an optimized solvothermal synthesis method was developed to obtain solution-processable MOF nanocrystals, with size control over their growth process. This approach involved the use of additives to regulate the MOF crystal growth process.

After synthesis, the resulting MOF powders were dispersed in solvents such as ethanol and then drop cast onto the electrode surface. A thin film formed after the solvent evaporation. The thickness of this film could be controlled by adjusting the concentration of the solution and the number of drop-casting repetitions.

3.2.2 Electrochemical synthesis of conductive MOFs

For the electrochemical experiments, a PGSTAT204 Autolab electrochemical workstation (Eco Chemie, Netherlands) was used, controlled via a PC using NOVA 2.1 software. A standard 3-electrode set-up was employed, consisting of a Pt coil as the counter electrode and an Ag/AgCl electrode as the reference electrode (Figure 3.1).

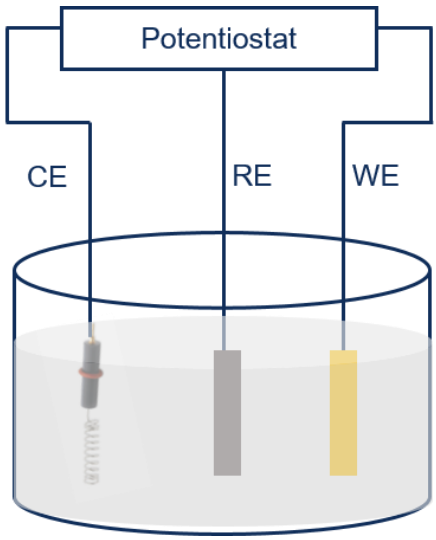

Figure 3.1: Schematic diagram of the three-electrode electrochemical setup used for MOF film deposition and cyclic voltammetry (CV) measurements. A platinum coil serves as the counter electrode (CE), and an Ag/AgCl electrode is used as the reference electrode (RE). The working electrode (WE) varies depending on the experiment and includes Cu tape, ITO glass, Cu tape adhered to the opposite side of ITO glass, or Cu tape attached to the opposite side of an interdigitated electrode (IDE).

Cyclic voltammetry (CV) is a widely used electrochemical method for investigating the redox behaviour of compounds. In a CV experiment, a voltage is applied to the working electrode, and the applied voltage is swept forward and then reversed back to the initial voltage. During this process, the compound at the electrode surface may undergo oxidation or reduction, depending on the applied voltage potential and the compound's electrochemical properties. The current generated at the working electrode is measured as a function of the applied voltage, creating a plot of current versus applied potential. This graph provides information such as the redox potential, electron transfer kinetics, and whether the redox process is reversible or irreversible in each system.[159]

In this work, CV measurements were carried out on an ITO glass electrode to investigate the redox behaviours of the ligand, metal, and the synthesized MOF. The oxidation potential of Cu and the ligand was determined form the CV results. This information is crucial for optimizing the conditions for further electrochemical synthesis of MOFs, as it helps identify the appropriate potential for the formation and control of the MOF structure.

Chronoamperometry is an electrochemical technique used to study the current response of an electrochemical system when a constant voltage is applied to the working electrode, producing a current versus time diagram. The applied potential for a CA experiment is determined based on information from CV, particularly the desired oxidation state of the reactant. Additionally, CA analysis provides information about quantitative analysis of the reaction on the electrode surface. By integrating the current over time trace, the total consumed charge (Q) during reaction can be calculated.[159-160]

In this work, Chronoamperometry was used to directly deposit MOF film on working electrode by applying a constant voltage. Several kinds of electrodes were used, including Cu tape, a combination of Cu tape and IDE, and Cu tape with ITO glass. These electrodes were submerged in a solution containing the ligand and electrolyte. Upon applying a voltage determined from the CV measurements, MOF films were successfully fabricated over various time periods.

3.3 Sensing chamber setup

Sensing experiments were performed in a stainless-steel gas-sensing chamber (Figure 3.2).[161] The carrier gas and analyte gases are mixed at a T-joint to ensure thorough gas mixing before entering the gas chamber. The flow rate of each gas was controlled by an Alicat mass flow

controller. By tuning the flow rate of each gas, the analyte concentration can be controlled. Throughout all sensing experiments, a total flow rate of 500 standard cubic centimetres per minute (sccm) was maintained.

The sensor was connected to a Keysight U8001A single output DC power supply. During the measurement, a constant voltage is applied to the MOF-coated interdigitated electrode, and the resulting current is measured using a Keysight B2900A source meter. For all sensor measurements conducted in this thesis, a voltage of 1.0 V was applied. To balance performance and measurement reliability, the applied voltage was selected to be low enough to prevent self-heating effects, yet sufficiently high to ensure an acceptable signal-to-noise ratio. Nitrogen was used as the carrier gas throughout the experiment. The analyte gas was 10 ppm ammonia diluted in dry nitrogen. Prior to each measurement, the device is exposed to nitrogen flow for 1-2 hours until the baseline is stabilized. Once stabilization was achieved, the sensor was exposed to various concentration of ammonia for the subsequent response measurements.

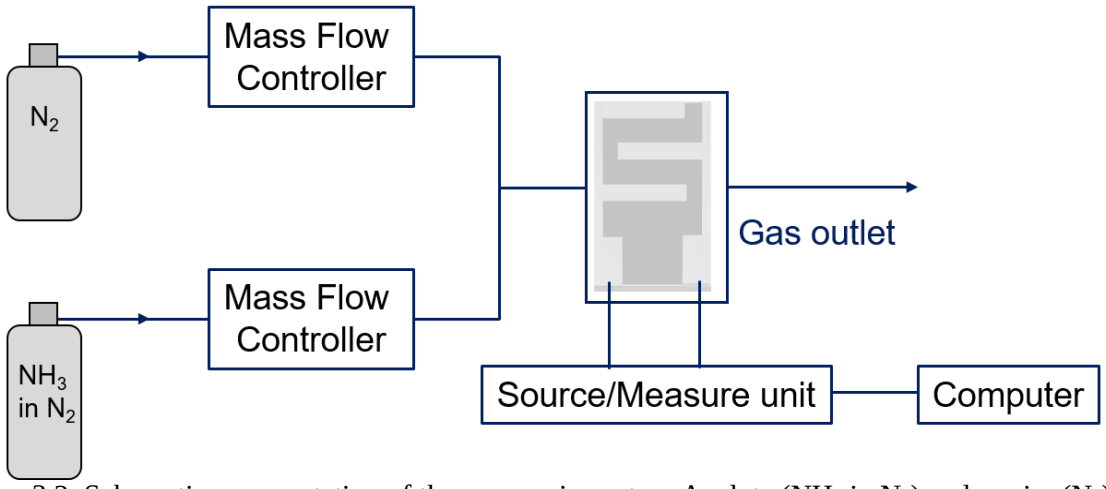

Figure 3.2: Schematic representation of the gas sensing setup. Analyte (NH_3 in N_2) and carrier (N_2) gas cylinders are connected to mass flow controllers (MFCs) for regulating gas flow rates, with a T-junction for mixing the gases before they enter the sensing chamber. The chamber houses the sensor, which consists of a MOF film deposited on an interdigitated electrode (IDE) substrate. Electrical connections from the sensor to a source/measure unit enable real-time resistance or current measurements. Data is recorded by a computer.

3.4 Characterisation techniques

3.4.1 Electron microscopy

Scanning electron microscopy, SEM, was used to determine the morphology of the synthesized MOF materials in this thesis. This technique involves an electron gun emitting a beam of electrons, which is accelerated and focused through lenses to a small spot size on the sample surface. As this focused beam scans across the sample surface, it ejects secondary electrons, which are detected to produce high-resolution images of the surface's microstructure.[162]

A Zeiss Merlin – Analytical SEM was used in this work. Samples were stuck on 9-pin stubs using carbon sticky pads and partially covered using conductive copper tape. Most images were obtained at an accelerating voltage between 10kV-15kV with probe current of 100 pA. The SEM analysis provided information about the morphology of MOF bulk powder, orientation of the MOF film, and MOF nanocrystals. Additionally, the SEM images revealed the particle size distributions of nanocrystals.

In contrast, transmission electron microscopy (TEM) uses the transmitted electrons, the electrons pass through the sample to be collected. Therefore, TEM provides information on intrinsic structures such as crystal lattice. All TEM images in this thesis were taken from a JEOL TEM-2100. For TEM analysis, MOF samples were dispersed in ethanol and drop-cast onto copper grids with holey carbon films. For some conductive MOFs, it is still challenging to grow single crystals, therefore, TEM provides additional information into their 2D layer structures and stacking modes.[16]

3.4.2 Atomic force microscopy

Atomic Force Microscopy (AFM) is a type of scanning probe microscopy. It uses a sharp tip attached to a flexible cantilever that bends when interacting with a surface. As the tip contacts the surface, the bending is detected by a laser and photodector to determine the force between the tip and the surface. By recording the vertical movements required to maintain this constant force, the AFM determines the height difference between the substrate and the top of the layer, thereby measuring the thickness of the film.

Conductive AFM (cAFM) is used to measure the electrical properties of a surface. In cAFM, the tip is coated with a conductive material, allowing it to pass electrical current between the tip and the sample. As the AFM scans the surface, it not only maps the topography but also measures the current flowing through the surface at each point. This technique provides information on the sample's local conductivity.[95, 163]

In this thesis, AFM is used to measure the thickness of the oriented films at various deposition times. The cAFM is employed to measure the local conductivity of the oriented film. AFM experiments were performed by Shengming Zhang from Bruce's group using a Bruker Dimension Icon AFM, with all samples in a glovebox filled with argon (< 0.1 ppm H_2O, < 0.1 ppm O_2) at room temperature. All samples were grounded by conductive silver paste. AFM probes (SCM-PIT-V2) were calibrated according to standard samples (Samphire and Ti roughness sample) interpolating the actual spring constant and tip radius (~5 nm). The PeakForce Tunneling AFM (TUNA) method was conducted to capture both topography of samples and corresponding TUNA current data (average current during a full tapping cycle). The 3D topography images were reconstructed by NanoScope Analysis 2.0 software.

3.4.3 X-ray diffraction

X-ray diffraction (XRD) is a technique used to determine the lattice parameters and structural ordering of crystalline materials.[164] When X-rays interact with a crystal, they are scattered by the periodic arrangement of atoms. The interference occurs at specific angles is determined by Bragg's law:

$$n\lambda = 2d\sin\theta \quad (1)$$

where λ is the wavelength, d is the inter-layer spacing, θ is the angle of incidence, and n is an integer.

In layered materials, the orientation of a film relative to the substrate can be determined from its X-ray diffraction pattern (Figure 3.3). When the layers lie parallel to the substrate, forming a face-on orientation, the incident X-ray beam primarily probes the interlayer spacing along the stacking direction, resulting in distinct out-of-plane diffraction peaks. If the layers are aligned perpendicular to the substrate in an edge-on arrangement, the pattern is dominated by in-plane reflections. By analyzing the positions and intensities of these peaks, the orientation of the film can be identified.

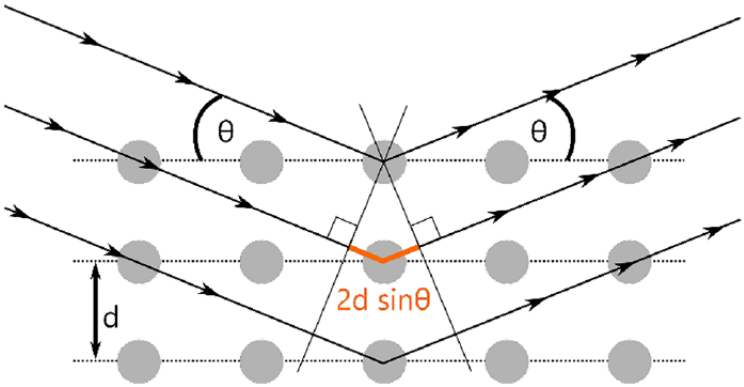

Figure 3.3: Schematic representation of Bragg's law, illustrating the principle of X-ray diffraction. An incident X-ray beam interacts with parallel atomic planes at an angle θ, resulting in reflected beams. Constructive interference occurs when the path length difference between these reflected beams equals an integer multiple (n) of the X-ray wavelength (λ), leading to a diffraction peak at angle 2θ. By analyzing the positions of these peaks, the d-spacing and crystallographic structure of the material can be determined.

In this thesis, a Mini-flex XRD was used for powder analysis, while an Empyrean XRD was used for thin film analysis and situations when the sample quantity was limited. XRD was used to confirm the successful synthesis of the MOFs and to detect changes in crystal structure due to various synthesis methods by analyzing the peak positions and the shifts, such as stacking distance variations. Furthermore, by comparing the intensity of each peak, the preferred orientation of the synthesized MOF films was identified.

3.4.4 UV-Vis-NIR spectroscopy

Ultraviolet-visible (UV-vis) spectroscopy is used to obtain the absorption spectra of a compound. The underlying principle of UV-vis spectroscopy involves the excitation of electrons from ground state to excited state when a compound absorbs radiation. Molecules absorb light at specific wavelengths based on their electronic structure. When the energy of the incident light matches the energy required for an electronic transition within the molecule, the molecule absorbs the light and the electron is promoted to a higher energy orbital, resulting in a spectrum of absorbance (A) versus wavelength.

UV-vis spectroscopy enables understanding of the electronic properties of MOFs and molecular complexes at low cost.[31, 144, 165] In this thesis, the UV-Vis measurements were conducted on a Varian Cary 5000 UV-Vis-NIR spectrometer. The UV-Vis absorption spectrum of solid-state 2D MOFs usually show a peak around 360 nm, corresponding to the π-π* transition, and a broad peak at about 650 nm, attributed to ligand-to-metal charge transfer (LMCT). In Cu-centred

mixed-valence MOFs, a broad peak at around 730 nm can be observed due to the intervalence charge transfer (IVCT).[34] The electronic feature of MOFs usually extends into the near-infrared range, which are observed in highly conjugated organics and conducting polymers.[11] This helps distinguish crystalline MOFs from molecular complexes.[166] Variations in electronic transitions among different compounds lead to distinct spectral properties.

3.4.5 X-ray photoelectron spectroscopy

X-ray photoelectron spectroscopy (XPS) was employed to measure the oxidation state of metals in MOFs. In an XPS experiment, X-rays are directed onto a sample, leading to the emission of photoelectrons with a specific kinetic energy. The different kinetic energies are related to the binding energy of the electrons, which reflects the energy of an electron attracted to a nucleus. The binding energy is related to their atomic number and the chemical environment of the atoms. Thus, XPS enables the identification of materials composition and the oxidation states of its elements.[167] For MOFs, XPS can identify the valence state of metal centres. In this thesis, XPS experiments were performed by Axel Forssberg on a PHI VersaProbe II X-ray Photoelectron Spectrometer. XPS analysis was carried out using CASAXPS software, and characteristic binding energies can be referenced to the Thermo Fisher Scientific XPS database.

3.4.6 Fourier-transform infrared spectroscopy

Fourier transform infrared spectroscopy (FT-IR) is a technique used to identify chemical bonds by measuring the absorption of infrared light across a range of wavelengths. When infrared light interacts with a sample, specific molecular vibrations absorb characteristic wavelengths, generating an absorption spectrum that reveals the chemical structure and composition of the

sample.[110, 168] ATR-FTIR measurements were conducted using a Nicolet iS10 spectrometer to analyse the chemical structure of oriented Cu_3HHTP_2 films and assess structural differences. In the solution-processable MOF nanomaterials project, the technique was also employed to evaluate whether the use of modulators and surfactants during nanocrystal synthesis induced changes in molecular bonding or left residual molecules.

3.4.7 Electron paramagnetic resonance spectroscopy

EPR spectroscopy enables investigation of electronic properties, interactions and coherence characteristics.[169] The fundamental principle in EPR is Zeeman splitting, in which an external magnetic field results in a splitting of the two energy levels due to the quantum mechanical nature of the electron spin. Continuous wave (CW)-EPR allows the investigation of spin states and their chemical environment. In a CW-EPR experiment, the sample is placed in a microwave radiation field with constant frequency while varying the magnetic field to achieve spin resonance.[170] This thesis focuses on Cu-catechol based MOFs, where CW-EPR provides valuable information on both components. For Cu, Cu^{2+} ions exhibit a broad EPR signal, while Cu^{+} is EPR-silent because its d-electrons are fully paired. For the ligand, it possesses semi-quinone radicals, the change can be detected by CW-EPR. By analysing the EPR spectra, the electronic structure change of metal centres and ligands due to external stimuli or conditions can be revealed.

In this thesis, EPR experiments were performed on Bruker ELEXSY-E580 and E680 EPR spectrometers, operating at X-band (~9.7 GHz). CW-EPR was first used to study the interaction between Cu_3HHTP_2 and ammonia. It provides information on changes in the Cu^{2+}/Cu^{+} concentration and the oxidation state of ligand after exposure to ammonia, thereby revealing

how ammonia interacts with the binding sites. Then the presence of organic radicals in DBC were characterized.

While for pulse EPR experiment, the magnetic field B0 is kept constant, and the sample is given a high-power microwave pulse of given frequency v.[122] The spin relaxation times and control of the super position state are assessed by pulsed EPR. Pulsed EPR is used to study the spin dynamics of the MOFs. Various spin pulse sequences can provide different information. The Hahn-echo is a pulse sequence used to measure spin coherence. It begins with a π/2 pulse applied at time t=0, which rotates the spin packet into the transverse plane, and the spins begin to dephase. After a delay time t= τ, a π pulse is applied to reverse the dephasing, and the spin packet refocuses, producing an echo at time 2τ (Figure 3.4a). As τ increases, the echo signal weakens, reflecting the decay of spin coherence.[20, 116]

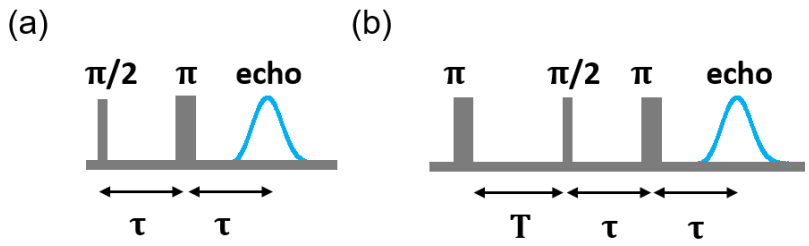

Figure 3.4: Pulse sequences used in electron paramagnetic resonance (EPR) measurements. (a) The Hahn echo experiment, which is used to measure spin-spin relaxation times (T_2). (b) The inversion recovery experiment, commonly employed to determine spin-lattice relaxation times (T_1).

Inversion recovery is used to measure the longitudinal relaxation time (T_1) of the electron spins. The sequence starts with a π pulse, which inverts the spin magnetization from its equilibrium state along the z-axis to the opposite direction. After a variable delay time T, a π/2-τ-π-τ-echo sequence is applied to measure the net magnetization along the z-axis (Figure 3.4b). The echo amplitude recovers toward its thermal equilibrium value as a function of the time decay T.[20, 116] All data analysis was conducted using the Xepr software and the Easyspin toolbox.

3.5 Summary

This chapter has introduces the materials used in this work and the experimental methods used for MOF synthesis, as well as the gas sensing setup. It then described the characterization techniques employed, including SEM, TEM, and AFM for morphology analysis, XRD for determining crystal structure and film orientation, UV-vis spectroscopy, FT-IR spectroscopy, XPS for analysing electronic and structural properties, and EPR spectroscopy for studying spin dynamics.

Chapter 4

Orientation control of 2D MOFs

Two dimensional electronically conductive metal-organic frameworks (2D MOFs) have great potential as the active material in electronic devices such as chemiresistive sensors, wearable devices, and field-effect transistors (FET).[4, 14] However, investigations into the anisotropic properties of 2D MOFs have remained limited, primarily due to synthetic challenges in achieving precise control over their layered stacking orientation. The synthesis of oriented 2D MOF films and an understanding of their growth mechanisms will provide possibilities to fabricate electronic devices with vertical and lateral orientations, therefore achieving directional anisotropic properties.

In this chapter, an electrochemical synthesis method to deposit $Cu_3(HHTP)_2$ film is reported in-situ on ITO glass with controllable film orientation and thickness. The method utilizes a dual-working-electrode setup to direct MOF formation. By adjusting the ligand concentration in the electrolyte, distinct complex structures form, which interact differently with the electrode, leading to the formation of edge-on and face-on film orientations. The highly oriented Cu_3HHTP_2 films demonstrate the contributions of conjugated planes and π-π interlayer interactions to its anisotropic conductivity.

4.1. Introduction

When two-dimensional electronically conductive metal-organic frameworks (2D MOFs) are used as the active material in electronic devices, precise control over the 2D MOF film, including factors such as morphology, contact resistance, thickness, and orientation, is crucial for maximizing the effectiveness of these devices.[5, 14, 171] Orientation control is especially relevant for stacked crystalline 2D MOF materials, where the structure and electrical conductivity are highly anisotropic. Thus, it is important to be able to control this orientation during materials integration into the device.[84, 89]

Various synthesis methods including layer-by-layer synthesis, electrochemical synthesis, and solid-interface methods have been developed to achieve control over the preferred bulk structure of 2D MOFs.[72, 76, 92, 96, 172] Among these methods, electrochemical synthesis methods for fabricating $Cu_3(HHTP)_2$ films shows potential for tuning film morphology and thickness by adjusting parameters such as applied voltage.[46, 76-77] However, cathodic synthesis requires a complex chemical environment and tends to produce randomly oriented particles.[173] Anodic deposition offers improved control for the direct deposition of oriented MOF films. In the conventional anodic synthesis method, a potential is applied either to a metal source or a substrate coated with a metal source, where both the release of metal ions and MOF formation occur at the same interface.[77] This method faces several challenges, including limited substrates options, film thickness limitations due to crystal detachment, the risk of introducing metal oxides, and the need for a complicated transfer process.[76-77, 174] Furthermore, achieving edge-on oriented 2D MOF films remains a challenge. Gaining a deeper understanding of the growth mechanism of electrochemically deposited thin films is crucial for achieving such control and enabling further optimization of the synthesis process.[81, 95, 175]

In this chapter, $Cu_3(HHTP)_2$ films were directly deposited on Indium Tin Oxide (ITO) glass with controllable lateral and vertical orientation using electrochemical synthesis. We employed a dual-working-electrode system that enables the anodic oxidation of Cu and ligand. This setup enables control over the orientation of $Cu_3(HHTP)_2$ thin films by tuning the concentration of ligand. Furthermore, I elucidate the growth mechanism responsible for the formation of both face-on and edge-on $Cu_3(HHTP)_2$ films on ITO. The synthesis of oriented 2D MOF films and an understanding of their growth mechanisms will provide possibilities to fabricate electronic devices with vertical and lateral orientations, therefore achieving preferred properties.

4.2. Experimental section

4.2.1. Solvothermal synthesis of $Cu_3(HHTP)_2$ powder

A solid mixture of HHTP (7.5 mg) and copper (II) acetate (10.5 mg) was dissolved in 2 mL of deionized water in a glass vial. The vial was then sonicated for 10 min. The mixture was heated at 85 °C for 72 h resulting in dark blue crystals. The resulting powder was washed with deionized water, ethanol, and acetone for three times and dried in air overnight.

4.2.2. Electrochemical synthesis of $Cu_3(HHTP)_2$ film

The oriented film was grown on ITO via electrochemical deposition using the same set-up. A conventional 3-electrode set-up was utilized, with a platinum counter electrode and an Ag/AgCl reference electrode, and the electrolytic cell itself was a beaker with a 10 cm diameter. Cu tape was adhered on the opposite side of ITO glass, maintaining the same size as the substrate. Different concentrations of ligand were employed in the synthesis of oriented films. For the edge-on film, 2.6 mM HHTP powder and 0.02 M Tributylmethylammonium methyl sulfate (TBMAMS) were dispersed in mixed solution of 4v:1v water and ethanol. For the face-on film,

1.3 mM HHTP powder and 0.02 M TBMAMS were dispersed in mixed solution of 4v:1v water and ethanol. The solution was then sonicated for 5 min before synthesis. The deposition takes 2 h to 12 h. The final film on ITO glasses was washed using acetone.

4.2.3. Cyclic voltammetry measurements

Cyclic voltammetry (CV) measurements were performed using the same three-electrode set-up, with a Pt counter electrode and an Ag/AgCl reference electrode. For the HHTP CV measurement, the electrolyte solution contained 2.6 mM HHTP and 0.02 M TBMAMS in a 4v:1v water and ethanol mixture, with ITO glass serving as the working electrode. In the case of the Cu tape measurement, the electrolyte solution contained 0.02 M TBMAMS in the same 4v:1v water and ethanol mixture, with Cu tape used as the working electrode.

4.3. Results and discussion

4.3.1 Electrochemical synthesis using a dual-working-electrode setup

As illustrated in Figure 4.1, I used a dual-working-electrode synthesis method, with a piece of copper tape adhered to the side opposite the ITO, where both sides serve as working electrodes. This setup allows direct deposition of the MOF film onto the electrode. The electrolyte solution contains HHTP and TBMAMS in a mixed solvent of water/ethanol (v/v, 4:1). The MOF formation on the ITO requires an appropriate voltage to ionize Cu and oxidize ligand on the electrode surface, enabling reactions on both sides.

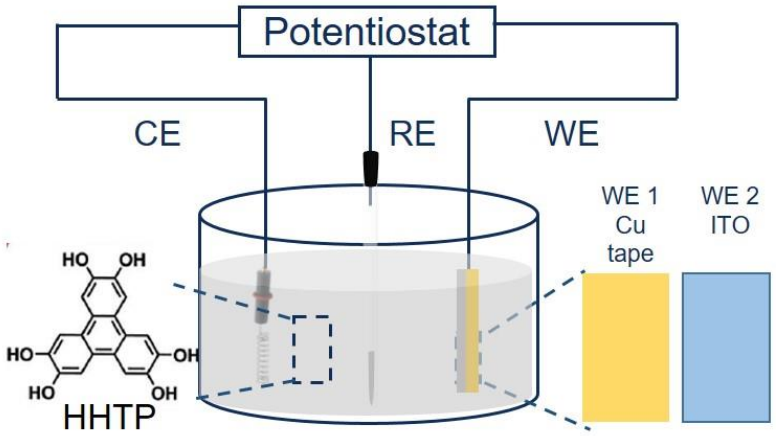

Figure 4. 1: Schematic illustration of the electrochemical synthesis setup for $Cu_3(HHTP)_2$ film deposition. The Cu tape serves as working electrode 1 (WE 1) and is adhered to the opposite side of the ITO, which acts as working electrode two (WE 2). A Pt electrode is used as counter electrode (CE), and Ag/AgCl as the reference electrode (RE). The ligand HHTP and electrolyte TBMAMS are dissolved in a water-ethanol mixture, which serves as the supporting electrolyte solution.

The electrochemical behaviour of Cu and HHTP was investigated using cyclic voltammetry (CV) to determine the potential for the electrochemical deposition. Initially, we examined the ITO as working electrode in an electrolyte solution without HHTP, which showed no peaks, indicating its suitability for studying the electrochemical behaviour of HHTP (Figure 4.2a, green). When the CV measurement of ITO was conducted in a solution containing both HHTP and the electrolyte, three anodic peaks were observed at 0.43 V, 0.65 V, and 0.9 V. Previous studies have reported six one-electron-oxidation processes for HHTP, from fully reduced $HHTP^{6-}$ to a fully oxidized $HHTP^{0}$ after deprotonation.[40, 48] The three peaks observed in our experiment likely correspond to three one-electron-oxidation processes of HHTP from CatCatCat sequentially to CatCatSq, CatSqSq, and SqSqSq (Figure 4.2b).[39, 46, 94] The ionization of Cu tape, used as working electrode in an electrolyte solution without HHTP, starts at about 0.2V and shows a peak at about 0.43V. Therefore, a potential of 0.43V was chosen to enable the oxidation of both Cu and the HHTP. After 30 min deposition, a dark film was observed on both the Cu side and ITO sides. Notably, 10 CV cycles were performed for HHTP, with only the first cycle shown, as it exhibited the most intense oxidation peaks. In the case of Cu, when

the potential was swept back, an increase in current was observed, suggesting incomplete consumption of the Cu electrode. Therefore, only the forward sweep for Cu is presented.

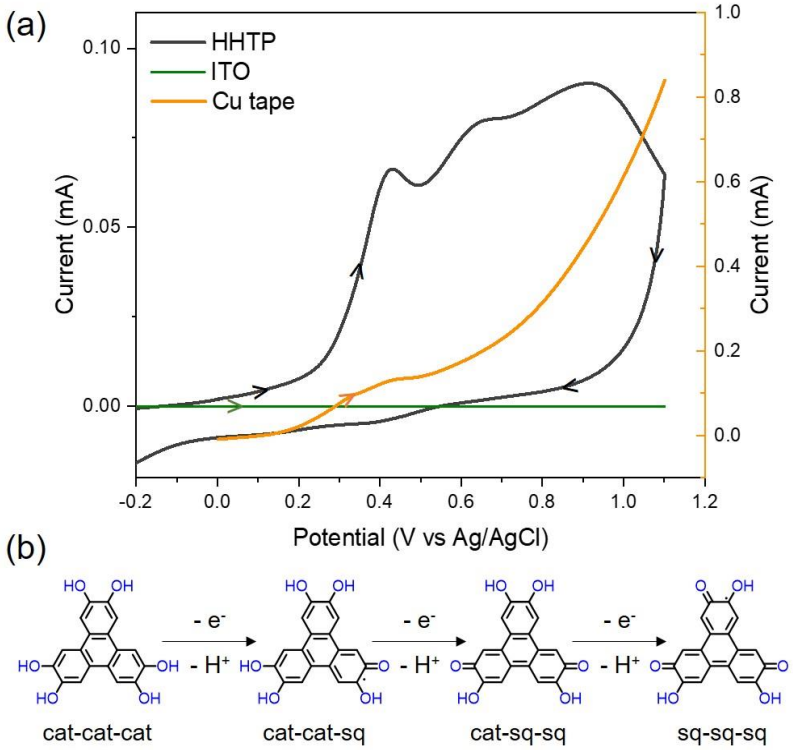

Figure 4. 2: (a) CV curves of ITO glass in solution containing electrolyte only (green), Cu tape in solution containing electrolyte only (orange), and ITO glass in solution containing HHTP and electrolyte (grey) at scan rates of 100 mV/s, with the scan initiated at 0V in the positive direction. (b) Schematic illustration of the redox sequence of HHTP in the absence of metal ions and base, showing the oxidation from H_6-HHTP (cat-cat-cat) to H_3-HHTP$^{\cdot}$ (sq-sq-sq) state.

Then we aim to confirm the successful deposition of $Cu_3(HHTP)_2$ on the ITO side. The powder was scraped off from ITO glass for PXRD characterization. As shown in Figure 4.3a, peaks at 4.9°, 9.6°, 12.6°, 16.6° and 28° for 2θ correspond to the (100), (200), (210), (220) and (001) planes of $Cu_3(HHTP)_2$, respectively.[72] XRD pattern of the scraped $Cu_3(HHTP)_2$ powder (blue) is consistent with both the solvent synthesized $Cu_3(HHTP)_2$ powder (grey) and the XRD pattern reported in literature.[72, 76] Detailed insight into the electrochemically synthesized $Cu_3(HHTP)_2$ with 2 distinct structures was obtained using high resolution TEM measurements. The TEM

images and corresponding FFTs shows a highly ordered linear arrangement with a lattice periodicity of 1.8 nm (Figure 4.3b) and a hexagonal crystalline structure (Figure 4.3c), showing the lattice structure of $Cu_3(HHTP)_2$.[16] These results confirm the successful synthesis of $Cu_3(HHTP)_2$ using the dual-working-electrode strategy.

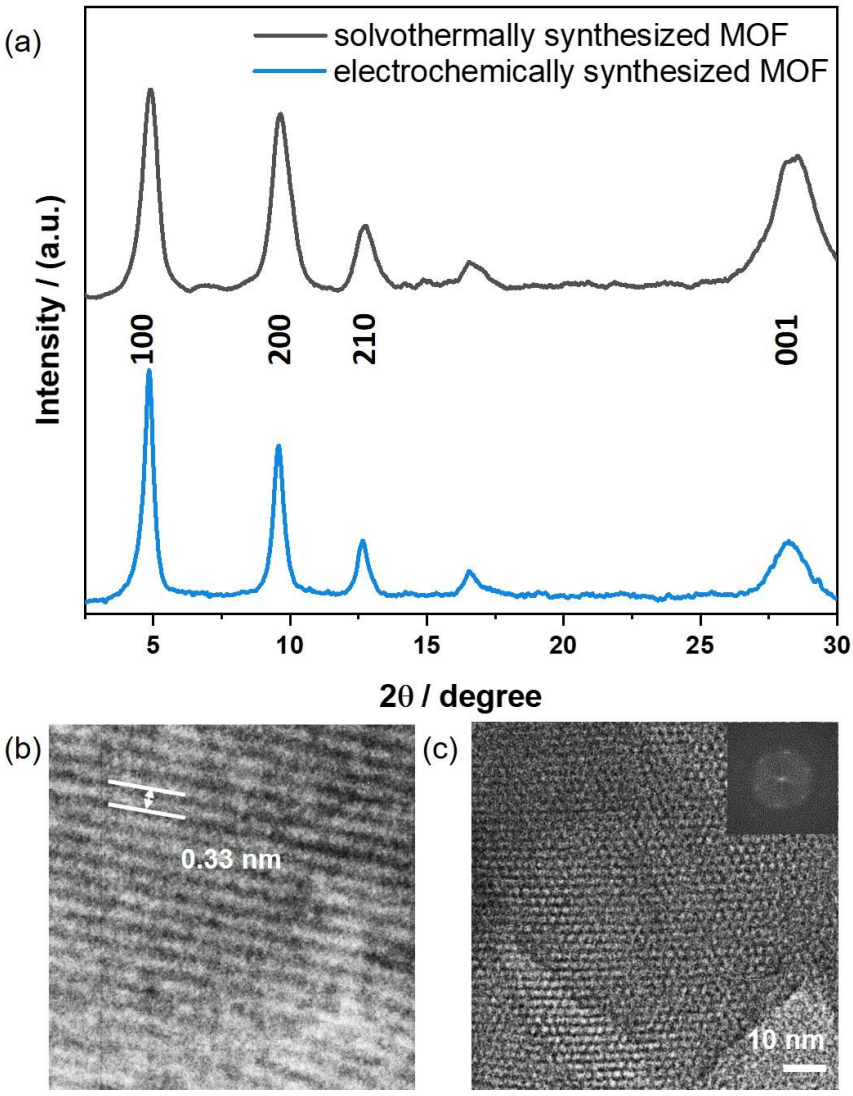

Figure 4. 3: (a) XRD pattern of electrochemically synthesized $Cu_3(HHTP)_2$ powder sample (blue) and solvothermally synthesized $Cu_3(HHTP)_2$ (grey), confirming the formation of $Cu_3(HHTP)_2$ using electrochemical synthesis method (b) HRTEM image of $Cu_3(HHTP)_2$ showing the lattice periodicity of 0.33 nm (c) HRTEM image of $Cu_3(HHTP)_2$ showing the hexagonal structure of $Cu_3(HHTP)_2$.

Notably, the reactions happening on the copper side differ from that occur on the ITO side. On the copper side, by applying 0.43 V on the copper tape, both Cu and HHTP undergo oxidation. The Cu ions released react with the oxidized HHTP, leading to the formation of the $Cu_3(HHTP)_2$ MOF on the Cu tape. During the formation of the $Cu_3(HHTP)_2$ MOF, the HHTP loses 6 H^+ ions and is triply oxidized, resulting in an $HHTP^{3-}$ charge state. In this setup, HHTP loses one electron due to the applied voltage, with further oxidation facilitated by the presence of oxygen. On the other hand, there is no Cu source for ionization on the ITO side, which means the Cu ions have to diffuse from the Cu tape to the ITO to form $Cu_3(HHTP)_2$ on the ITO side. By applying the same voltage on Cu tape and the ITO, there is no electrical gradient between these two surfaces. The concentration gradient enables the diffusion of Cu ions to the ITO surface.

The diffusion of Cu ions may proceed via two potential pathways, either as solvated Cu^{2+} ions or as pre-formed Cu_nHHTP_m coordination complexes. To explore the preferred diffusion state, we first employed a solvo-synthesis approach. Upon the addition of two drops of the Cu salt solution to the HHTP solution in a water–ethanol mixture, an immediate colour change was observed (Figure 4.4a). Since MOF formation is unlikely to occur instantly at room temperature with only copper salt and ligand in solution, and without a base to facilitate deprotonation or higher temperatures to promote the reaction, this suggests that the intermediate complexes are formed before MOF formation. Further understanding on the preferred diffusion process can be provided by UV-Vis measurements.

As shown in Figure 4.4b, the solution of $Cu(NO_3)_2$ exhibits a characteristic broad absorption peak at 810 nm. The UV-Vis spectrum of HHTP shows no distinct absorption features in the range of 370-1400 nm. The spectrum of the resulting MOF displays an absorption peak at 365 nm, corresponding to a π-π^* transition, and a broad peak at 664 nm, attributed to a ligand-to-metal charge transfer transition.[68, 94] Gradual addition of 6.0 equiv. $Cu(NO_3)_2$ per HHTP

resulted in the formation of a new species with peaks at 400 nm and a broad peak at the ligand to metal charge transfer region. This indicates the solvated Cu ions and HHTP molecules initially form an intermediate complex before MOF formation. In fact, the complexes Co-HATP and Ni-HATP before MOF formation have been observed using Scanning Tunnelling Microscopy (STM) in our group recently.[176] The monolayer $Ni_xCo_{3-x}(HITP)_2$ MOFs were deposited on the Au (111) surface in an ultrahigh vacuum, which provides a direct observation of the formation process.

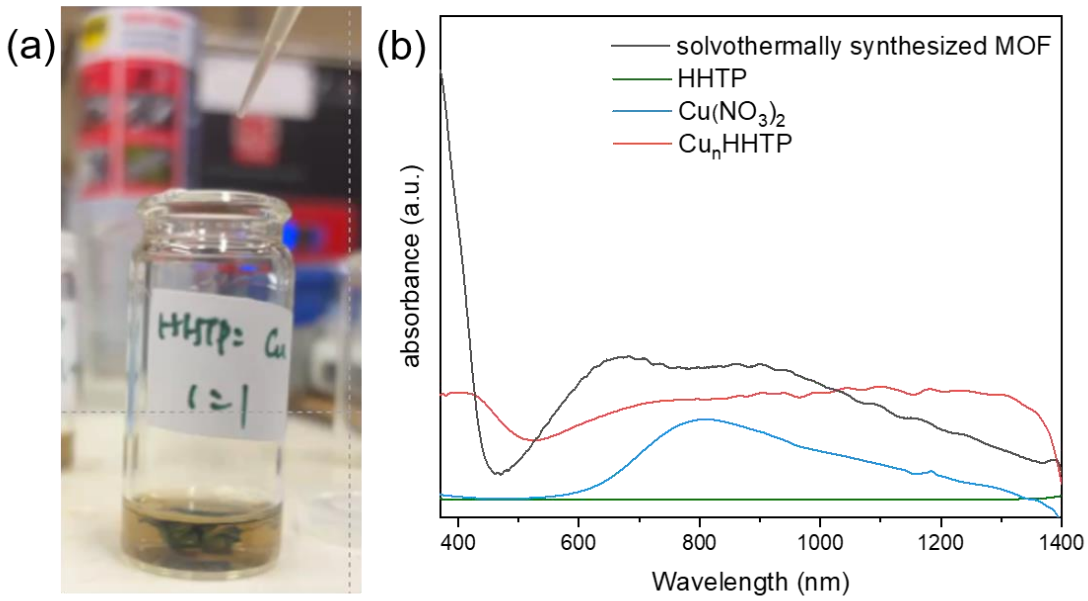

Figure 4. 4: (a) Photograph of HHTP solution after the addition of two droplets of $Cu(NO_3)_2$ solution. The $Cu(NO_3)_2$ solution is light blue, while the HHTP exhibits grey colour. Upon adding $Cu(NO_3)_2$ to the HHTP solution, a dark blue colour immediately observed. (b) UV-Vis spectra of $Cu(NO_3)_2$ (blue), HHTP (green), Cu_3HHTP_2 (grey), and Cu_nHHTP_m complex (red).

After establishing the presence of an intermediate-state diffusion pathway during MOF formation, we further examined the electrochemical processes occurring at the ITO surface. To assess the role of the applied potential, a control experiment was performed in which voltage was applied exclusively to the Cu surface, resulting in a conducting Cu surface but leaving the ITO surface insulating. The formation of $Cu_3(HHTP)_2$ was observed on the Cu side, but not on

the ITO side, indicating that a charged electrode surface is necessary for MOF deposition on the ITO. This suggests that the interaction between reactants and positive charged surface, driven by the redox processes or electrostatic interactions, play a crucial role. One such reaction involves the oxidation of the HHTP ligand. Furthermore, CV analysis of HHTP showed that higher voltages are required to oxidize HHTP once one of its subunits has been oxidized or coordinated.[40, 48] This suggests that the redox process of the diffused intermediate complexes is unlikely to occur on the ITO surface. Therefore, we propose a mechanism for MOF growth in the dual-working-electrode setup, as illustrated in Figure 4.5. In the presence of oxygen, Cu ions oxidized from the Cu tape either form $Cu_3(HHTP)_2$ directly on the Cu tape or are "caught" by the ligand, forming Cu_nHHTP_m complexes in the solution. These complexes then diffuse toward the ITO surface driven by their concentration gradient, where they interact with the positively charged electrode and subsequently grow into a MOF film.

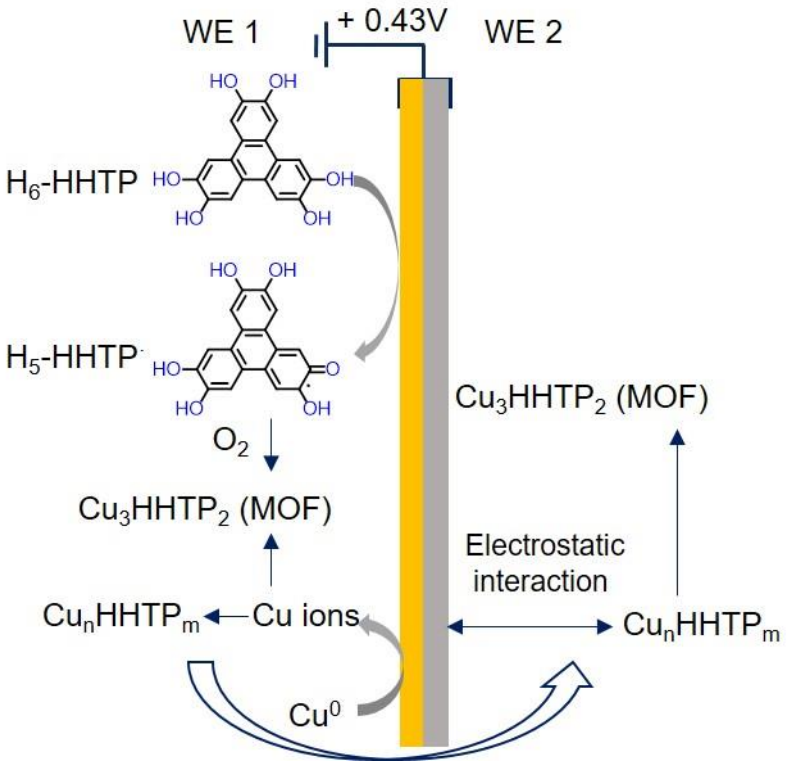

Figure 4. 5: Proposed reactions at the two working electrodes. Oxidation of HHTP occurs on both sides. The main difference is that copper ions are ionized from the Cu side and form complexes, which diffuse to the ITO side, where they lead to MOF formation. The grey arrow indicates oxidation reactions, while the blue arrow represents diffusion.

At the counter electrode, some Cu ions may diffuse into the solution and undergo reduction. Additionally, during the formation of MOF, each HHTP ligand releases $6H^+$ ions upon coordination with Cu. The standard hydrogen electrode potential difference between Cu oxidation and H^+ ion reduction is 0.34V, driving the reduction of these H^+ ions at the counter electrode.[177]

4.3.2 Orientation control

After confirming the successful formation of $Cu_3(HHTP)_2$ using the dual-working-electrode electrochemistry synthesis, we aim to achieve control over the orientation of the film. We experimented with the ligand concentration and found that this gives rise to orientation

differences.[104, 178] In each experiment, the applied voltage remains the same at 0.43V to ensure that the oxidation state of Cu and HHTP, and the released amount of Cu ions remains consistent. We found that $Cu_3(HHTP)_2$ grown from solution containing high ligand concentration and low ligand concentration exhibited remarkably different morphology. The SEM image of $Cu_3(HHTP)_2$ synthesized from a high ligand concentration exhibits vertically grown flakes (Figure 4.6a), while the $Cu_3(HHTP)_2$ film synthesized from a low ligand concentration tends to form laterally along the electrode surface (Figure 4.6b).

XRD measurement was performed to probe the stacking orientation of both $Cu_3(HHTP)_2$ films. As shown in Figure 4.6c, the MOF film synthesized under high ligand concentration exhibited strong diffraction peaks at 4.9°, 9.6°, 12.6°, and 16.6°, corresponding to the (100), (200), (210), and (220) planes, respectively. The presence of these peaks and the absence of a peak at 28° indicate an edge-on orientation of the film (Figure 4.6c, blue).[89] While the film synthesized under low ligand concentration showed a strong diffraction peak at 28°, corresponding to a π-π stacking distance of 0.33 nm (Figure 4.6c, red).[72] This peak was indexed to the (001) plane of $Cu_3(HHTP)_2$, confirming that the 2D layers are face-on oriented. These results confirm the formation of highly oriented and crystalline $Cu_3(HHTP)_2$ films using our electrochemical synthesis method, with high ligand concentration promoting an edge-on orientation, while the low ligand concentration leads to face-on stacking of $Cu_3(HHTP)_2$ (Figure 4.6d). Notably, rather than the broad peak typically seen in solvothermal samples, the electrochemically synthesized film exhibited two distinct and sharp peaks at 28.01° and 28.68°, corresponding to interlayer distances of 0.32 nm and 0.31 nm. The appearance of these two peaks suggests the coexistence of different stacking arrangements within the film, each associated with a slightly different interlayer spacing.

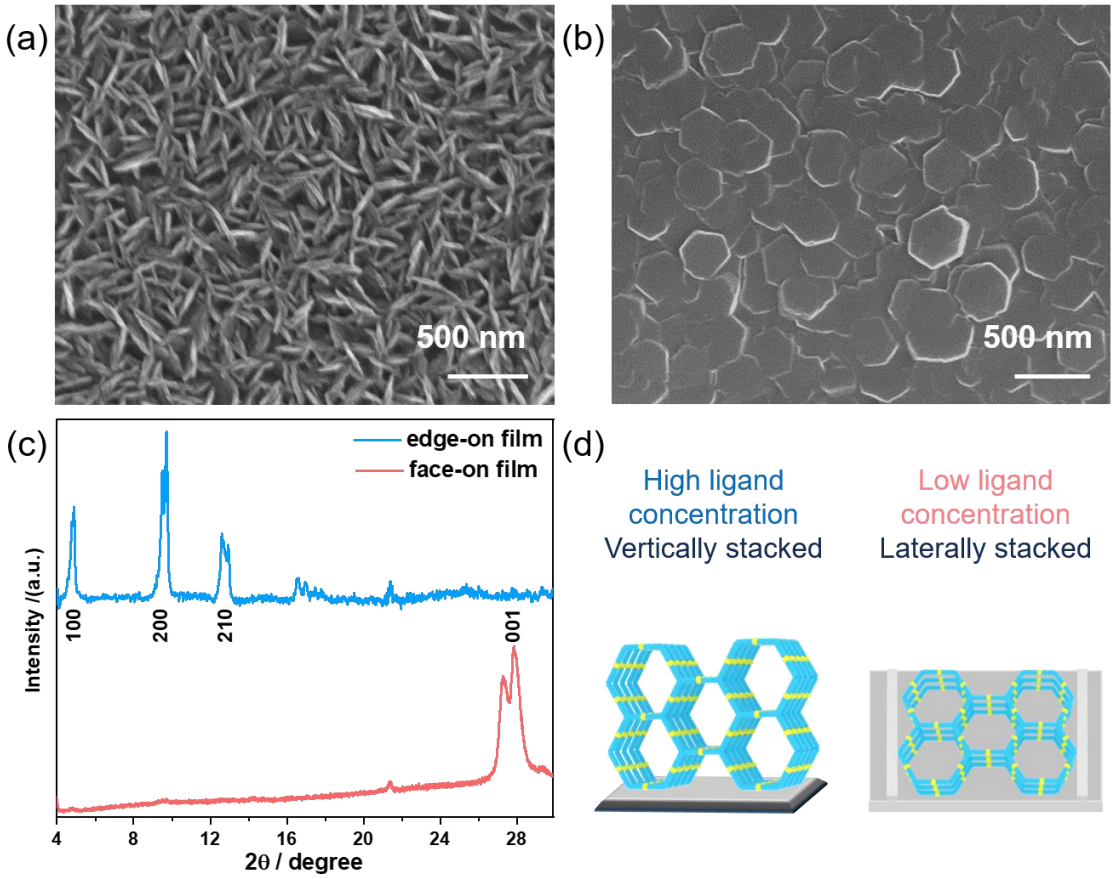

Figure 4. 6: SEM images of $Cu_3(HHTP)_2$ synthesized from (a) high ligand concentration and (b) low ligand concentration for 1 hour. (c) XRD patterns of edge-on (blue) and face-on (red) $Cu_3(HHTP)_2$ films. (d) Proposed model shows the preferential edge-on and face-on orientation on the electrode.

The formation of the oriented $Cu_3(HHTP)_2$ film was conducted by varying the reaction time to study its growth process. In a solution with high ligand concentration, vertically stacked $Cu_3(HHTP)_2$ nano-flakes were formed on the ITO surface after 2 hours of reaction (Figure 4.7a). Thickness of each flake could be increased from about 40 nm to 100 nm by increasing the reaction time (Figure 4.7a, c). Under low ligand concentration, electrochemical deposition for 2 hours led to the formation of a continuous film with flakes, each flake being approximately 500 nm in diameter (Figure 4.7 b). Increasing the synthesis time to 10 hours produced flakes of roughly the same size (Figure 4.7d).

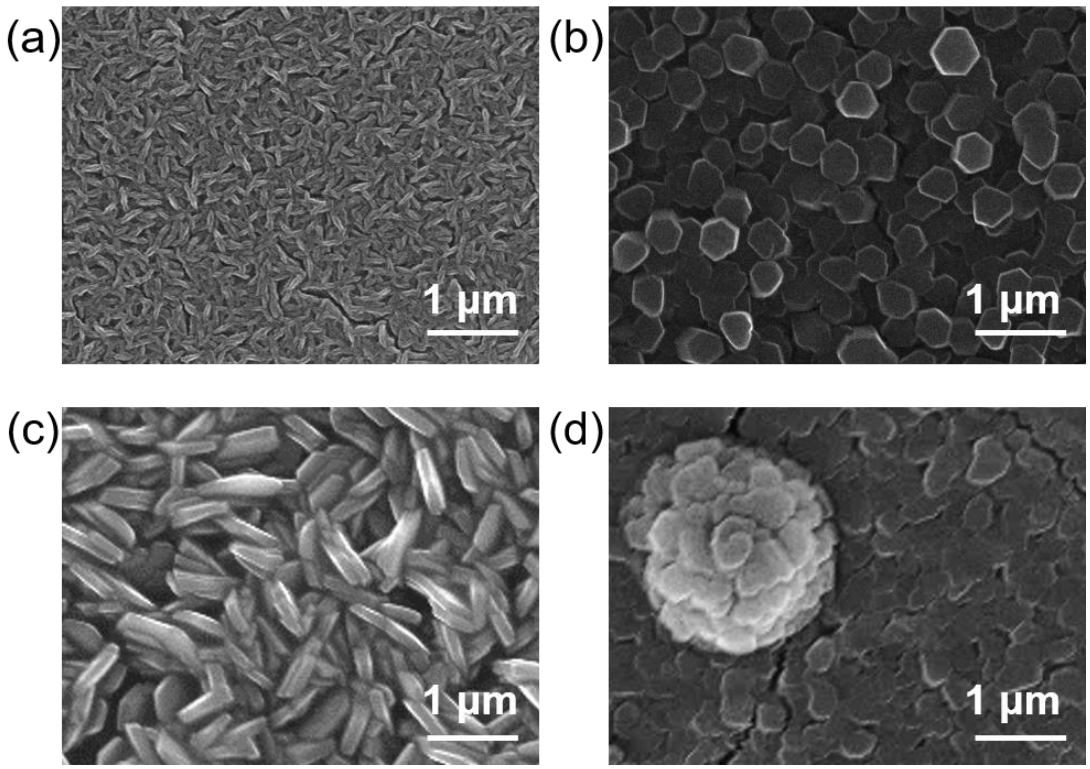

Figure 4. 7: (a, c) SEM images of edge-on $Cu_3(HHTP)_2$ film synthesized for 2h and 10 h. (b, d) SEM images of face-on $Cu_3(HHTP)_2$ film synthesized for 2h and 10 h.

By changing the reaction time, the thickness of both face-on and edge-on film can be tuned. AFM was used to measure the thickness of the oriented film. After 2 hours reaction, the edge-on film shows a thickness of 560 nm (Figure 4.8a), and the face-on film shows a thickness of about 1.5 μm (Figure 4.8c). Extending the reaction time to 10 hours increased the thickness of the edge-on film to 2.5 μm and the face-on film to 9.6 μm (Figure 4.8b, d). These results suggest that growth along the stacking direction is more favorable than along the conjugated plane. Notably, both edge-on and face-on films maintain their orientation across micrometre-scale thicknesses, exceeding the nanoscale thicknesses reported for oriented MOF films. In particular, micrometre-scale thickness control while preserving edge-on orientation has not been demonstrated in MOF systems. The dual-working-electrode strategy overcomes limitations associated with inhibited diffusion of reactants through initially formed dense layer, enabling thickness control on the micrometre scale.[46, 76-77] Interestingly, the film synthesized from low

ligand concentration, which utilized fewer reactants, exhibited greater thickness compared to the film deposited from a high ligand concentration. A possible reason is that the face-on film possesses higher conductivity and a more uniform structure, allowing it to act as fresh electrode for continued growth along the out-of-plane direction, facilitating the consistent formation of new layers and promoting a more uniform deposition process. In contrast, the uneven morphology of the edge-on film may hinder nucleation and crystal growth on its surface, thereby limiting further growth.

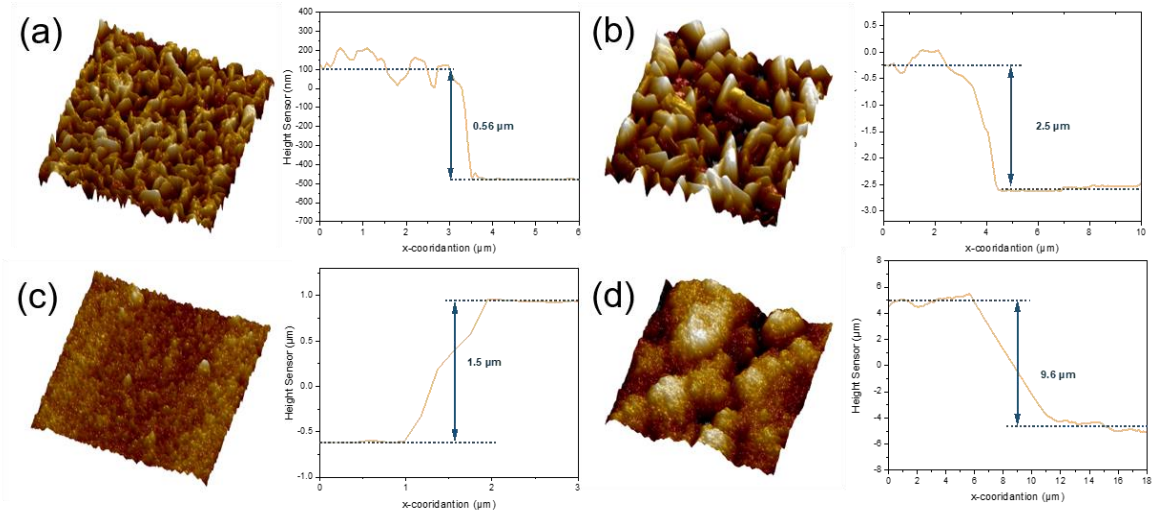

Figure 4. 8: AFM images of the edge-on and face-on $Cu_3(HHTP)_2$ film synthesized for various durations, and the corresponding thickness measurements. (a) edge-on film synthesized for 2 hours, showing a thickness of 560 nm. (b) edge-on film synthesized for 10 hours, with a thickness of 2.5 µm. (c) face-on film synthesized for 2 hours, with a thickness of 1.5 µm. (d) face-on film synthesized for 10 hours, with a thickness of 9.6 µm.

Another factor that influences the growth of $Cu_3(HHTP)_2$ is the applied voltage. The applied voltage potential is related to the oxidation state of HHTP and the electrolysis rate.[46, 83] Under high ligand concentration conditions, edge-on films form at 0.25V and 0.43V (Figure 4.9a, b). However, when the voltage increases to 0.65V, no strong orientation nature was observed (Figure 4.9c). For face-on film, we found that higher applied voltage potential leads to smaller crystal domains, promoting the nucleation of $Cu_3(HHTP)_2$ (Figure 4.9d-f). These results

suggest that a high applied voltage led to increased structural disorder in the MOF film.[77, 179] Furthermore, at 0.65V, HHTP is oxidized from the cat-cat-cat state to the cat-sq-sq state, which may alter its coordination behavior with Cu ions and subsequently affect the formation of an oriented film. (Figure 4.2).

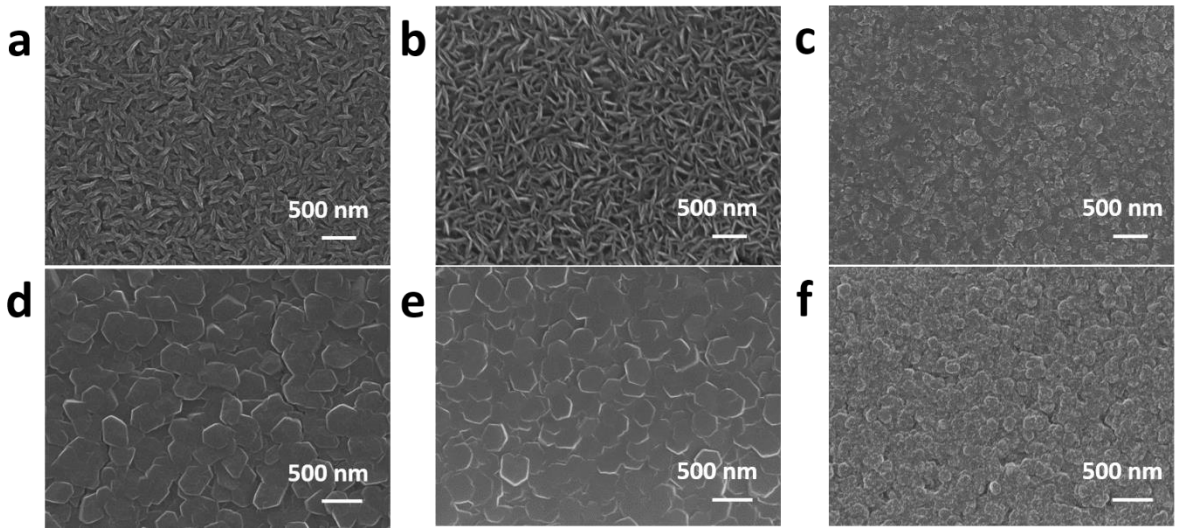

Figure 4. 9: SEM images of $Cu_3(HHTP)_2$ films synthesized under various applied voltage potential. (a-c) $Cu_3(HHTP)_2$ film synthesized from high ligand concentration at 0.25V (a), 0.435V (b), and 0.65V (c). (d-f) $Cu_3(HHTP)_2$ film synthesized from low ligand concentration at 0.25V (d), 0.435V (e), and 0.65V (f).

4.3.3 Oriented growth mechanism

Our findings suggest that high ligand concentration is necessary for the formation of edge-on oriented films. To further understand the growth mechanism of the oriented films, we aim to explore the role of the intermediate complex diffusion by looking into the morphology of $Cu_3(HHTP)_2$ grown on Cu tape under different conditions. SEM images of $Cu_3(HHTP)_2$ grown on Cu tape show a face-on orientation at both high and low concentrations (Figure 4.10), indicating that edge-on film cannot form on the Cu tape, implying that the diffusion process of intermediate complexes to the ITO surface is necessary to achieve an edge-on orientation.

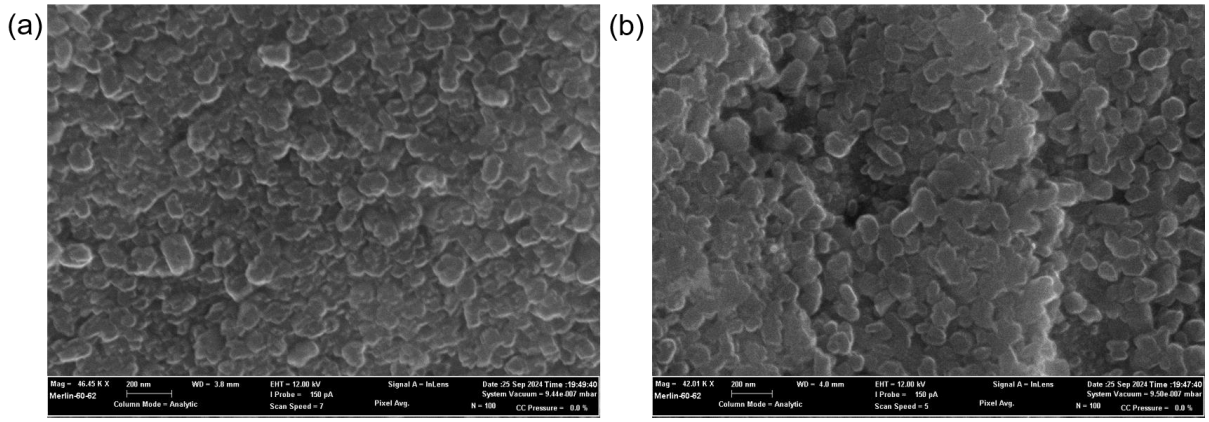

Figure 4. 10: SEM image of the MOF on the Cu tape from (a) high ligand concentration (b) low ligand concentration.

After identifying that intermediate complex formation upon the release of Cu ions, we aim to identify if different complex structures form under various ligand concentration conditions, which lead to the growth of oriented films.

After 30 minutes of electrochemical deposition, the solution close to the ITO surface containing the intermediate complexes was pipetted off. UV-vis spectroscopy measurements were then performed on solutions collected from both high ligand concentration and low ligand concentration conditions. As shown in Figure 4.11, the UV-vis spectra of the electrolyte solution differ from the HHTP, $Cu(NO_3)_2$, and solvothermally synthesized $Cu_3(HHTP)_2$, confirming the presence of intermediate complex. Compared to the $Cu_3(HHTP)_2$, the complex formed under high ligand concentration showed a blue shift of peak from 664 nm to 642 nm, and a decreased intensity in the NIR region. While the complexes formed in low ligand concentration exhibited a red shift, with the peak shifting to 686 nm, and relative high intensity of the peak extending to NIR region. The red shift of the ligand-to-metal charge transfer peak indicated an increased binding number of Cu ions.[166] Furthermore, the increased ratio of peak in the NIR region to the ligand-to-metal charge transfer peak was observed at low ligand complex concentrations, indicating a higher degree of metal-ligand charge transfer and higher

conjugation.[34] The results suggest that HHTP coordinates with a higher number of Cu ions in complexes formed in low ligand concentration solutions. However, identifying these complex structures remains a challenge.

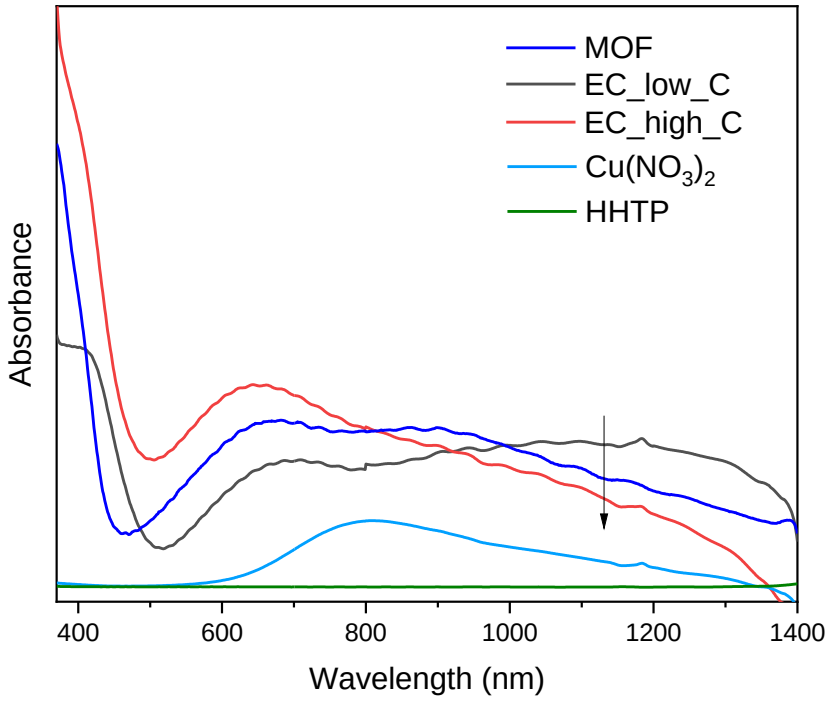

Figure 4. 11: (a) UV-vis spectra of HHTP (green), $Cu(NO_3)_2$ (light blue), $Cu_3(HHTP)_2$ (blue), solution from high concentration electrochemical synthesis condition (red), and solution from low ligand concentration electrochemical synthesis condition (grey). The ratio of the peak intensity in the NIR range to the peak intensity at ~650 nm decreases. (b) UV-vis spectra of diluted solution from high ligand concentration (red) and low ligand concentration (grey).

Overall, we found that different complex structures form in solution before the formation of edge-on and face-on films on ITO. After a 2-hour deposition, the remaining solution was directly used as the electrolyte solution, with the ITO as the working electrolyte in the absence of Cu tape (Figure 4.12a). Remarkably, the continued growth of the MOF film was observed, even after the removal of the Cu tape. The remaining solution still leads to the formation of oriented films. Higher ligand concentrations resulted in edge-on oriented flakes (Figure 4.12b),

whereas low ligand concentration led to laterally oriented flakes (Figure 4.12 c). These results suggest that neither Cu nor HHTP was fully consumed, and the complexes remained stable in the solution.

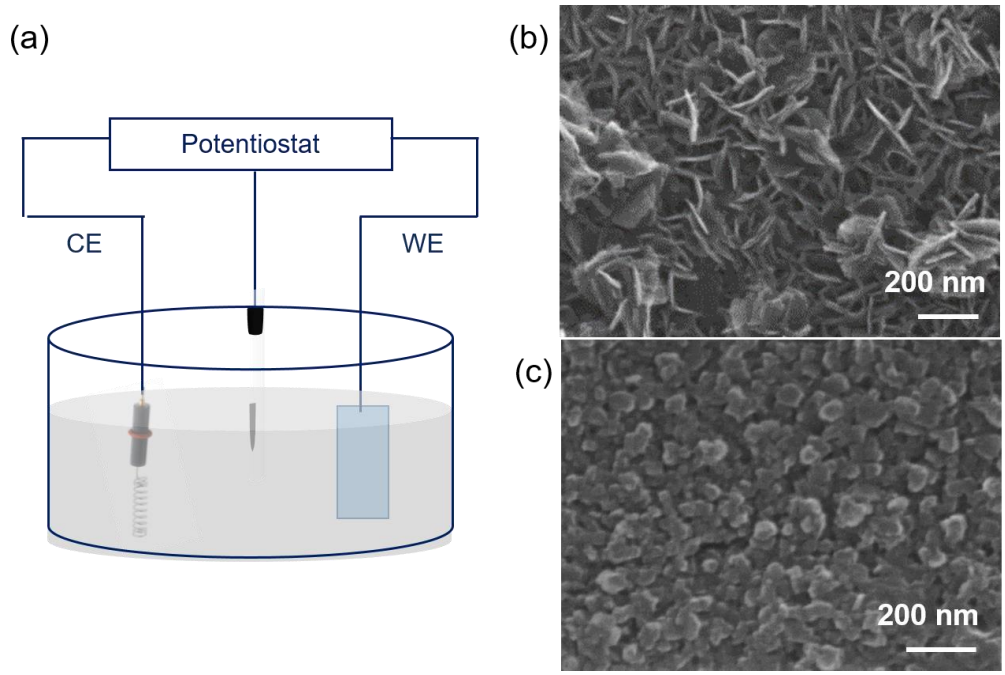

Figure 4. 12: (a) Schematic diagram of the setup using ITO without Cu tape adhered, the solution used is the solution left after 2 hours synthesis using setup shown in Figure 4. (b) SEM image of the deposited edge-on film after 30min deposition (c) SEM image of the face-on film after 30min deposition.

To elucidate the formation mechanism of these oriented films, we propose possible smallest units for the complexes. First, we consider configurations where each HHTP subunit binds with either one or two Cu ions, from this basis, discuss configurations that specify the total number of Cu ions bound to each HHTP molecule. Initially, we ruled out the presence of the mono-deprotonated HHTP subunits, as HHTP catechol subunits typically deprotonate both hydrogen ions to bind with Cu ions, and mono-deprotonated complexes have rarely been reported in solution. Based on these conditions, we propose that each HHTP subunit coordinates with one Cu ion.

Accordingly, we suggest possible structures for the initial complexes formed on the Cu side, denoted as Cu_nHHTP_m. When the Cu-to-HHTP ratio is less than 1, each Cu ion

coordinates with at least one HHTP molecule, leaving no excess solvated Cu ions in solution. In this case, the limited availability of Cu prevents MOF formation, as these configurations saturate the available Cu coordination sites, thereby suppressing MOF growth. Efficient MOF formation requires a Cu-to-HHTP ratio of 1.5. At a ratio of $1 \leq$ Cu-to-HHTP < 3, both Cu_1HHTP_1 and Cu_2HHTP_1 complexes may coexist. This range provides a sufficient concentration of accessible Cu binding sites, enabling further coordination between complexes and facilitating MOF assembly. When Cu-to-HHTP ratio ≥ 3, forming a complex structure of Cu_3HHTP_1, this Cu concentration allows for coordination with both HHTP molecules in solution and between complexes, further facilitating the formation of an extended MOF network.

We hypothesize that in high concentration of HHTP solution, the Cu ions fail to coordinate with all binding sites of HHTP, forming asymmetrical structures that have an in-plane electric dipole moment. These complexes then interact with the charged ITO electrode surface vertically, growing into an edge-on film. In low ligand concentration solution, there is a greater number of fully coordinated Cu_nHHTP_m intermediate complexes, which promotes the face-on orientation of $Cu_3(HHTP)_2$. Our hypothesis is supported by DFT calculations (Figure 4.13). DFT calculations were performed using both the PBE and PBE0 functionals, the same qualitative results were found. For HHTP coordinated with a single Cu atom, the electric dipole moment was 1.25 eÅ within PBE and 1.46 eÅ within PBE0 (Figure 4.13a). Binding two Cu atoms reduces the electric dipole moment of 0.26 eÅ within PBE and 0.1 eÅ within PBE0 (Figure 4.13b), while a fully coordinated HHTP shows no electric dipole moment (Figure 4.13c). The out-of-plane electric dipole moment perpendicular to the Cu_nHHTP_m complex plane remains zero in all cases. These results indicate that, with increasing number of Cu coordination,

there is a decrease in in-plane electric dipole moment of the intermediate complexes which promotes face-on interaction between the complexes and the ITO surface. These complexes subsequently grow into a face-on film.

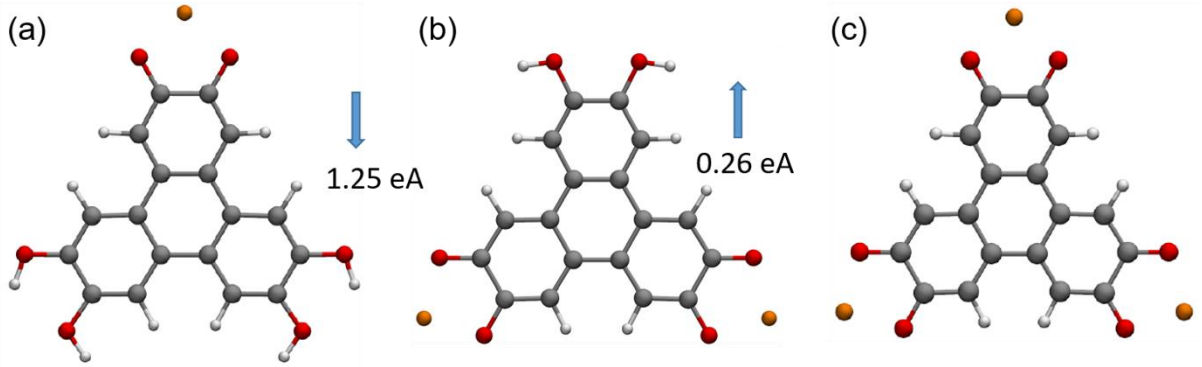

Figure 4. 13: Proposed possible smallest intermediate complex structure with corresponding electric dipole moments calculated using DFT.

To investigate whether the formation of oriented films is dominated by crystal nucleation or growth, we performed a control experiment by switching the synthesis conditions for edge-on and face-on films. As described, a high ligand concentration promotes the formation of edge-on films, and a low ligand concentration results in the formation of face-on oriented films. Using the same setup, an ITO glass with Cu tape on the opposite side was submerged in an electrolyte solution with a high concentration of HHTP ligand, and a voltage of 0.43V was applied for 3 minutes. The combined working electrode was then transferred to a low ligand concentration condition. After 60 minutes of deposition, an edge-on film was observed (Figure 4.14a). Conversely, when the electrode was initially placed in a low ligand concentration solution for 3 minutes under 0.4 V, and then transferred to high ligand concentration condition. After 60 minutes deposition, a face on film was observed (Figure 4.14b). These results show that the film orientation is determined during the initial three minutes of deposition, indicating that the nucleation process plays the crucial role in directing film orientation.

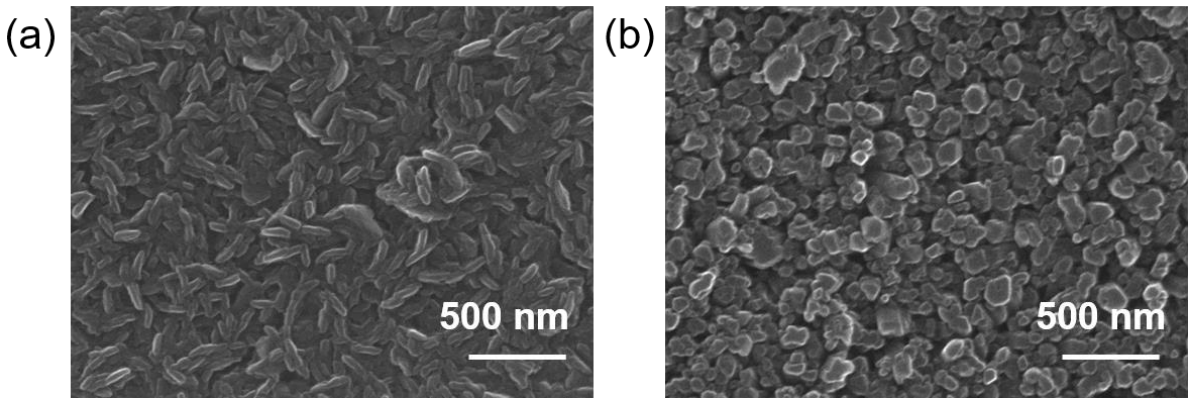

Figure 4. 14: SEM image of (a) $Cu_3(HHTP)_2$ films synthesized in high ligand concentration condition for 3 min, and then switched to low ligand concentration for 1 hour. (b) $Cu_3(HHTP)_2$ films synthesized in low ligand concentration condition for 3 min, and then switched to high ligand concentration for 1 hour.

4.3.4 Investigation of anisotropic conductivity and surface chemistry

The highly orientated 2D MOF enables us to understand the conductivity contribution of interlayer spacing and conjugation plane using conductive AFM (cAFM). This technique measures local conductivity of films with nanoscale resolution, avoiding the effect of inhomogeneity, grain boundaries and contact resistance that would normally be measured in macroscopic conductivity experiments.[95, 180] Charge transport through in-plane and out-of-plane direction can be measured from edge-on and face-on film, respectively (Figure 4.15).

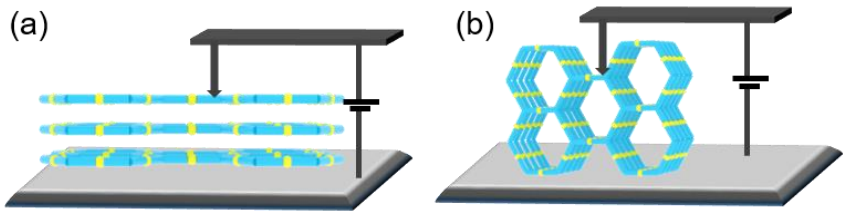

Figure 4. 15: Schematic diagram of the conductive-AFM setup for measuring local conductivity in in-plane and out-of-plane direction for (a) face-on and (b) edge-on film.

Voltages of 1, 2, 3, and 4V were applied to the tip for the edge-on film, while voltages of 3, 4, 5, and 6V were applied to the tip for the face-on film, as the resistance of face-on film is too big to be detected for voltage less than 2V (Figure 4.16b,d). The resulting local vertical conductivity for the edge-on film is 7×10^{-2} S cm^{-1}, while for the face on film is about 7×10^{-5} S cm^{-1} (Figure 4.16). The in-plane charge transport is 10^3-fold higher than the π-π stacking charge transport. These results confirm the contribution of out-of-plane conductivity in the layered 2D MOFs, highlighting the importance of involving orientation for devices with enhanced performance.

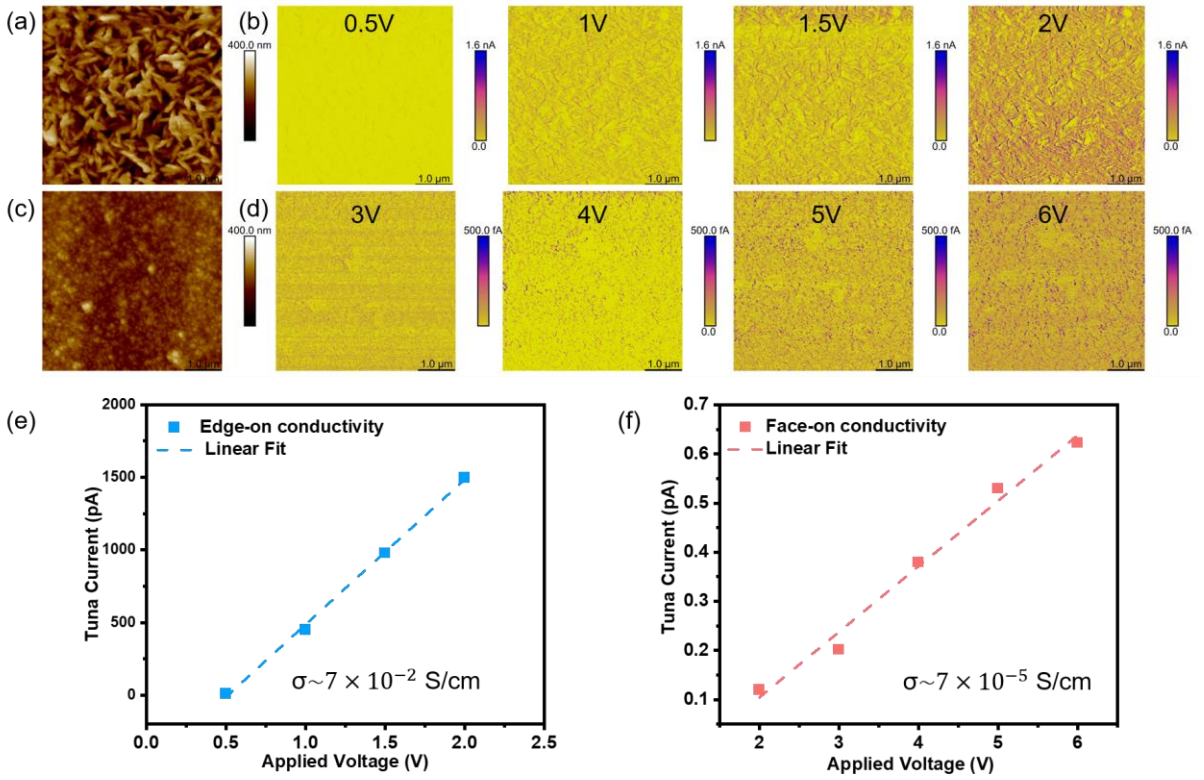

Figure 4. 16: Morphology of two randomly selected area on the edge-on film (a) and face-on film (c). (b) Images of the edge-on film under an applied voltage potential of 0.5V to 2V. (d) Images of the face-on film under a voltage potential of 3V to 6V. Local conductivity through (e) edge-on film and (f) face-on film direction derived from the c-AFM.

XPS measurements were conducted to determine the oxidation state of the elements in the $Cu_3(HHTP)_2$ film. The peak fitting analysis was carried out using CASAXPS software. As shown in Figure 4.17a, the Cu spectrum shows a strong peak at 934.8 eV, corresponding to Cu^{2+}, along with a weak peak at 932.5 eV, suggesting the presence of Cu^{+} or Cu, the absence of Cu metal peaks in the PXRD pattern indicates that no detectable Cu metal is formed.[38] Both edge-on and face-on film show low amount of Cu^{+}, likely originating from structural defects, which suggests a well-coordinated structure.[26, 42] The O 1s spectra indicates the coexistence of C-O and C=O bonds, showing that catechol is partially oxidized to semiquinone state in the HHTP ligand during coordination with Cu (Figure 4.17b).[21, 46] These XPS results show the well-coordinated structure of $Cu_3(HHTP)_2$ film, with no obvious differences observed in the oxidation state between the oriented films.

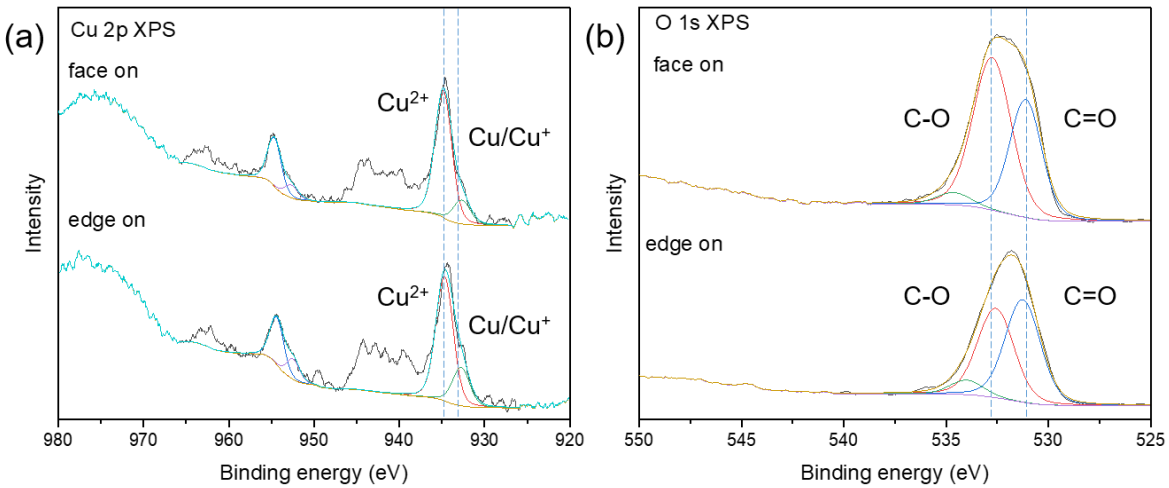

Figure 4. 17: XPS spectra of the face-on (top) and edge-on (bottom) $Cu_3(HHTP)_2$ films on ITO substrate. (a) Cu 2p, (b) O 1s, and (c) C1s are shown. The experimental data (black curve) is fitted, with peak assignments are labelled.

4.4. Conclusion and outlook

In conclusion, we developed a dual-working electrode electrochemical synthesis method to fabricate $Cu_3(HHTP)_2$ films, enabling direct MOF growth on the electrode. This setup allows the oxidation of the metal and the MOF formation to occur at separate interfaces. By tuning the ligand concentration, highly oriented edge-on and face-on $Cu_3(HHTP)_2$ was achieved on the ITO surface. Our investigation into the growth mechanism of oriented $Cu_3(HHTP)_2$ under different ligand concentration emphasized the importance of the intermediate products formed before MOF formation. The highly oriented edge-on film and face-on film exhibits anisotropic conductivity. The local conductivity along the conjugation plane was found 10^3 times higher than that along the stacking direction. This study presents a new strategy for depositing oriented 2D MOF films on electrodes, providing understanding into their growth mechanism. These results provide further insight into the design and synthesis of 2D MOF films with directed charge transport pathways for electronic devices.

The main limitation of employing the dual-working-electrode setup is coordinating the oxidation potentials of both the metal and ligand. For HHTP, attempts to use metals like Zn or Mg as working electrode in the same setup were unsuccessful. The rapid oxidation of Zn or Mg led to a fast reaction with HHTP, resulting in the formation of large, detached crystals, with no obvious structures formed on the ITO side. The same synthesis conditions were also ineffective for forming $Cu_3(HITP)_2$. During the synthesis of $Cu_3(HITP)_2$, oxygen bubbling was found to be necessary, suggesting that the reaction requires an additional oxidizing environment for successful MOF formation.

Chapter 5

Sensing behaviour of oriented films

Two-dimensional electronically conductive metal-organic frameworks (2D-MOFs) can be used as the active material in chemiresistive gas sensors. An important step to maximise the effectiveness of these devices is to optimise the interaction between the MOF and the analyte molecules that is being targeted. This is especially relevant for stacked 2D MOF films where the structure and electrical conductivity are highly anisotropic. It is therefore important to consider the orientation of 2D MOFs when applied as gas sensing device.

This chapter describes the in-situ synthesis of $Cu_3(HHTP)_2$ films between interdigitated electrodes (IDE) with controllable edge-on and face-on orientation employing the method detailed in Chapter 4 and explores their use as active materials in chemiresistive gas sensors. Our ability to control the orientation of the MOF film enables us to optimize the gas sensor response to be able to measure ammonia in the part per billion (ppb) range. To further investigate potential structural or chemical changes in the oriented films, XRD, XPS, and FT-IR analysis were performed before and after ammonia exposure.

5.1 Introduction

The conductivity and permanent porosity of 2D MOFs make them ideal candidates for ultrasensitive chemiresistive gas sensors.[1] These sensors rely on a change in conductivity with the adsorption of a chemical analyte.[101, 106] For example, if a p-type MOF is exposed to the electron donating molecule NH_3 then the resistance of the MOF will increase as a function of the amount of NH_3 adsorption.[112] The performance of these devices is greatly influenced by the properties of the MOF film, such as morphology, thickness, orientation, and surface roughness.[64, 72] Design strategies include optimizing their properties by increasing surface roughness, maximizing specific surface area, achieving dense inter-particle packing, and minimizing electrode-MOF interface resistance.[64, 107, 181] Among these factors, the orientation of 2D MOF crystals may play a particularly critical role in determining gas sensing performance.

When a polycrystalline film of a 2D stacked MOF is created for a gas sensing device, the orientation of the crystals affects the sensing properties, as the interaction between an analyte molecule and the crystal surface termination along the stacking direction is very different from the interaction perpendicular to the stacking direction.[69, 182-183] However, published work to date generally only considers the overall response of 2D MOF to analytes without taking into account the anisotropic structure and specific gas diffusion pathways of these materials. This is despite the known orientation-dependent conductivity of the film.[110, 172] Additionally, understanding of the structure-property relationships in 2D MOFs remains limited within the context of their use as chemiresistive sensors.[72, 110, 112-113] In chapter 4, we presented the fabrication of a highly oriented $Cu_3(HHTP)_2$ film, synthesized directly on ITO glass with controllable lateral and vertical orientations. In this chapter, we apply the same method to fabricate oriented films on IDEs and explore their performance as chemiresistive gas sensing

devices. The sensing response and reproducibility of the edge-on and face-on films are investigated, revealing that the edge-on film shows a greater response and improved sensing reproducibility compared to the face-on film. This comparison provides a design direction for further optimizing the 2D MOF-based chemiresistive sensing device. Additionally, the interaction between ammonia and $Cu_3(HHTP)_2$ has been examined using XPS, FT-IR, and XRD to understand the underlying sensing mechanisms.

5.2 Experimental section

5.2.1 Fabrication of oriented MOF film-based sensors

The oriented film was grown on an IDE via electrochemical deposition using a conventional 3-electrode set-up, with a platinum counter electrode and an Ag/AgCl reference electrode. The electrolytic cell itself was a beaker with a 10 cm diameter. Cu tape was adhered to the opposite side of the IDE, which is coated with 150 nm of platinum on a glass substrate. Each IDE finger features a width of 5 µm with gap of 5 µm between the fingers. For the edge-on film, 2.6 mM HHTP powder and 0.02 M Tributylmethylammonium methyl sulfate (TBMAMS) were dispersed in mixed solution of 4:1 water and ethanol. For the face-on film, 1.3 mM HHTP powder and 0.02 M TBMAMS were dispersed in m in mixed solution of 4:1 water and ethanol. The solution was then sonicated for 5 min before synthesis. The electrochemical deposition takes one hour. The final film on the IDEs was washed using acetone.

5.2.2 Sensing experiments

Sensing experiments were performed in a stainless-steel gas-sensing chamber as described in Chapter 3. The flow rates from individual gas cylinders were regulated by digital mass flow

controllers, allowing dry N_2 and NH_3 gases to be mixed before entering the chamber. Ammonia gas concentration was controlled by tuning the relative flow rates of the two mass flow controllers, with the total flow rate maintained at 500 sccm. In each experiment, a DC voltage of 1.0 V was applied to the sensing device, and the current changes were measured using BenchVue software. Before each experiment, nitrogen gas was flowed through the chamber for one hour until the sensor baseline stabilized. Sensors were then exposed to varying ammonia concentrations for 30 seconds. After each exposure, ammonia was removed from the chamber, and the nitrogen was introduced for a variable period until the baseline fully recovered.

5.3 Results and discussion

5.3.1 Synthesis and Characterization of oriented MOF films

The $Cu_3(HHTP)_2$ film was synthesized onto the IDE using the method described in Chapter 4. HHTP powder and tributylmethylammonium (TBMAMS) as the electrolyte are dissolved in the mixture of deionized water and ethanol. A piece of copper tape was taped at the opposite of the IDE and immersed in the solution. $Cu_3(HHTP)_2$ films were electrochemically synthesized at different ligand concentrations for 90 min. The successful synthesis of oriented $Cu_3(HHTP)_2$ films has been confirmed using X-ray diffraction (XRD). The oriented films for XRD measurements were synthesized for 12 hours to achieve a detectable thickness. As shown in Figure 5.1, the XRD spectrum of both electrochemically synthesized $Cu_3(HHTP)_2$ films on IDE shows peaks at about 4.9°, 9.6°, 12.7°, and 28°, corresponding to the (100), (200), (210) and (001) planes of $Cu_3(HHTP)_2$, respectively.[57] The XRD patterns for both edge-on and face-on films along with previously reported $Cu_3(HHTP)_2$ MOF structures.[57] The edge-on film shows strong peaks at about 4.9° and 9.6°, indicating that the MOF film is laterally stacked.[89] While the face-on film shows dominant peak at 28°, indicating a stacking direction along the c-axis.

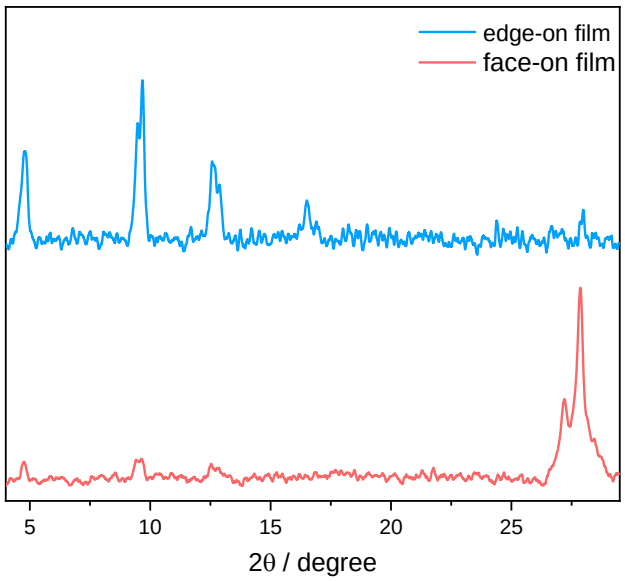

Figure 5. 1: XRD pattern for the $Cu_3(HHTP)_2$ MOF in edge-on (blue) and face-on (red) orientations. The presence of (100), (200), (210) and (001) planes confirming successful MOF formation, and variation in peak intensities suggest different crystal orientations for each film.

SEM was used to characterize the morphology and thickness of the oriented $Cu_3(HHTP)_2$ films. As shown in Figure 5.2a**,** in a solution with high ligand concentration, $Cu_3(HHTP)_2$ nano-flakes form an edge-on film. After 90 minutes deposition, each vertically stacked flake is about 50 nm in thickness, and the overall film thickness is about 440 nm (Figure 5.2b). While at low ligand concentration, the $Cu_3(HHTP)_2$ flakes tend to grow laterally along the electrode surface, forming a continuous face-on film. The face-on flakes have a diameter of about 400 nm, and the total film thickness is about 660 nm (Figure 5.2 c, d).

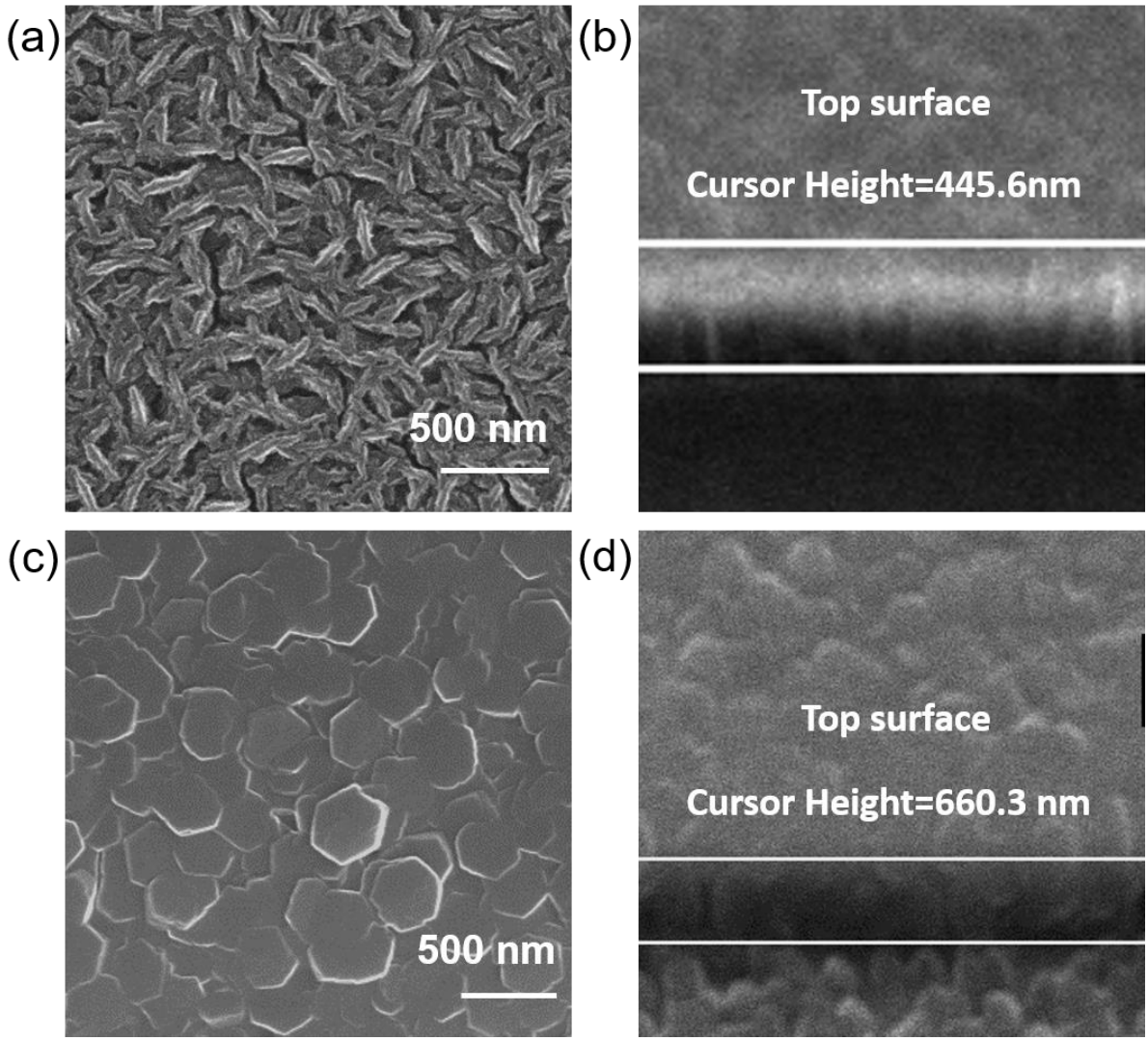

Figure 5. 2: SEM images of (a) edge-on films synthesized for 90 minutes, with corresponding thickness measurement in (b). (c) SEM images of face-on films synthesized for 90 minutes, with thickness measurement shown in (d).

5.3.2 Chemiresistive gas sensing performance of oriented film

The highly oriented 2D MOFs with anisotropic conductivity and structural properties, motivated us to explore the sensing behaviour of both edge-on and face-on oriented films. The sensors were tested in a gas flow chamber, as described in our previous work.[161, 184] A constant potential of 1 V was applied to the devices, and the current was monitored as the gas flow was modulated between pure N_2 and an NH_3/N_2 mixture. Initially, the sensors were exposed to N_2 flow until a stable baseline was achieved, then they were exposed to diluted ammonia for 30 s.

Upon ammonia exposure, the sensor resistance increased as the ammonia is an electron-donating molecule which results in a reduction of the hole charge carries in the p-type MOF. Once the ammonia flow was stopped and the sensors were exposed to pure N_2 flow, the resistance decreases again, gradually recovering toward the original baseline.

Initially, both sensors were exposed to 500 ppb ammonia for 30 seconds. As shown in Figure 5.3a and b, both sensors reached saturation within this short exposure period. The response time, defined as the duration required to reach 90% of saturation, was 18 seconds for the edge-on and 25 seconds for the face-on film.To futher analyze the sensor performance, resistance changes relative to the initial resistance were calculated as the response ($\Delta R/R_0 \times 100\%$). As shown in Figure 5.3c, the edge-on film showed a much stronger response to 500 ppb ammonia, reaching 8.5%, compared to 0.13% for the face-on film. The recovery time was about 40 minutes for the edge-on film and around 12 min for the face-on film. However, the baseline resistance level in the face-on film is decreasing over time, which may affect the accuracy of its recovery time measurement.

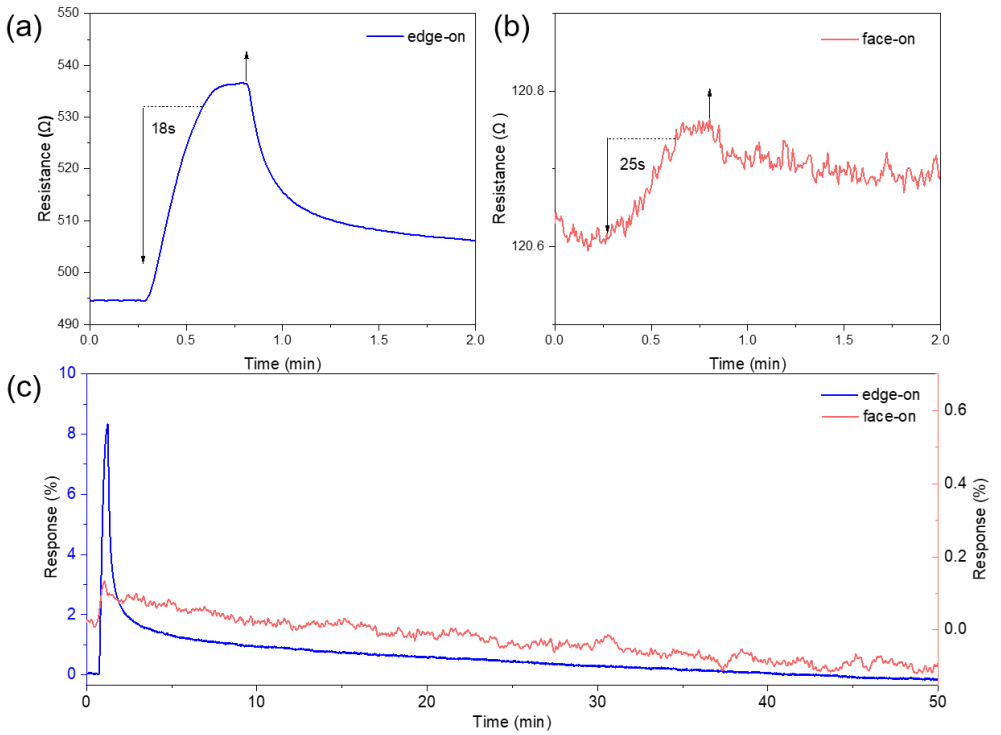

Figure 5. 3: Sensing performance of (a) edge-on film and (b) face-on film upon exposure to 500 ppb ammonia for 30s. (c) Comparison of sensor response, defined as $\Delta R/R_0 \times 100\%$, for the edge-on film (blue line, left axis) and face-on film (red line, right axis).

We then exposed the sensors to 20 cycles of 500 ppb ammonia to test response reproducibility, with a time interval of 50 min between each exposure (Figure 5.4 a, b). The edge-on film displayed consistent, reversible resistance changes for 20 cycles. Conversely, the face-on film's response was nearly undetectable above the noise level after 10 exposures, suggesting saturation of irreversible binding sites or possible structural changes. Additionally, a temperature change of several degrees during measurement, might have led to the baseline drift.

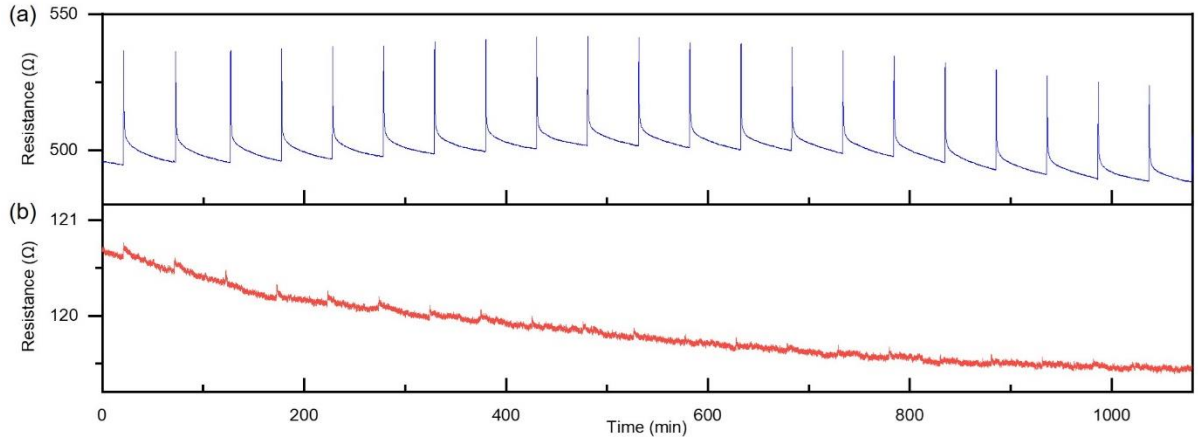

Figure 5. 4: Stability performance of (a) edge-on and (b) face-on sensors to 20 exposure cycles. (500ppb ammonia, 30s exposure, 50 min nitrogen recovery).

The response of both the face-on and edge-on films to 500 ppb ammonia was calculated and is shown in Figure 5.5. After 20 cycles, the edge-on film exhibited a decrease in response from 8.5% to 7.3%, demonstrating reasonably good reproducibility. The face-on film showed a more significant decrease from 0.13% to 0.06%. These results indicate that the edge-on film, perfoms more effectively than the face-on film, offering both a better response and better reproducibility. We therefore only further investigated the sensing behavior of the edge-on oriented film.

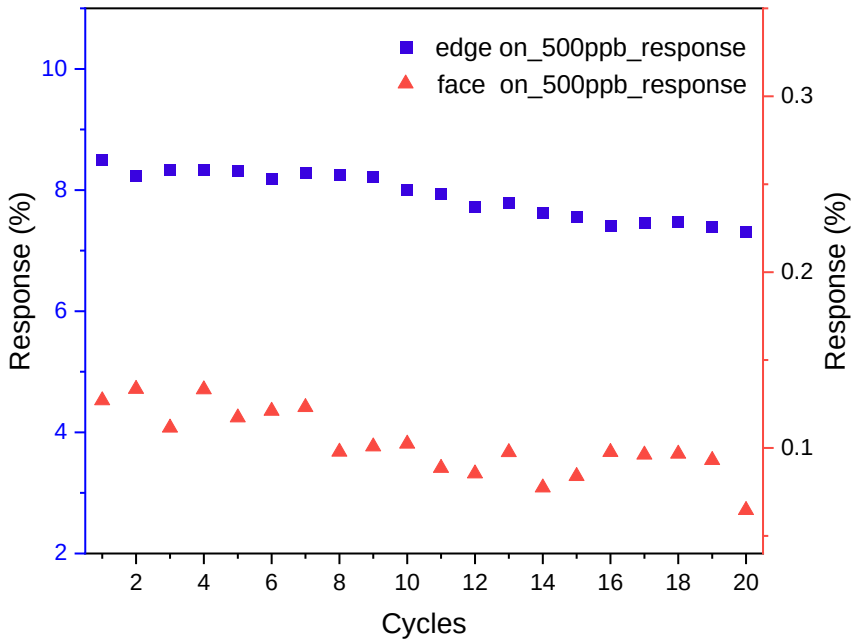

Figure 5. 5: Response of edge-on film and face-on films, during 20 500ppb NH_3 exposure cycles.

To determine edge-on film sensitivity to NH_3 the sensor was exposed to different concentrations of ammonia. Figure. 5.6 shows the response and recovery curves of the edge-on $Cu_3(HHTP)_2$ film when exposed to ammonia concentrations of 10, 5, 2, 0.2 part per million (ppm) for 30 seconds. As the concentration of ammonia is increased from 0.2 ppm to 10 ppm, the response of the edge-on film sensor increases from 1.2% to 29% (Figure 5.6a). The calculated response is plotted as a function of the concentration of ammonia. The slope of the fitted line represents the sensitivity. As shown in Figure 5.6b, the edge-on $Cu_3(HHTP)_2$ film demonstrates a sensitivity of 5.04 ppm^{-1}. The film exhibits a non-linear response to varying ammonia concentrations. In an ideal sensor, the sensor response should display a linear relationship between response and concentration, with the fitted line passing through the origin, indicating that the sensor shows no response at a concentration of zero. However, previous studies have shown that MOF-based sensors, including $Cu_3(HHTP)_2$, often exhibit non-linear behaviour and we fitted our data using the formula $y=ax+bx^{1/2}+cx^{1/3}$.[45, 72, 113]

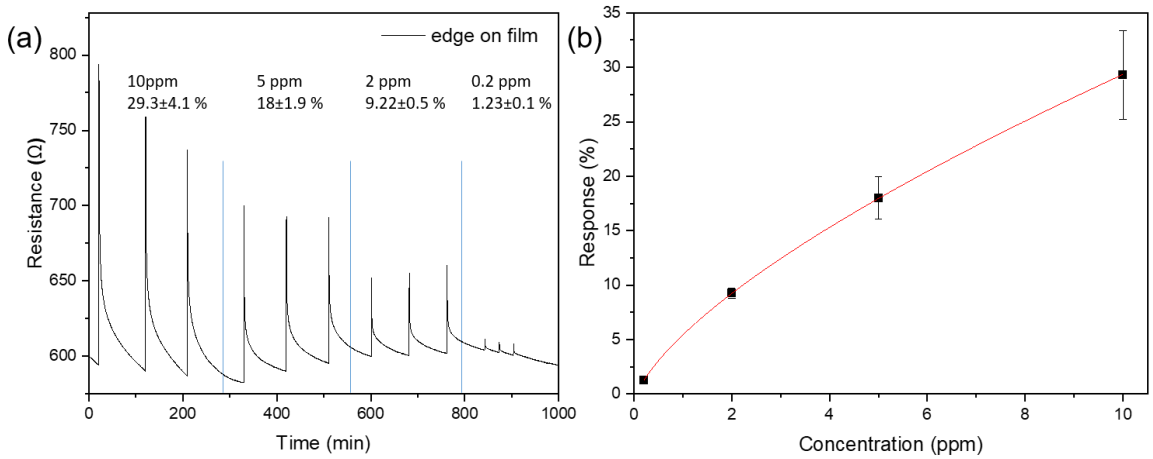

Figure 5. 6: (a) Resistance as a function of time for the edge-on film on exposure to different concentrations of ammonia for 30s. (b) Sensor responses as a function of ammonia concentration for the edge-on sensor, the red line is the fitting curve using equation $y=ax+bx^{1/2}+cx^{1/3}$.

Due to the non-linear response of the edge-on $Cu_3(HHTP)_2$ film, we evaluated its response to low concentrations of ammonia to determine the limit of detection (LOD). The film demonstrated a high and consistent 0.7 ± 0.08% response to 50 ppb of ammonia over 10 cycles. Using the 3σ/sensitivity equation, the LOD was estimated to be approximately 20 ppb. Notably, a measurable response was still observed at concentrations as low as 10 ppb, as shown in Figure 5.7b. This behavior aligns with the sensor's non-linear response characteristics and suggests that the LOD is more reliably estimated by considering both the calculated value and the experimentally observed response at the lowest detectable gas concentrations. To the best of our knowledge, it is one of the most sensitive room temperature NH_3 chemiresistive sensing materials among all reported results (Table 5.1). This suggests that the design strategy, which incorporates an edge-on orientation and a highly homogeneous structure of the electrochemically synthesized $Cu_3(HHTP)_2$ film directly synthesized on an IDE, leads to excellent sensitivity towards ammonia.

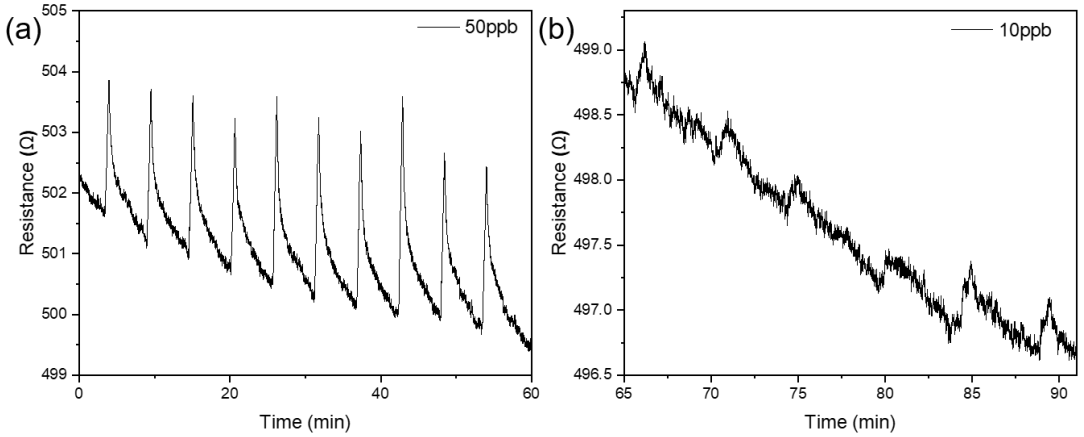

Figure 5. 7: (a) Resistance vs time data for10 cycles of 50 ppb ammonia for 30st on edge-on film. (c) Resistance vs time curve of six cycle of 10 ppb ammonia measurement for an edge-on film sensor.

Table 5.1: Room temperature ppb-level chemiresistive sensing of NH_3.

Material	Preparation method	LOD (ppb)	Ref.
$Cu_3(HHTP)_2$	Chronoamperometry	20	This work
$Cu_3(HHTP)_2$	Templated layer-by-layer	780	181
$Cu_3(HHTP)_2$	Layer-by-layer	500	72
$Cu_3(HITP)_2$	Solvothermal	500	45
Cu-HHTP-THQ	Solvothermal	20	114
Zn-HHTP-Hierarchical film	Immersion	40	185
Polypyrrole	Chronoamperometry	10	184
Nanostructured Polypyrrole	Chronoamperometry	70	161
$Mo_{0.5}W_{0.5}S_2$	Sonication exfoliation	500	186

5.3.3 Interaction mechanisms between ammonia and MOF film

Significant efforts have focused on characterizing the structure-property relationships of 2D MOFs within the context of their use as chemiresistive sensors.[72, 110, 112-113] Various spectroscopic methods, including infrared reflection absorption spectroscopy (IRRAS), EPR, and XPS, have been employed to investigate the chemical changes in 2D MOFs upon ammonia exposure.[110, 113, 187] These studies show that the gas exposure induced chemical changes due to the weak Bronsted acidity/ Lewis acidity and redox behavior of the Cu^{2+} ion.[110, 113, 187] Structurally, Rubio-Giménez et al. suggested that NH_3 interacts directly with the Cu^{2+} metal centres leading to slight distortions of the interlayer spacing.[112]

In this work, the edge-on and face-on films exhibit distinct differences in both sensing responses and reproducibility. However, both show partially reproducible responses to varying extents. We therefore hypothesize that permanent changes may occur in the film after ammonia exposure. To investigate ammonia induced changes in $Cu_3(HHTP)_2$, we first performed CW-EPR on pristine $Cu_3(HHTP)_2$ powder and the $Cu_3(HHTP)_2$ powder after exposure to 10 ppm ammonia for 30 min.

After NH_3 exposure, a new half-field signal appeared (Figure 5.8, inset bottom left), indicating the emergence of magnetic interactions between Cu^{2+} centres and newly coordinated species. Additionally, a new signal observed in the NH_3-treated sample (Figure 5.8, inset top right) is consistent with σ-type bonding involving sp^3-hybridized nitrogen, characteristic of coordinated ammonia.[188] Together, these observations suggest that NH_3 remains bound to some Cu centres.

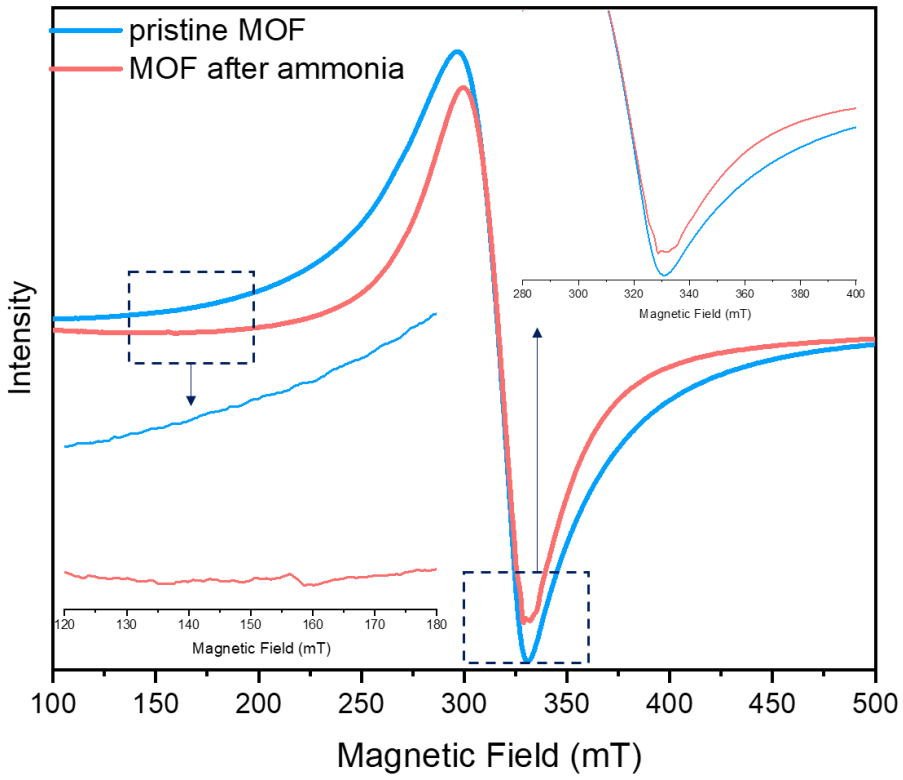

Figure 5. 8: X-band EPR of Cu_3HHTP_2 at 100K under pristine conditions (blue) and after NH_3 treatment (red). The treated sample shows the emergence of a new half-field signal (inset, bottom left) and an additional signal (inset, top right), indicative the interaction between Cu^{2+} and NH_3.

After gaining insight into the interaction between MOF and ammonia, we next aim to understand the impact of the oriented film on these interactions. To investigate whether the above discussed reduction of Cu^{2+} various between the two oriented films, XPS measurements were performed. As shown in Figure 5.9 (a, c), both films exhibit a prominent peak at 934.8 eV, which corresponds to Cu^{2+}, along with a weak peak at 932.5 eV, suggesting the presence of Cu^{+}.[38] The O 1s spectra further show the coexistence of C-O and C=O bonds (Figure 5.9 b, d).[21, 46] However, no significant changes in oxidation states of Cu and O were observed between the two films. Additionally, nitrogen remained undetectable in all samples.

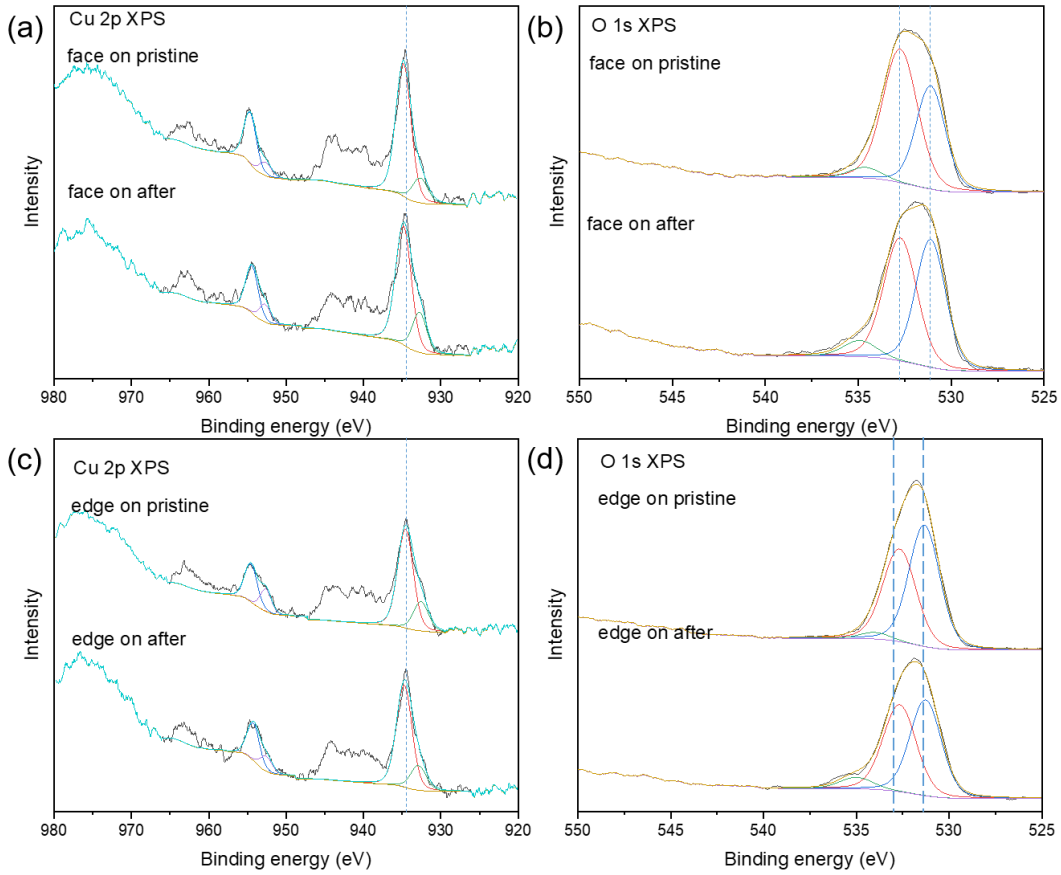

Figure 5. 9: (a, b) High resolution XPS spectra for the face-on film, shown in both pristine state and after 30 minutes of exposure to 10ppm ammonia. (c, d) High resolution XPS spectra for of the edge-on film, shown in its pristine state and after 30 minutes of exposure to 10ppm ammonia. Peaks corresponding to Cu and O are labelled.

We then investigated whether the two films show changes in molecular bonding environment using Attenuated Total Reflectance-Fourier Transform Infrared (ATR-FTIR) spectroscopy. As shown in Figure 5.10, ATR-FTIR spectrum of HHTP powder (grey) shows C=O, C=C and C-O vibration peaks at 1621 cm^{-1}, 1432 cm^{-1} and 1292 cm^{-1} respectively.[89, 110] When coordinating with Cu, both films exhibit a new peak at 688 cm^{-1}, attributed to the stretch of Cu-O.[72] Notably, the edge-on film shows an additional peak at 808 cm^{-1}, which is assigned to the Cu-O scissoring stretching vibration.[110, 189] The face-on film presents a broad peak at 1621 cm^{-1}, indicating more unsaturated C=O groups existing on the $Cu_3(HHTP)_2$ surface.[72, 190] After 10 minutes of ammonia exposure, the edge-on film shows no obvious changes, while the face-on film exhibits

an additional peak at about 808 cm^{-1} and a decrease in the intensity of the C=O peak. This indicate that the face-on film undergoes more significant chemical changes upon ammonia exposure compared to the edge-on film.

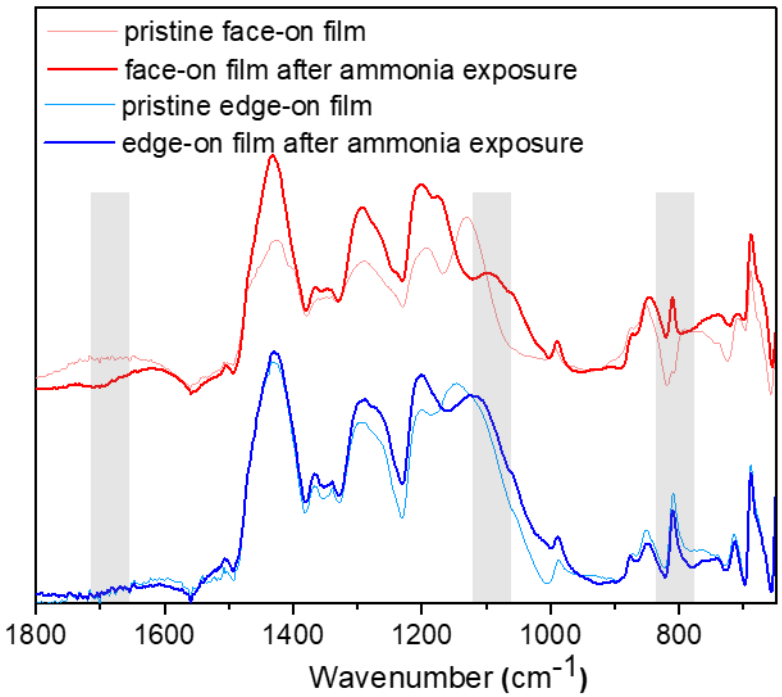

Figure 5. 10: ATR-FTIR spectra for the pristine edge-on film (light blue) and after 30 minutes of exposure to 10 ppm ammonia, and spectra for the pristine face-on film (light red) and after 30 minutes of exposure to 10 ppm ammonia.

To determine whether structural changes occur in the oriented films after ammonia exposure, XRD measurements were conducted on both face-on and edge-on films before and after exposure. As shown in Figures 5.11a and 5.11b, no peak shift is observed in either film orientation. Since the peak near 28°, assigned to the (001) plane, is not well-defined in the edge-on film, we scraped off a powder sample for additional XRD analysis to examine potential shifts in the stacking direction. The powder sample also showed no significant change (Figure 5.11c).

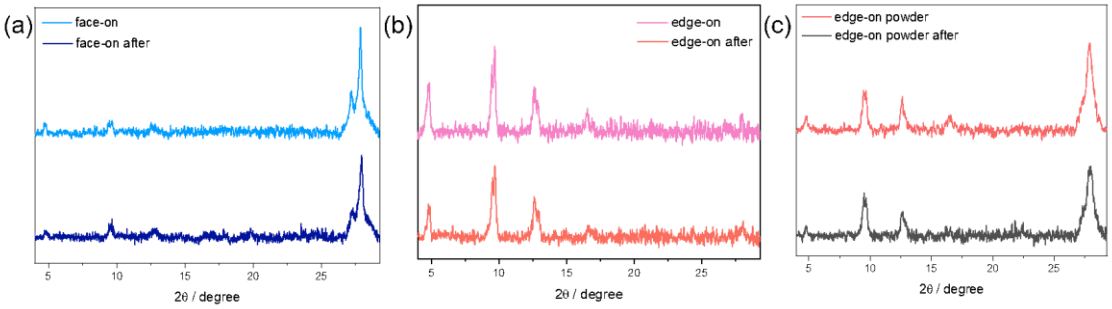

Figure 5. 11: (a) XRD pattern of edge-on film before (top line) and after (bottom line) ammonia exposure for 30 min. (b) XRD pattern of face-on film before (top line) and after (bottom line) ammonia exposure for 30 min. (c) XRD analysis of powder scraped from the edge-on film, showing the peak near 28°.

5.4 Conclusion and outlook

In summary, we fabricated face-on and edge-on MOF films directly on interdigitated electrodes using an electrochemical synthesis method. Their performance as active materials in chemiresistive gas sensors were investigated. Notably, the edge-on film can detect ammonia with good reproducibility and a LOD of 20 ppb, while the face-on film shows a much weaker response. Several factors likely contribute to the observed differences in sensing behaviour. First, the anisotropic structure and conductivity of the oriented films may play a role. In edge-on films, the dominant surface structures are the exposed interlayer spaces of $Cu_3(HHTP)_2$ layers, while in face-on films, the exposed surface consists of the void spaces from the pores.[110, 172] The SEM images show that the edge-on film has a thinner structure and greater surface roughness compared to the face-on film.

To investigate the interaction between $Cu_3(HHTP)_2$ films and ammonia, we employed a combination of EPR, XPS, FT-IR, and XRD techniques. However, these methods did not yield conclusive evidence of the interaction. Future research should focus on in situ techniques to capture dynamic changes during gas exposure.

Chapter 6

Solution-processable MOF nanomaterials for chemiresistive gas sensing

The limited processability of metal-organic frameworks (MOFs) has posed challenges for their integration into large-scale device with optimised performance. In this chapter, we develop two methods, the modulator-based synthesis method and surfactant-based synthesis method, to prepare solution-processable conductive MOF nanomaterials via solvothermal synthesis. These methods enable the controlled synthesis of $Cu_3(HHTP)_2$ nanocrystals with varying dimensions, demonstrating excellent dispersibility in solvents including water, methanol, and dimethylformamide (DMF). Comprehensive characterization of their structural and conductive properties confirm the successful synthesis of nanoscale crystals with dimensional control and uniform size dispersion.

To examine their potential in device applications, the solution-processable $Cu_3(HHTP)_2$ nanomaterials were deposited onto interdigitated electrodes (IDEs) using a spray-coating method. The fabricated film demonstrated high sensitivity and quick recovery of resistance, highlighting the potential of these methods for producing conductive MOFs with enhanced processability for sensing applications. This work was carried out in collaboration with my colleague Weishuo Li. Weishuo conducted the initial synthesis of the MOF nanocrystals, while

I performed all subsequent characterizations. The synthesis and testing conditions were collaboratively designed and refined.

6.1 Introduction

Due to their combined conductivity and porosity, conductive MOFs have been applied in diverse fields including energy storage, chemiresistive sensors, electrochromism, and electromagnetic wave absorption.[56, 191-194] Despite these achievements, their limited processability poses challenges for large-scale device fabrication and miniaturization. The conventional solvothermal method typically produces microcrystalline powders of conductive MOFs, which are subsequently dispersed in solvents and applied to substrates as active layers using coating methods such as drop-casting, spray-coating and mechanical abrasion.[195-200] However, this approach often results in micrometre-scale particles, leading to poor grain-to-grain contact and inadequate grain-to-electrode interface contact.[14, 201] These limitations hinder the performance of individual devices and device-to-device reproducibility, while also making nanoscale device preparation particularly challenging.

To address the challenge of material processability, various methods have been developed, such as layer-by-layer self-assembly, vapour-assisted conversion, interfacial self-assembly, in situ surface coating, and electrochemical deposition.[202-208] These techniques have enabled the fabrication of uniform conductive MOF nanofilms with tunable surface morphology. These advancements have shown promise for enhancing device performance, particularly in the field of chemiresistive gas sensing.[202-203, 209] Despite these progresses, these methods introduce several limitations in device fabrication, such as the increased processing complexity and limited material diversity. For instance, in situ MOF growth often requires specialized equipment, restrictive operating procedures, and long processing times. As demonstrated by the electrochemical synthesis method reported in previous chapters, synthesis conditions have to be very carefully tuned. The compatibility of electrolyte systems and substrates with the electrochemical process is crucial for the successful synthesis of MOFs. Furthermore, many of

these methods struggle with consistent reproducibility due to the inherent variability of the processing procedures during the MOF formation.

An alternative and more straightforward fabrication strategy is to achieve solution processable MOFs through either top-down or bottom-up methods.[210] Top-down methods, such as exfoliation and centrifugation, provide straightforward solutions but often yield uncontrollable morphology, poor size uniformity and low reproducibility. Bottom-up methods could achieve structural control by the addition of additives, such as modulators, hard templates, and surfactants, offering a balance between high yields and reliable control of MOF structures.[211-215] Some of these studies have notably led to improved chemiresistive gas sensing performance, as higher surface-to-volume ratios and thinner sensing films benefiting from material design can enhance the interaction between conductive MOFs and gas analytes.[198, 211-214]

Among these bottom-up methods, hard template-based approaches often employ insoluble sacrificial precursors such as metal oxides and MXenes, which can introduce impurities and undesired contributions to material properties.[216] The modulator-based approach offers a promising route to achieve processable MOF nanomaterials with controlled size by varying the amount or type of modulators. These modulators, typically monotopic analogues of MOF ligands, function as end-capping molecules due to their single coordinating group, ensuring high material purity. Another effective method is the surfactant-based approach, which limits the growth of MOF crystals, particularly by alleviating their stacking in the preferred stacking direction.[59] Both methods avoid the potential contributions or influence from templates that might affect material properties. Although both the modulator-based and the surfactant-based methods have shown promise, only limited studies have so far been reported, and the potential of the resulting MOFs in chemiresistive gas sensing has not yet been systematically explored.

In this study, we developed two approaches for the solvothermal synthesis of solution-processable conductive MOFs: a modulator-based method and a surfactant-based method. Initially, catechol was introduced as a modulator due to its structural simplicity and similarity to HHTP (2,3,6,7,10,11-hexahydroxytriphenylene), enabling the synthesis of MOF nanocrystals with controllable sizes, leading to the formation of $Cu_3(HHTP)_2$-Cat. To further achieve morphology control, we employed a surfactant-based method using polyvinylpyrrolidone (PVP), a widely used polymeric surfactant in nanomaterial synthesis. This approach facilitated the formation of $Cu_3(HHTP)_2$-PVP nanorods with tunable dimensions. $Cu_3(HHTP)_2$ was selected for this work as it is a well-studied conductive MOF with significant potential for practical applications. The solvothermally synthesized $Cu_3(HHTP)_2$ nanomaterials using both methods, with varying dimensions, exhibited excellent dispersibility in solvents such as water, methanol, and DMF. Comprehensive structural characterization of these MOFs was performed to confirm the structure and fundamental properties using techniques including X-ray diffraction (XRD), Fourier-transform infrared spectroscopy (FTIR), scanning electron microscopy (SEM), and Brunauer-Emmett-Teller (BET) surface area analysis. The electrical conductivity of pellets made from $Cu_3(HHTP)_2$-Cat and $Cu_3(HHTP)_2$-PVP was measured using the four-probe method to evaluate their electronic properties. Additionally, these solution-processable $Cu_3(HHTP)_2$ nanomaterials were deposited onto glass substrates with Pt interdigitated electrodes (IDEs) via spray coating. Chemiresistive gas sensing experiments were conducted to explore their potential as ammonia sensors, demonstrating the promise of these materials in sensing applications.

6.2 Experimental section

6.2.1 $Cu_3(HHTP)_2$-Cat MOF preparation

A solid mixture of HHTP (32.4 mg, 0.10 mmol, 1 equiv.) and catechol (5.5 mg, 0.05 mmol, 0.5 equiv) was dissolved in 10 mL DMF and 10 mL EtOH in a 75 mL round bottomed pressure vessel with PTFE bushing (Synthware). A solution of $Cu(OAc)_2$ (27.3 mg, 0.15 mmol, 1.5 equiv) in 5 mL DI H_2O was added dropwise to this mixture in the pressure vessel at a rate of 4 $\mu L\ s^{-1}$ controlled by a syringe pump (Ossila). This mixing process was facilitated under stirring at 500 rpm. The resulting solutions in the capped pressure vessel were then heated at 85 ℃ under stirring at 500 rpm for 18 hr, after which they were centrifuged at 13000 rpm for 15 min using a Heraeus multifuge X3 centrifuge equipped with a Fiberlite F15-8 x 50cy fixed-angle rotor. The precipitates were further washed twice through ultrasonic re-dispersion in MeOH for 10 min followed by centrifugation at 13000 rpm for 10 min. Subsequently, the washed precipitates were dried under vacuum at room temperature in a Heraeus vacutherm oven. The obtained MOFs were named $Cu_3(HHTP)_2$-Cat.

6.2.2 $Cu_3(HHTP)_2$-PVP MOF preparation

The synthesis of $Cu_3(HHTP)_2$-PVP followed the same procedure as $Cu_3(HHTP)_2$-Cat, except catechol was replaced with PVP (200.0 mg), and $Cu(OAc)_2$ with $Cu(NO_3)_2{\cdot}3H_2O$ (36.2 mg, 0.15 mmol). Additionally, the solvent ratio was adjusted to 10 mL DMF and 15 mL EtOH to improve PVP solubility. All other conditions, including dropwise addition of the copper precursor, reaction temperature, stirring rate, duration, and post-synthetic washing and drying steps, remained unchanged. The resulting material was designated $Cu_3(HHTP)_2$-PVP.

6.2.3 Characterization

Powder X-ray Diffraction (PXRD) of the MOF powder was performed using a Panalytical Empyrean XRD equipped with a Cu Kα radiation source. The instrument was operated at a tube voltage of 40 kV and a current of 40 mA. Samples for PXRD analysis were prepared by mounting the powder onto a sample holder and flattening it using a glass slide. UV–Vis absorption spectra were collected using a Varian Cary 5000 UV-Visible-NIR Spectrometer. The MOF powder was dispersed in anhydrous DMF to eliminate the influence of water absorption in the NIR region. The scan range was set from 260 to 2000 nm. Fourier-transform infrared (FT-IR) spectroscopy was performed using a Varian Excalibur FTS 3500 FT-IR Spectrometer. For FT-IR analysis, the MOF powder was mixed with KBr and pressed into pellets. Scanning electron microscope (SEM) images were obtained using a Zeiss Merlin (EDX) SEM with an InLens detector. The instrument was operated at an accelerating voltage of 12kV and a beam current of 150pA. For SEM experiments, each MOF sample was dispersed in water and drop-cast on a piece of ITO glass. The nitrogen adsorption measurements were carried out using a Micromeritics Gemini VII BET surface area analyser. Prior to the measurements, the samples were degassed overnight at 85°C under flowing nitrogen. The fits to the Brunauer-Emmett-Teller (BET) equation met the published consistency criteria. Conductivity measurements were performed at room temperature using an Ossila Four-Point Probe. Prior to the measurements, 65 mg of each sample was compressed into a circular pellet with a diameter of 15 mm and a thickness of approximately 360 μm under an applied pressure of approximately 3 GPa. The pellet thickness was measured using a micrometer. Conductivity was measured 100 times for each sample to obtain a mean value, with measurements taken from three different areas of each pellet.

6.2.4 Spray-coating process for gas sensor fabrication

Samples for gas sensing were prepared via spray-coating. The obtained MOFs were re-dispersed in DI H_2O at a concentration of 0.3 mg mL^{-1} through 30-min ultrasonic treatment at 10 ± 1 ℃. A Bartsharp AC01 airbrush kit (UK) was utilised as the spray-coater. The air pressure applied to the airbrush (nozzle diameter: 0.3 mm, cup capacity: 7 cc) was 30 psi and the air flow rate was set to 20 L min^{-1}. For each MOF, a 100 μL suspension was added to the cup of the airbrush. The Pt IDE substrate was placed on an IKA RCT Basic stirrer hotplate (UK, accuracy: ± 5 °C) set at 85 ℃ to speed up the evaporation process and avoid flooding during spraying. The spray-coating was then conducted at a distance of 10.0 ± 0.1 cm between the nozzle and the deposition area covering the Pt IDE substrate. This process was terminated upon complete consumption of the solution loaded in the airbrush cup. For further drying, the obtained samples were left on the RCT hotplate for 30 min.

6.2.5 Sensing experiments

Gas sensing experiments were conducted in a custom-made glass bottle chamber (250 mL). Sensing tests involved using NH_3 (10 ppm, nitrogen fill) and zero grade N_2 (99.998 %, to further dilute the analyte). The flow rate of each gas cylinder was regulated by an Alicat mass flow controller (accuracy: ± 0.5 % of reading), with the gases being mixed at a joint before being introduced into the gas inlet of the chamber. A total flow rate of 500.0 ± 2.5 standard cubic centimetres per minute (sccm) was maintained throughout the experiments. The concentration of analyte gas was determined by the relative flow rates of the two mass flow controllers. The temperature and relative humidity in the chamber were recorded via a Sensirion SHT31 temperature and humidity sensor (accuracy: ± 0.3 ˚C and ± 2 % RH) placed next to the samples. Each sample in the custom-made chamber was connected to a Keysight B2902A source/measure unit (UK). A DC potential of 1.0 V was applied during the experiments, and the resistance of the sample was monitored on a personal computer equipped with Benchvue

software. The sensing layer on each sample was parallel to the direction of airflow at a distance of 10.0 ± 0.5 mm to the head of gas inlet tube. Prior to each test, the chamber was purged with N_2 to remove impurities from the chamber and the sensing layer until a stable baseline was reached. The sample was then exposed to concentrations of NH_3 from 5 parts per million (ppm) to 0.5 ppm for 10 min per exposure. After each exposure, the sample was purged with N_2 for 20 min before the next exposure. The temperature and humidity where each test was conducted were approximately 22 ℃ and 4 % RH.

6.3 Results and discussion

6.3.1 Modulator-assisted synthesized $Cu_3(HHTP)_2$-Cat

The synthesis of $Cu_3(HHTP)_2$ nanocrystals was explored using a modulator to control particle size. Catechol was chosen as the modulator due to its structural similarity to HHTP and its simplicity, enabling effective integration into the synthesis process. A molar ratio of 3:2 between $Cu(OAc)_2$ to HHTP was maintained to ensure stoichiometric balance. $Cu(OAc)_2$ was selected as the copper source due to its weakly acidic nature, which minimizes the risk of inhibiting the deprotonation and oxidation processes during $Cu_3(HHTP)_2$ formation. The weak acidic nature makes $Cu(OAc)_2$ a commonly used precursor in such synthesis.

The formation and properties of $Cu_3(HHTP)_2$-Cat were investigated using a range of analytical techniques. For comparison, pristine $Cu_3(HHTP)_2$ powder was synthesized via solvothermal methods as described in Chapter 4. The crystal structure of $Cu_3(HHTP)_2$-Cat was characterized using XRD. The XRD pattern of $Cu_3(HHTP)_2$-Cat powder showed diffraction peaks at 4.9°, 9.6°, 12.7°, and 28°, which is consistent with the known XRD pattern of solvothermally synthesized $Cu_3(HHTP)_2$ in the absence of catechol (Figure 6.1). This result confirms the

successful formation of $Cu_3(HHTP)_2$-Cat and indicates that the addition of catechol as a modulator does not affect the crystal structure of $Cu_3(HHTP)_2$.

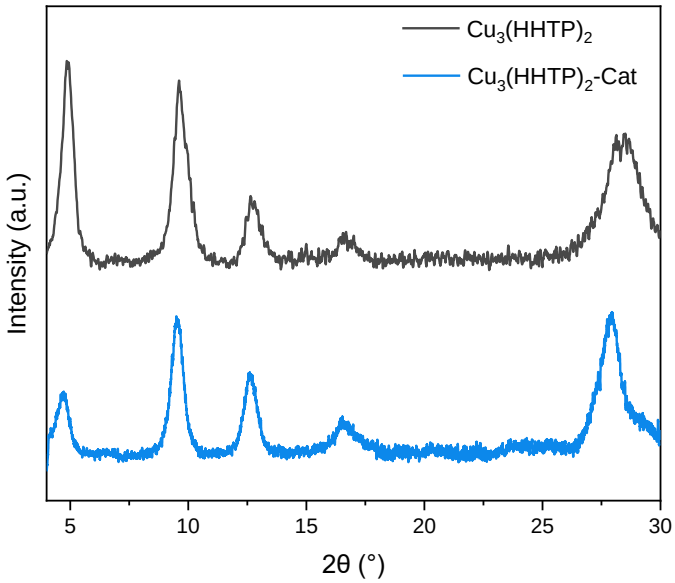

Figure 6. 1: XRD patterns of $Cu_3(HHTP)_2$ (top, grey) and $Cu_3(HHTP)_2$-Cat (bottom, blue), confirming that the addition of catechol does not affect the crystal structure of $Cu_3(HHTP)_2$.

The formation of molecular bonding and the conjugated structure of $Cu_3(HHTP)_2$-Cat were further confirmed through FTIR and UV-vis spectroscopy. As shown in Figure 6.2a, the FTIR spectrum of $Cu_3(HHTP)_2$-Cat exhibited characteristic vibration peaks at 1621 cm^{-1}, 1432 cm^{-1}, and 1292 cm^{-1}, corresponding to the C=O, C=C, and C–O vibrations, respectively.[89, 110] Additionally, the peaks observed at 688 cm^{-1} and 808 cm^{-1} were attributed to the Cu–O stretching and Cu–O scissoring vibrations, providing direct evidence of coordination between copper ions and the organic ligands.[72, 110, 189] UV-vis spectroscopy further shows the material's electronic structure, revealing distinct absorption peaks at 365 nm and 636 nm (Figure 6.2b). These peaks are assigned to the π-π* transition of the HHTP ligand and the ligand-to-metal charge transfer (LMCT) transition, respectively.[67] Notably, the electronic absorption extends

into the near-infrared (NIR) region, indicating the highly conjugated framework of $Cu_3(HHTP)_2$-Cat.[11]

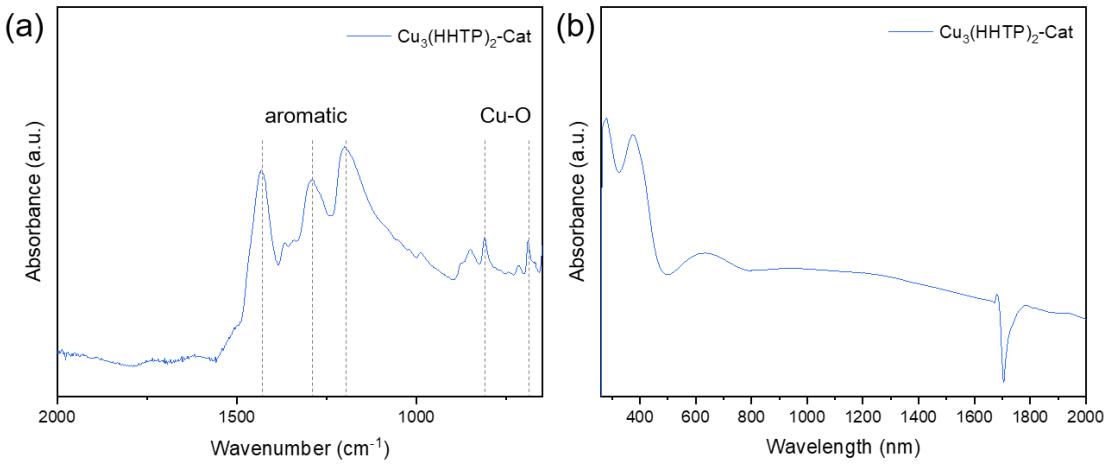

Figure 6. 2: (a) FT-IR spectrum of $Cu_3(HHTP)_2$-Cat confirming coordination between copper and organic ligand. (b) UV-Vis spectrum of $Cu_3(HHTP)_2$-Cat showing a highly conjugated framework, extending to NIR region .

After confirming that the crystal structure, molecular bonding, and electronic properties of $Cu_3(HHTP)_2$-Cat remain unaffected by the addition of catechol, we examined the morphology and particle size distribution of the synthesized $Cu_3(HHTP)_2$-Cat nanomaterials using SEM. As a reference, the morphology of solvolthermally synthesized $Cu_3(HHTP)_2$ without catechol was first examined. The resulting material exhibited large, micron-sized aggregates with uncontrollable size and morphology (Figure 6.3).

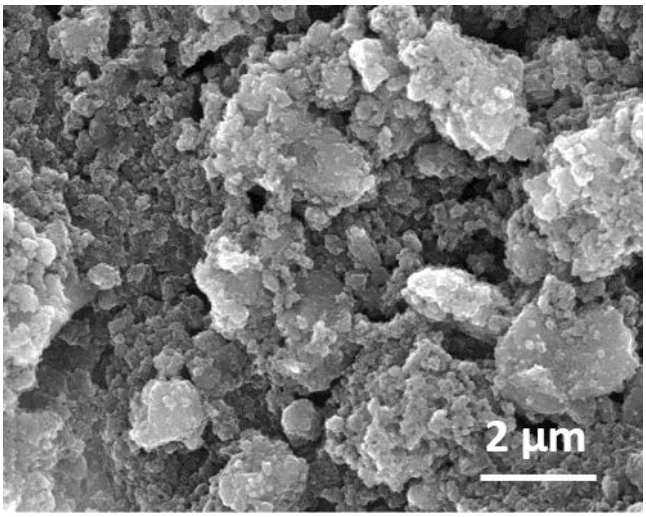

Figure. 6.3: SEM image of pristine solvolthermally synthesized $Cu_3(HHTP)_2$, showing micron-sized aggregates.

The inclusion of catechol as a modulator resulted in the formation of nanoscale aggregates with sizes ranging from 20 nm to 200 nm (Figure 6.4). Due to the inherent aggregation of the nanomaterials, determining the exact particle size was challenging. However, in regions where distinct particles without significant aggregation could be observed, the average particle size was estimated to be between 20 nm and 40 nm. These findings suggest that the addition of catechol effectively restricts particle growth, resulting in the formation of nanoscale MOF materials, further demonstrating the utility of catechol as a modulator for controlling the particle size of $Cu_3(HHTP)_2$-Cat.

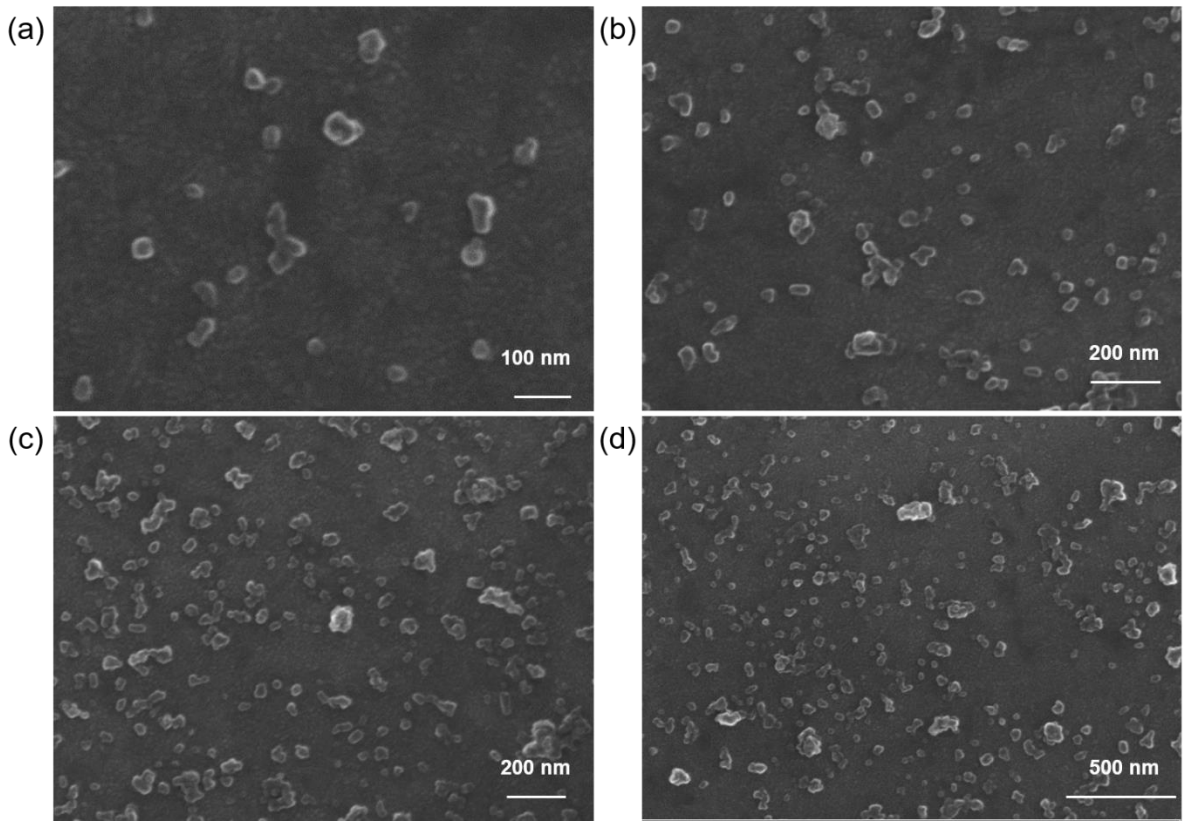

Figure 6. 4: SEM images of $Cu_3(HHTP)_2$-Cat nanomaterials, showing nanoscale aggregates and an average particle size of 20–40 nm, demonstrating the role of catechol in restricting particle growth.

After investigating the structure and properties of the $Cu_3(HHTP)_2$-Cat, we examined the solution processibility of the nanomaterials. As shown in Figure 6.5, the $Cu_3(HHTP)_2$-Cat powder was dispersed in several commonly used solvents including water, methanol, and DMF. The pictures were taken as-synthesized and after standing for 48 hours. The excellent solution dispersibility and stability can be observed from the pictures.

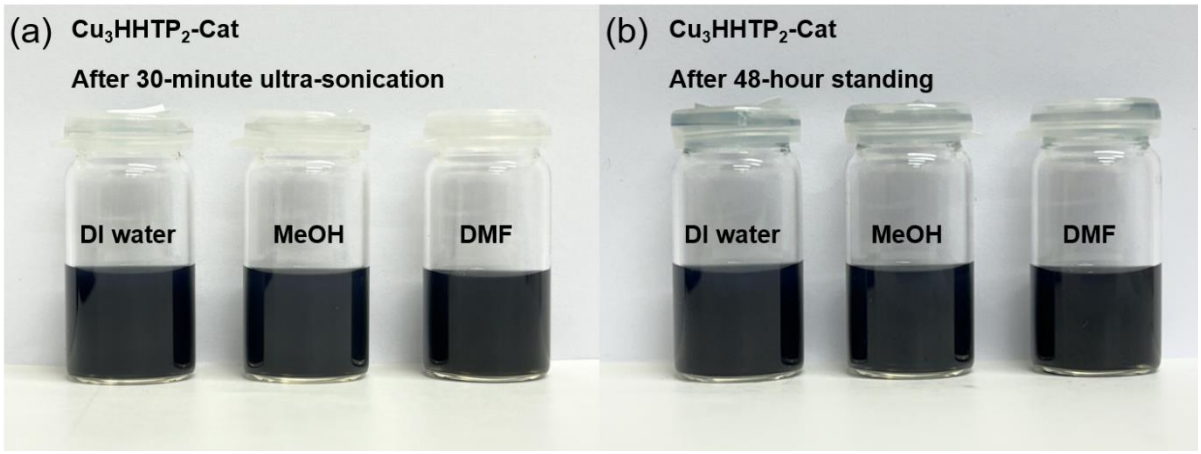

Figure 6.5: Optical photographs of as-synthesized $Cu_3(HHTP)_2$-Cat suspension in DI water, MeOH, and DMF. Panels (a) and (b) display the same suspensions after being left undisturbed at room temperature for 48 hours. The corresponding molecules and solvents are labelled in the images.

Apart from the observed differences in particle size, $Cu_3(HHTP)_2$-Cat and $Cu_3(HHTP)_2$ exhibit nearly identical properties across all other characterization techniques. By analyzing the gas sorption curves, the Brunauer-Emmett-Teller (BET) surface area of $Cu_3(HHTP)_2$-Cat was determined to be 149.4 ± 1.1 m^2g^{-1} (Figure 6.6). The electrical conductivity of a $Cu_3(HHTP)_2$-Cat pellet at room temperature was measured using the four-probe method, yielding a value of 0.21 S/m, aligning well with previously reported values for $Cu_3(HHTP)_2$.

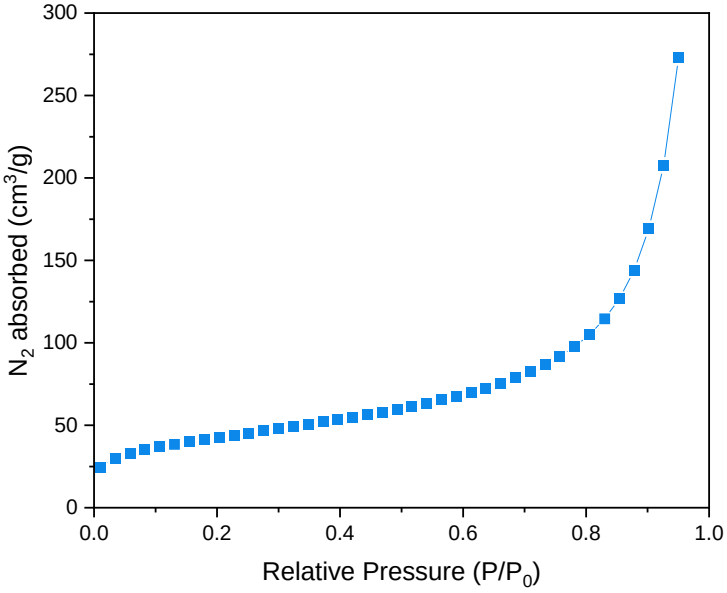

Figure 6.6: N_2 adsorption isotherm of $Cu_3(HHTP)_2$-Cat. The BET surface area of 149.4 ± 1.1 m^2g^{-1} was calculated by fitting the adsorption curve.

6.3.2 Fabrication and performance of $Cu_3(HHTP)_2$- gas sensor

The well-dispersed suspension allows for the fabrication of gas sensors using common methods such as drop-casting, spray-coating, immersion, and evaporation. Initially, we experimented with the immersion method to form a $Cu_3(HHTP)_2$-Cat film on an interdigitated electrode (IDE). However, due to the low concentration of the nanocrystal suspension, we observed only a small droplet on the IDE after immersion, and no measurable conductance was detected once the film dried. We then attempted to deposit the suspension by evaporating it on the IDE in an oven at 30-50°C, but this approach resulted in particle aggregation rather than a well-dispersed film. The spray coating method, however, was shown to be suitable for MOF film deposition on the IDEs.

We examined the sensing performance of the spray-coated $Cu_3(HHTP)_2$-Cat sensor. The fabricated sensor was placed in the sensor testing chamber, as described in the methodology, under a nitrogen flow with 1V applied. The resistance of the $Cu_3(HHTP)_2$-Cat film on the IDE were consistently monitored. As shown in Figure 6.7a, the dynamic response-recovery curves were recorded for ammonia concentrations ranging from 5ppm to 0.5ppm. Upon exposure to ammonia, the resistance of the $Cu_3(HHTP)_2$-Cat increases. The sensor demonstrated excellent reversibility over four exposure-recovery cycles highlighting its stability and reproducibility (Figure 6.7b). A baseline shift was observed, likely caused by environmental factors, especially temperature changes due to the long measurement duration.

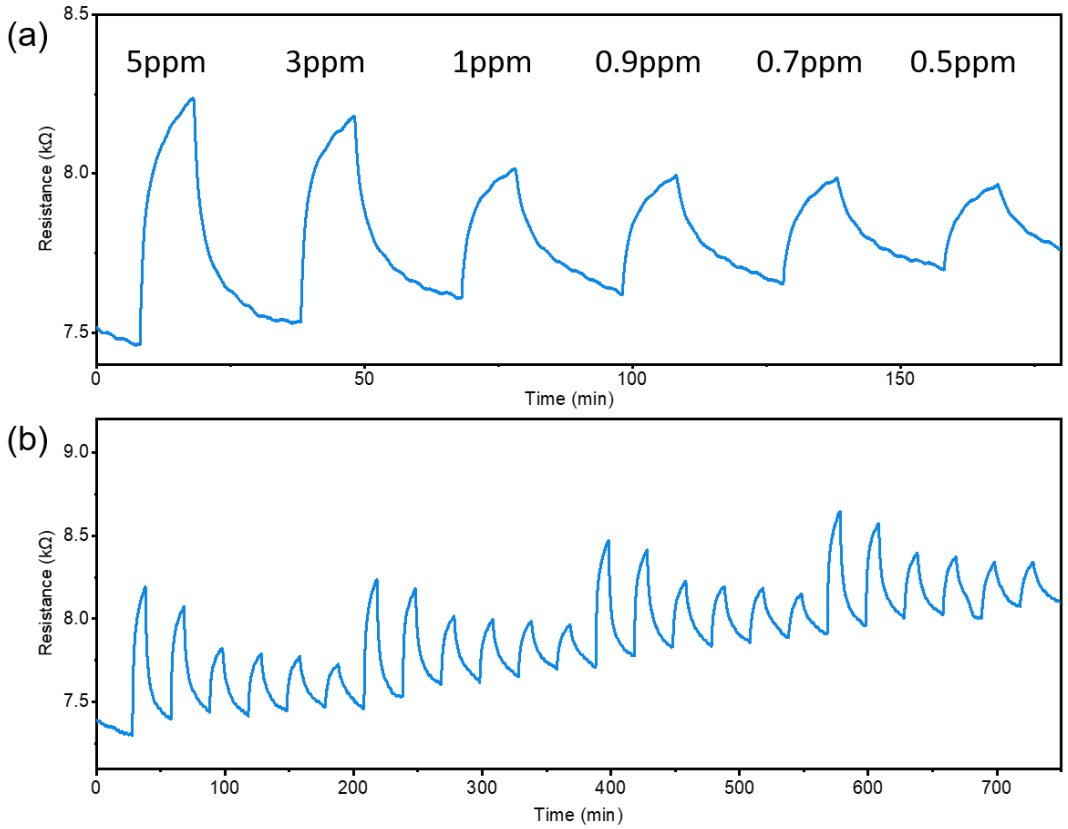

Figure 6. 3: (a) Response–recovery curves of $Cu_3(HHTP)_2$-Cat upon exposure to NH_3 for 10 minutes followed by 20 minutes of recovery, measured at concentrations of 5, 3, 1, 0.9, 0.7, and 0.5 ppm. (b) Sensor response over four repeated exposure–recovery cycles under the same conditions and concentration range as in (a).

Figure 6.8 presents the response of $Cu_3(HHTP)_2$-Cat as a function of ammonia concentration. For an ammonia concentration of 5 ppm, the resistance change reaches approximately 10.5%. A non-linear response trend is observed towards higher concentration as indicated. The sensor exhibits a sensitivity of approximately 5.9±2.8% ppm^{-1} and a calculated LOD of 300 ppb based on the 1ppm data, surpassing the performance of powder $Cu_3(HHTP)_2$-based sensors reported in the literature.[70, 101]

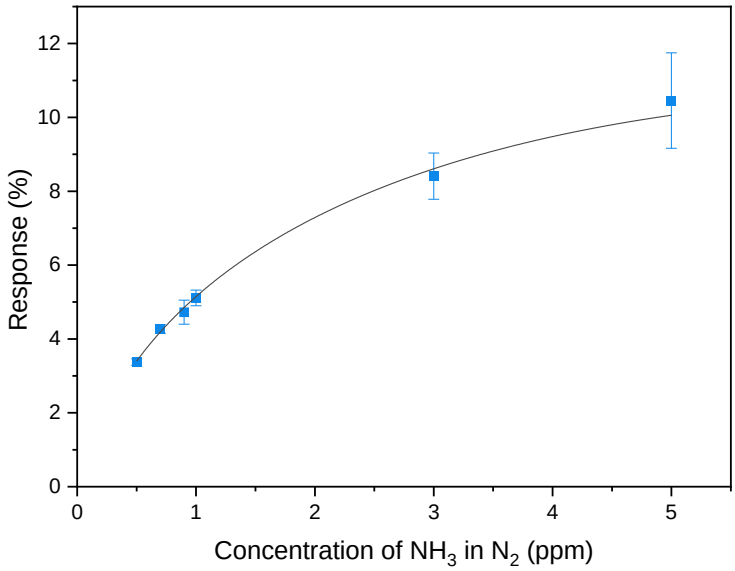

Figure 6. 4: Gas sensor calibration curve for NH_3 in dry N_2 of $Cu_3(HHTP)_2$-Cat. The sensitivity is 5.9±2.8% ppm^{-1} for the concentration range around 1 ppm.

6.3.3 Surfactant-assisted morphology Control of $Cu_3(HHTP)_2$-PVP

Besides the advantages mentioned above, we found that the addition of catechol enables control over the particle size of nano-MOF crystals but does not significantly influence their morphology. To achieve control over the morphology of these nanocrystals, we focused on an alternative approach. Instead of searching for suitable chemicals as modulators or templates, we explored the use of common surfactants to limit MOF crystal growth, particularly along the

stacking direction.[59] To direct the growth of the 2D MOF nanomaterials in a preferred orientation, we used PVP as a morphology-modulating agent to alleviate stacking.[59, 68] Initially, PVP was added to a reaction mixture of $Cu(OAc)_2$ and HHTP, as used in the previous discussed catechol-based synthesis. However, the rapid reaction between $Cu(OAc)_2$ and HHTP prevented effective regulation of MOF nanocrystals by PVP. To overcome this, we replaced $Cu(OAc)_2$ with $Cu(NO_3)_2$ to slow the reaction kinetics with HHTP, allowing the PVP to participate in the reaction. A molar ratio of $Cu(NO_3)_2$ to HHTP was maintained at 3:2, and 200 mg of PVP was introduced to direct the growth direction of $Cu_3(HHTP)_2$-PVP. The crystal structure of the resulting $Cu_3(HHTP)_2$-PVP was examined using XRD. As shown in Figure 6.9, the XRD spectra reveal that the pattern of $Cu_3(HHTP)_2$-PVP (red, bottom) aligns with the characteristic pattern of $Cu_3(HHTP)_2$ pattern (black, top), confirming the successful formation of the MOF structure. Notably, compared to $Cu_3(HHTP)_2$, the PXRD pattern of $Cu_3(HHTP)_2$-PVP displays a significantly sharper reflection at 27.9°, corresponding to an interlayer distance of 0.32 nm. The reduced peak broadening suggests a more ordered stacking structure, indicating that the incorporation of PVP facilitates the formation of a structurally better-aligned $Cu_3(HHTP)_2$ framework.

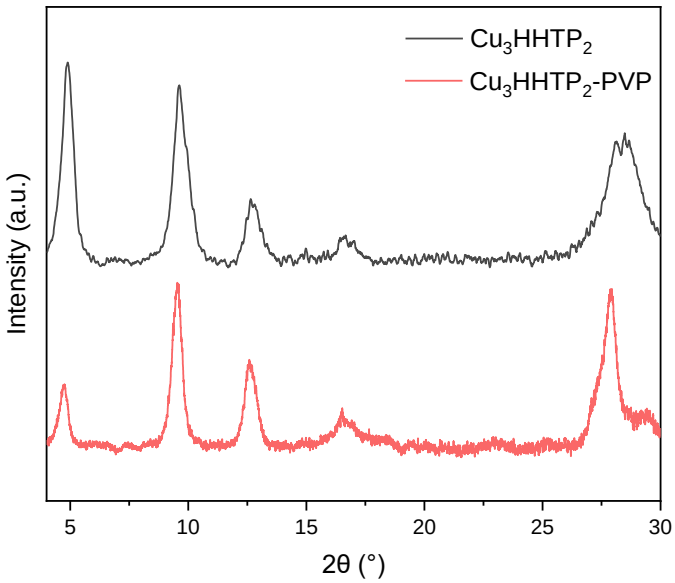

Figure 6. 5: XRD patterns of $Cu_3(HHTP)_2$ and $Cu_3(HHTP)_2$-PVP, confirming the successful formation of $Cu_3(HHTP)_2$ with the addition of PVP molecules. The PVP does not significantly alter the crystal structure of the $Cu_3(HHTP)_2$ MOF.

The FTIR spectrum of $Cu_3(HHTP)_2$-PVP reveals characteristic peaks, including those associated with aromatic peaks and Cu-O bonds, consistent with the $Cu_3(HHTP)_2$ (Figure 6.10a). However, the peak at 1654 cm^{-1}, corresponding to the C=O stretching vibration, is notably stronger in $Cu_3(HHTP)_2$-PVP compared to $Cu_3(HHTP)_2$.[217] This increased intensity may indicate interactions between the C=O groups of PVP and metal ions, leading to the incorporation of PVP molecules onto the MOF planes.[218] Alternatively, the increased intensity of the C=O peak could result from differences in $Cu_3(HHTP)_2$, such as defects, or changes in the oxidation state of the ligand. Despite these changes in the FTIR spectrum, the UV-Vis spectrum remains unchanged, indicating that the addition of PVP does not alter the electronic structure of $Cu_3(HHTP)_2$ (Figure 6.10b).

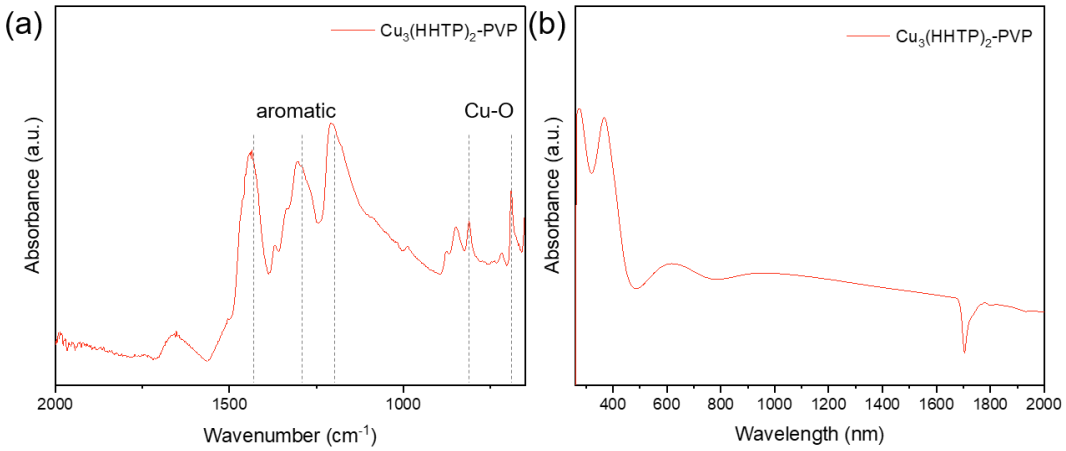

Figure 6. 6: (a) FTIR spectrum of $Cu_3(HHTP)_2$-PVP showing an increased intensity of the C=O bond. (b) UV-Vis spectrum showing unchanged electronic structure.

As shown in Figure 6.11, SEM images show the nanorod structure of $Cu_3(HHTP)_2$-PVP. The images were captured from randomly selected areas of a single sample to ensure representative analysis. Similar to the $Cu_3(HHTP)_2$-Cat, the nanorods tend to aggregate. However, in regions where the nanorods are well-dispersed, their dimensions can be measured. Specifically, the nanorods exhibit lengths ranging from 200 to 500 nm, and widths of approximately 15 to 30 nm. These results demonstrate that the morphology of $Cu_3(HHTP)_2$ can be tuned by the addition of PVP. Further studies could focus on optimizing the synthesis conditions to achieve more precise size control and to explore the impact of these morphological variations on the material's properties and potential applications.

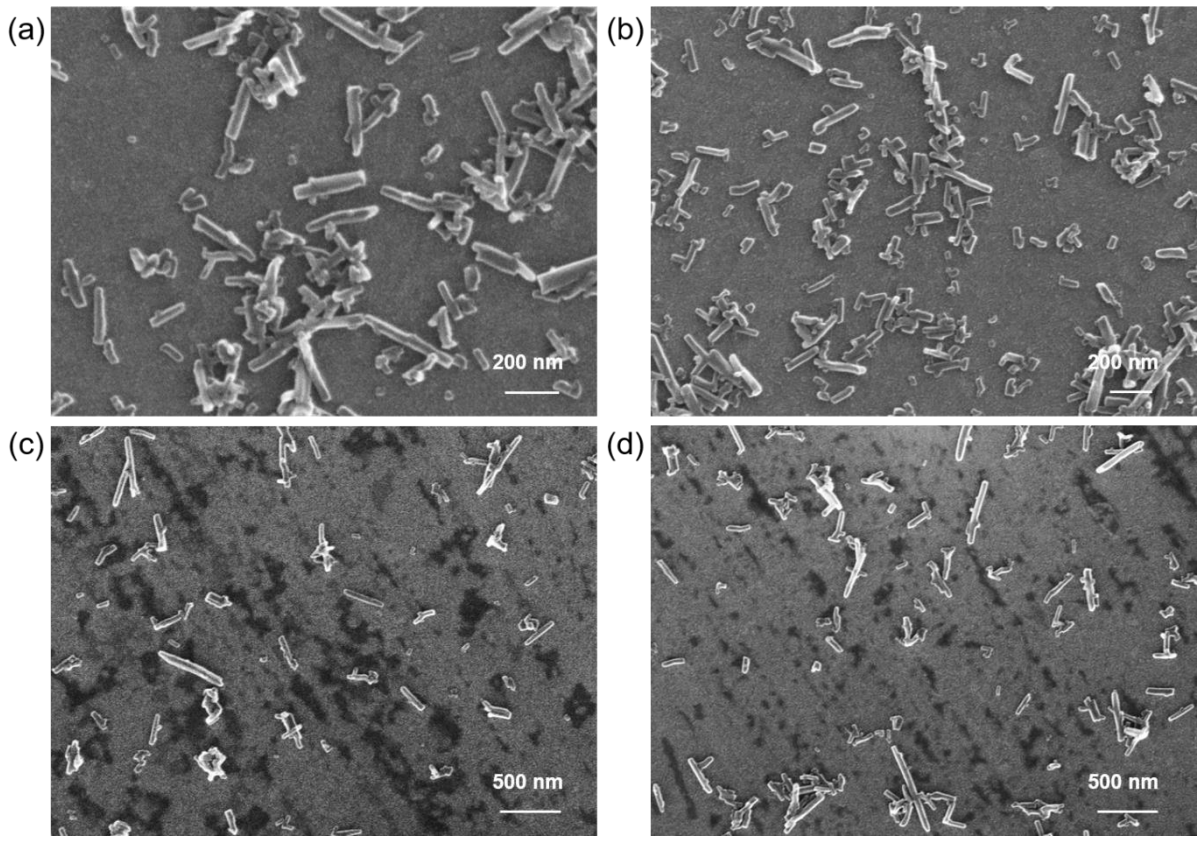

Figure 6. 7: SEM images of $Cu_3(HHTP)_2$-PVP nanorods, showing nanorod structures and demonstrating the role of PVP in controlling MOF size and directing morphology.

After verifying the crystal structure, confirming the formation of nanoscale particles, and characterizing the properties of $Cu_3(HHTP)_2$-PVP, we investigated its solution processability. The $Cu_3(HHTP)_2$-PVP powder was dispersed in the same solvents used for $Cu_3(HHTP)_2$-Cat: water, methanol, and DMF. To evaluate stability and dispersibility, photographs were captured immediately after dispersion and again after 48 hours of undisturbed standing at room

temperature. As shown in Figure 6.12, the results demonstrated that the suspension maintained excellent dispersibility and stability across all tested solvents throughout the observation period.

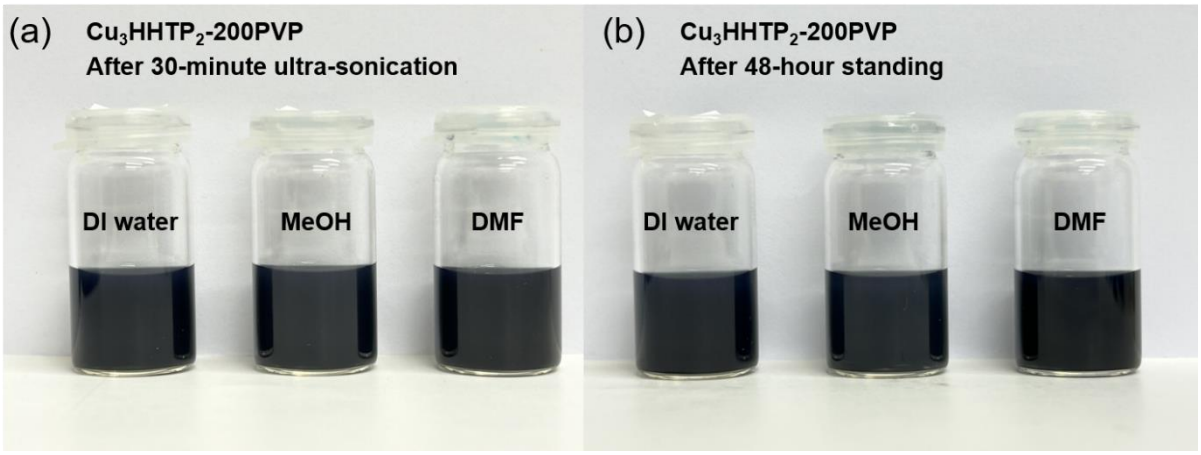

Figure 6. 8: Optical photographs of as-synthesized $Cu_3(HHTP)_2$-PVP suspensions in DI water, MeOH, and DMF. Panels (a) and (b) display the same suspensions after being left undisturbed at room temperature for 48 hours. The corresponding molecules and solvents are labelled in the images.

Next, we examined the BET surface area of $Cu_3(HHTP)_2$-PVP, the N_2 absorption curve revealed a surface area of 73.5±0.5 m^2g^{-1} (Figure 6.13). This value is lower than that of $Cu_3(HHTP)_2$-Cat, likely due to the larger particle size of $Cu_3(HHTP)_2$-PVP, which may result in a reduced specific surface area. The electrical conductivity of a $Cu_3(HHTP)_2$-PVP pellet at room temperature was measured using the four-probe method, yielding a value of 0.023±error S/m, which is an order of magnitude lower than for $Cu_3(HHTP)_2$-Cat.

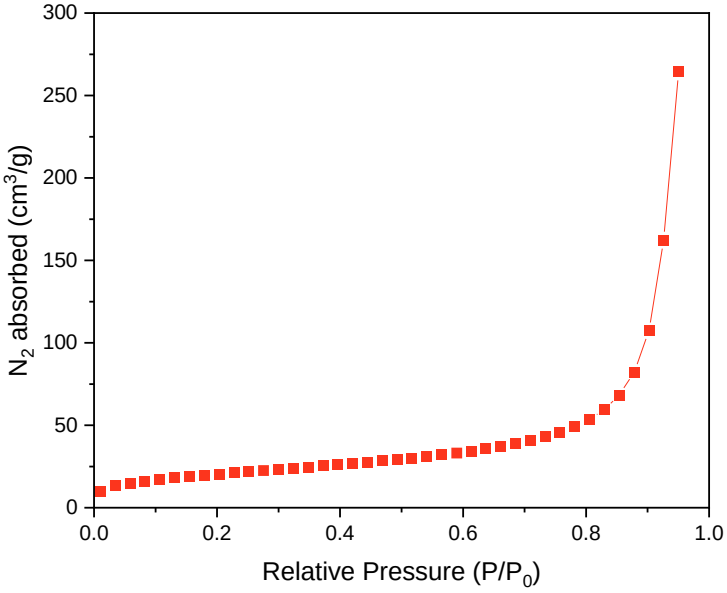

Figure 6. 9: N_2 adsorption isotherms of $Cu_3(HHTP)_2$- PVP. The BET surface area of 73.5±0.5 m^2g^{-1} was calculated by fitting the adsorption curve.

6.3.4 Fabrication and performance of $Cu_3(HHTP)_2$-PVP sensor

The $Cu_3(HHTP)_2$-PVP was dispersed in water and spray-coated onto IDEs as described in the method section. The fabricated $Cu_3(HHTP)_2$-PVP sensor was placed in a sensing chamber and exposed to nitrogen gas. The same sensing test was carried out for $Cu_3(HHTP)_2$-PVP as $Cu_3(HHTP)_2$-Cat. Figure 6.14a shows the dynamic response-recovery curve of the $Cu_3(HHTP)_2$-PVP upon exposure to 5 ppm-0.5 ppm ammonia. Upon ammonia exposure, the $Cu_3(HHTP)_2$-PVP shows a reversible increase in resistance. Figure 6.14b shows the sensor performance over four repeated exposure–recovery cycles, highlighting the good repeatability and operational stability of the $Cu_3(HHTP)_2$-PVP sensor.

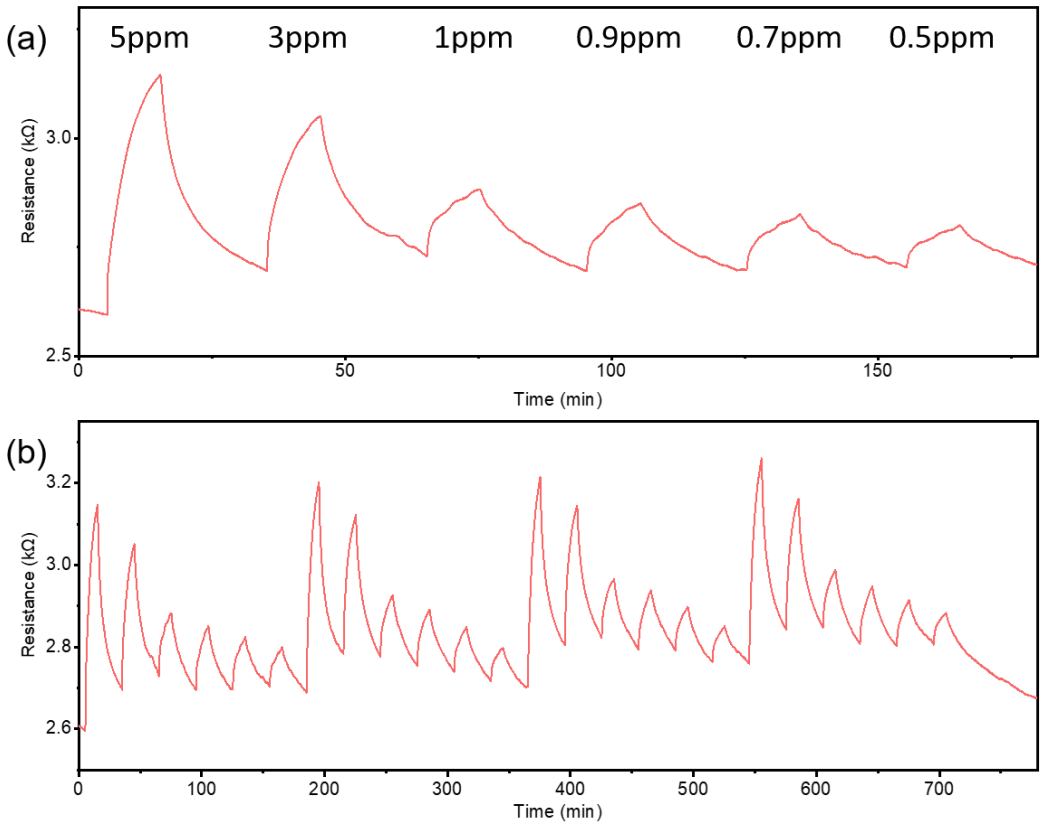

Figure 6. 10: (a) Response–recovery curves of $Cu_3(HHTP)_2$-PVP upon exposure to NH_3 for 10 minutes followed by 20 minutes of recovery, measured at concentrations of 5, 3, 1, 0.9, 0.7, and 0.5 ppm. (b) Sensor response over four repeated exposure–recovery cycles under the same conditions and concentration range as in (a).

Figure 6.15 shows the response of $Cu_3(HHTP)_2$-PVP sensor as a function of ammonia concentration. At an ammonia concentration of 5 ppm, the $Cu_3(HHTP)_2$-PVP exhibits a resistance change of approximately 19.4±1.3% , with a sensitivity of 5.3±0.3% ppm^{-1}. The LOD value is determined as three times the standard deviation of the baseline noise divided by the sensitivity, resulting in an LOD of around 130 ppb.

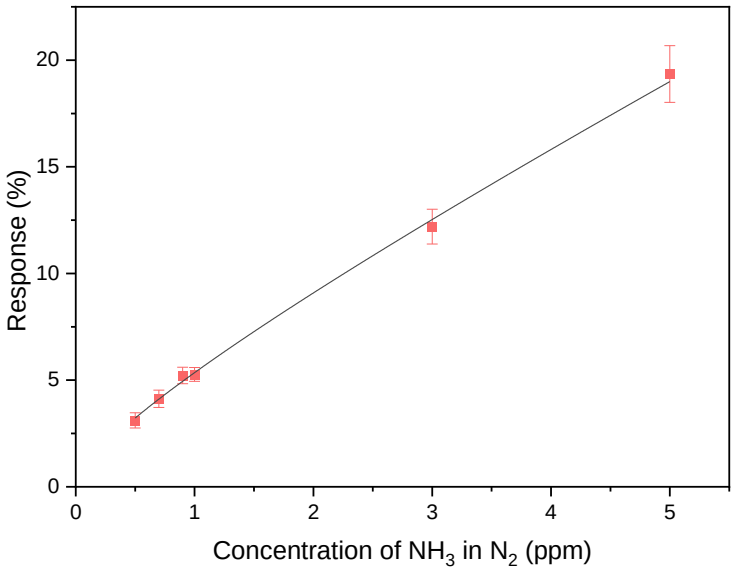

Figure 6. 11: Sensor responses of $Cu_3(HHTP)_2$-PVP as a function of ammonia concentration.

6.3.5 Comparative discussion of $Cu_3(HHTP)_2$-Cat and $Cu_3(HHTP)_2$-PVP

In this study, MOF nanomaterials based on $Cu_3(HHTP)_2$ were successfully synthesized and tailored through the use of modulators and surfactants, demonstrating effective control over particle size and morphology. Structural characterization using XRD, FTIR and UV-Vis spectroscopy confirmed the consistent structure of both $Cu_3(HHTP)_2$-Cat and $Cu_3(HHTP)_2$-PVP. The addition of catechol as a modulator resulted in spherical aggregates with a particle size of 20-40 nm, as observed in SEM images of $Cu_3(HHTP)_2$-Cat. By replacing catechol with PVP, the morphology of $Cu_3(HHTP)_2$ nanomaterials was tuned from spherical aggregates to well-defined nanorods. The introduction of PVP as a surfactant restricted crystal growth along the stacking direction, facilitating the formation of nanorod structures with lengths of 200-500 nm and widths of approximately 15-30 nm.

Both $Cu_3(HHTP)_2$-Cat and $Cu_3(HHTP)_2$-PVP demonstrated excellent solution processability, maintaining stable dispersions in solvents including water, methanol, and DMF over a 48-hour period. This stability highlights their potential for practical applications. Further characterization revealed differences in specific surface area and electrical conductivity between the two materials. BET surface area analysis indicated that $Cu_3(HHTP)_2$-PVP had a lower surface area than $Cu_3(HHTP)_2$-Cat, likely due to its larger particle size. Electrical conductivity measurements also showed significant differences, with $Cu_3(HHTP)_2$-Cat exhibiting a conductivity of 0.21 S/m, while $Cu_3(HHTP)_2$-PVP exhibited a lower conductivity of 0.023 S/m. The decreased conductivity of $Cu_3(HHTP)_2$-PVP can be attributed to the presence of non-conductive PVP within the material and between the nanocrystals. This will interfere with the conductive pathways by residing between the MOF layers or coating the particles.

Both $Cu_3(HHTP)_2$-Cat and $Cu_3(HHTP)_2$-PVP nanomaterials were fabricated into chemiresistive gas sensor using the spray-coating method. Upon exposure to ammonia concentrations between 0.5 and 1 ppm, both sensors exhibit comparable responses. However, at concentrations above 3 ppm, the response of $Cu_3(HHTP)_2$-Cat begins to flatten off, whereas $Cu_3(HHTP)_2$-PVP maintains a more linear and proportional response.

These initial findings confirm that both $Cu_3(HHTP)_2$-Cat and $Cu_3(HHTP)_2$-PVP show good sensing performance for ammonia detection. The observed variations in sensing performance may arise from many factors, including the amount of additives, the uniformity and thickness of the sensor film, and the particle connectivity. Further investigations into these parameters could optimize the sensing performance and provide a systematic insight into the differences between the two sensors.

6.4 Conclusion and outlook

In summary, this study successfully synthesized and tailored $Cu_3(HHTP)_2$-based MOF nanomaterials using catechol and PVP to control particle size and morphology. $Cu_3(HHTP)_2$-Cat formed spherical aggregates, while $Cu_3(HHTP)_2$-PVP formed nanorods. Both materials demonstrated excellent solution stability and good sensing performance, showing their potential as active material for chemiresistive gas sensing. These findings illustrate the versatility and effectiveness of modulator- and surfactant-assisted strategies in designing MOF nanomaterials with tailored morphologies and properties. Future research could focus on optimizing synthesis parameters and sensor integration techniques to achieve more precise control over particle size, morphology, and film thickness. This would enable a systematic investigation of the sensing performance of the MOF nanomaterials. This work not only provides insights into the mechanisms of morphology control but also opens new opportunities for the application of 2D MOF-based nanomaterials in fields such as catalysis, energy storage, and sensing.

Chapter 7

EPR Studies of a Cu-DBC MOF

In previous chapters, the orientation tuning of 2D metal-organic framework (MOF) films via electrochemical synthesis and their application in gas sensing were explored. This chapter shifts the focus to oxidation state modulation in MOFs, specifically using electrochemical synthesis to tune their redox-active properties. We synthesized a catechol-based 3D conductive MOF, Cu-DBC, using both solvothermal and electrochemical approaches. The electrochemical synthesis method resulted in different oxidation states of the ligand, which lead to the generation of organic radicals. This enabled a detailed investigation of the spin dynamics in electrochemically synthesized Cu-DBC using pulse electron paramagnetic resonance (EPR) techniques. The phase memory time (T_m) and spin-lattice relaxation time (T_1) were measured, yielding a phase memory time of 405 ns and spin relaxation time of 24.5 μs at room temperature. These results exhibit the critical role of redox-activity modulation in tuning the spin states of MOFs, offering a potential synthetic approach to build mixed-valence MOFs and explore their potential spin-related applications.

7.1 Introduction

Molecular systems with unpaired electrons have unique electronic and spintronic properties, making them promising candidates for use in organic electronic quantum devices.[121, 219] Achieving long phase memory times (T_m) and spin−lattice relaxation times (T_1) at room temperature are necessary for optimal performance in quantum systems.[220-221] The challenge lies in the random distribution of spin centres within diamagnetic matrices, making spatial control of spin centres very difficult.[121, 129-130] Constructing predictable and periodic arrays of molecular spins is therefore a promising pathway to achieve spatial control of molecular spin systems.[129-131]

The chemical precision and periodicity of MOFs enables organization of radicals into extensive ordered arrays.[5, 43] Previous reported MOFs incorporating unpaired electrons rely on metal centres, such as Co^{2+}, Cu^{2+} and VO^{4+} as paramagnetic spin centres.[129, 132-133] Room temperature coherence in these systems can be achieved by diluting the spin centres within a diamagnetic matrix.[133, 136] However, most of these MOFs fail to achieve comparable phase-memory times at room temperature due to the unpaired d-electrons and strong spin-orbit coupling inherent to these metal-based centres.[20, 131] Furthermore, complicated synthesis methods are involved to embed spin centre in MOFs.[129-130, 133]

An alternative approach is to build MOFs with organic radicals. One of the most well-established redox active linkers is the catechol-based ligand.[43, 148, 222] These ligands can adopt multiple oxidation states, with the fully reduced catechol (Cat) and radical-containing semiquinone ($SQ^{\cdot-}$) states being the most common modes of coordination with Cu to form $Cu^{2+}(Cat^{2-})$ and $Cu^{+}(SQ^{\cdot-})$ complexes.[32] Although the fully oxidized quinone (Q) state is a weak donor and can be subject to defects, especially in 2D MOFs, stabilization of Cu^{+}(Q)-based complexes and MOFs has been demonstrated through $\pi - \pi$ interactions.[31, 33-35] The preferred

coordination form between Cu and catechol, along with its valence tautomeric transitions, depends on various parameters including ligand structure, temperature, and the presence of an oxidant.[32, 34, 36-37] During these processes, Cu itself can oxidize catechol-based-ligands or reduce quinone-based-ligand under oxygen free atmosphere.[38-39] Additionally, Cu^{+} can undergo further oxidation in the presence of oxygen.[34] Several catechol-based ligands in construction of conductive MOFs have been proposed to possess stable radicals at certain oxidation states, such as tetrahydroxy-1,4-benzoquinone (THQ) and hexahydroxytriphenylene (HHTP).[20, 119] These organic ligands exhibit inherent redox activity, leading to distinct oxidation states spin densities based on their coordination with metals.[137, 222]

The dibenzo-[g,p] chrysene-2,3,6,7,10,11,14,15-octaol (DBC) ligand possesses four catechol units, which enable reversible redox transformations within the catecholate-semiquinone-quinone (cat-sq-q) sequence (Figure 7.1a).[12, 48] In previous studies, the resulting Cu-DBC forms a three-dimensional framework in which each copper ion coordinates with four oxygen atoms from two 8OH-DBC ligands, forming $Cu\text{-}O_4$ coordination sites.[152] Submicrometer-sized single crystals of Cu-DBC were analyzed using three-dimensional electron diffraction tomography (3D-EDT), which revealed that the coordination between copper ions and 8OH-DBC ligands results in a three-dimensional framework featuring approximately 1.0 nm in pore size (Figure 7.1b). Detailed structural analysis further confirmed that Cu-DBC adopts a fourfold interpenetrated diamond (dia) topology (Figure 7.1c). The formal charge state of DBC is -4, while Cu exhibits a formal charge of +2, with co-existing Cu^{+} ions. Strong paramagnetic behaviour was observed, arising from the +2 oxidation state of Cu.[29, 152, 223] In this chapter, we explore the possibility to modulate the oxidation states of both the ligand and metal node in the catechol-based MOF. Three-dimensional catechol-based MOFs, Cu-DBC, were synthesized using both a solvothermal method and an electrochemical method. XPS and CW-EPR results

show that the change in oxidation states of Cu and ligands occur only the electrochemical synthesis method. The electrochemically synthesized organic radical-dominating Cu-DBC enables spin dynamics measurements and exhibits room temperature coherence of 405 ns without dilution.

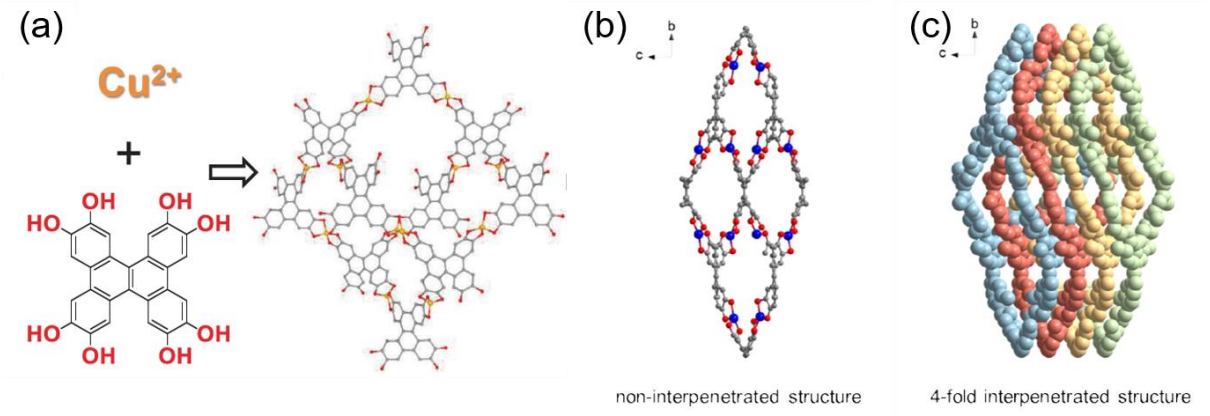

Figure 7. 1: (a) The Cu-DBC structure formed by Cu ions and 8OH-DBC, where each Cu ion is coordinated with two DBC molecules. (b) A non-interpenetrated Cu-DBC framework. (c) A four-fold interpenetrated Cu-DBC framework.

7.2 Experimental section

7.2.1 Solvothermal synthesis of Cu-DBC

The solvothermal synthesis of Cu-DBC was reported by the Chen group.[29] 8.6 mg of DBC ligand and 6 mg of $Cu(OAc)_2 \cdot H_2O$ were dispersed in 500 μL dimethyformamide (DMF) and 2 mL deionized water by ultrasonic treatment for 30 min. This vial was heated on a heating plate at 85 °C for 72 h. The resulting powder was washed with water, ethanol, and acetone three times and dried in air overnight to obtain a black product.

7.2.2 Electrochemical synthesis of Cu-DBC

A conventional 3-electrode set-up was utilized, with a platinum counter electrode and an Ag/AgCl reference electrode, and the electrolytic cell itself was a beaker with a 10 cm diameter. 20 mg of the DBC ligand powder and 300 mg tributylmethylammonium methyl sulfate (TBMAMS) were dispersed in a mixed solution of 50 ml water and 2 ml DMF. A piece of Cu tape was used as the working electrode. The solution was then sonicated for 30 min. The applied potential was 0.45 V applied for 240 min. The resulting powder was washed three times each with acetone, water, and ethanol.

7.2.3 General characterization

Powder X-ray diffraction measurements were performed on a Rigaku Miniflex XRD with a 1.54 Å CuKα X-ray source at room temperature. All EPR measurements were taken in the Centre for Advanced Electron Spin Resonance (CAESR), Department of Chemistry, University of Oxford. The specific machines used to acquire EPR data are Bruker EleXSys-E580 and E680 EPR spectrometers, operating at X-band (~9.7 GHz). For all samples, powder solid samples were placed into sample tubes (OD = 3.8 mm).

7.3 Results and discussion

7.3.1 Synthesis and Characterization

To explore the electrochemical behavior of DBC, CV was initially performed. However, the current changes were undetectable during scanning, likely due to the inherent limitations of CV in capturing weak redox signals or resolving rapid redox processes. This limitation arises because CV measures the total current during a continuous potential sweep, where weak signals could be overshadowed by high background currents or overlapping processes.[224-225] To

overcome this, Differential Pulse Voltammetry (DPV) was employed. DPV applies small voltage pulses over a linearly increasing potential and measures current differences before and after each pulse. This approach minimizes background noise, isolates faradaic currents, and offers higher sensitivity, making it more effective for detecting subtle redox events, slow electron transfer kinetics, or overlapping electrochemical signals.[224-227]

Using DPV, the oxidation potentials of Cu and DBC were determined (Figure 7.2a). Oxidation for DBC began at approximately 0.25V, with the first oxidation peak appearing at about 0.42V. This peak was attributed to a single-electron transfer from cat_4 state to cat_3-sq state, in alignment with previous studies.[29] After deprotonation, the radicals in DBC^{4-} can pair up, resulting in a non-radical structure.[40] The oxidation from DBC^{4-} to DBC^{3-} generates a monoradical structure (Figure 7.2b).[29] In addition, the oxidation of Cu also happens at 0.42V.

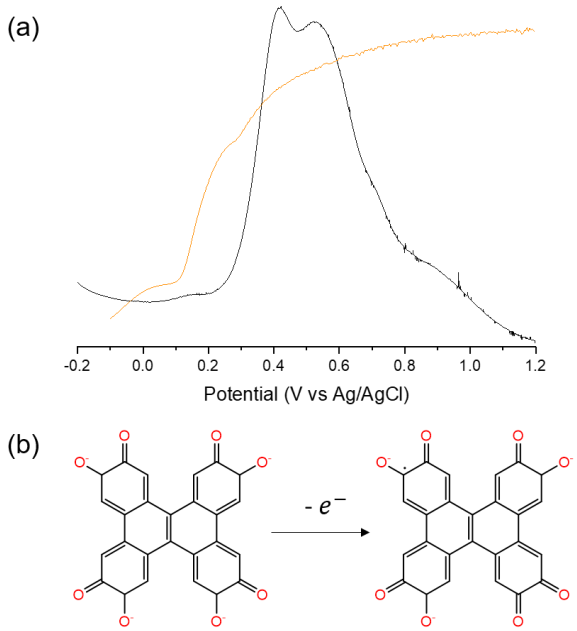

Figure 7. 2: (a) Differential pulse voltammetry (DPV) spectra of DBC (grey line) using an ITO glass working electrode in an electrolyte solution containing DBC, and Cu (yellow line) using a Cu tape working electrode in an electrolyte solution without DBC. The electrolyte solution concentration is 0.2 mM TBMAMS. (b) Redox sequence of DBC from SQ-SQ-SQ-SQ to SQ-SQ-SQ-Q state.

Based on the DPV results, the applied voltage enables the oxidation of ligand on the electrode, suggesting the potential for tuning the oxidation state via an electrochemical synthesis method. To further explore this possibility, we used a conventional three-electrode setup as shown in Figure 7.3, which presents a schematic diagram for the electrochemical synthesis of Cu-DBC. In this process, DBC powder and TBMAMS, used as the electrolyte, were dissolved in a mixture of deionized water and DMF, and a piece of copper tape was immersed in the solution. Upon applying a voltage to the copper tape, the Cu undergoes oxidation. To simultaneously oxidize both Cu and DBC, a voltage of 0.42 V was applied, facilitating the formation of Cu-DBC MOF crystals on the copper tape as well as in the solution. The resulting MOF crystals were collected and filtered using acetone, ethanol, and water, with each solvent applied three times.

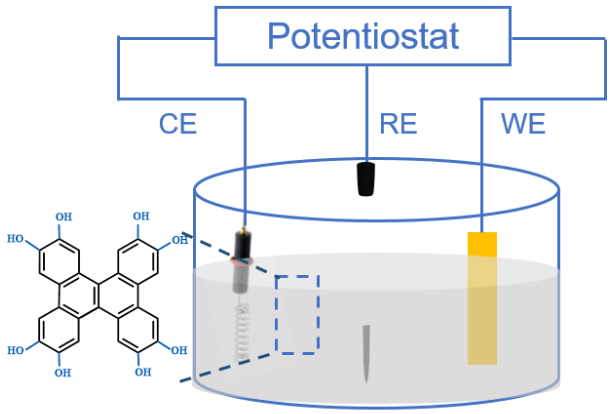

Figure 7. 3: Schematic illustration of the electrochemical synthesis set up for Cu-DBC, with a Cu tape as the working electrode, a Pt electrode as the counter electrode, and Ag/AgCl as the reference electrode.

Additionally, Cu-DBC was synthesized using a solvothermal synthesis method based on a previously reported protocol.[29] As shown in Figure 7.4, the powder XRD pattern confirms that the electrochemically synthesized Cu-DBC powder (blue line) exhibits characteristic peaks consistent with those of the solution-synthesized sample (red line), indicating successful formation of the Cu-DBC structure. Additionally, no peaks corresponding to Cu metal or Cu oxides were detected in the XRD analysis. However, several weak additional peaks were

observed from the XRD pattern of electrochemically synthesized Cu-DBC, which likely originate from residual ligands that have been difficult to remove during the purification process (grey line). The presence of these residual ligands may be attributed to several factors. First, the interpenetrated structure of Cu-DBC could trap ligand molecules within the framework's pores, making them resistant to removal by standard filtering process. Second, oxidized ligands that failed to coordinate with Cu exhibit poor solubility, potentially leading to the formation of aggregates or poorly soluble oligomers during synthesis. The weak additional peaks observed in the XRD pattern may correspond to crystalline components within these aggregates. The unpaired spins are typically unstable and can be quenched by exposure to air or the applied voltage during synthesis. It is highly unlikely for such radicals to survive in an air environment without forming a stabilizing structure, suggesting that these aggregates don't affect the MOF properties.[13, 228] The morphology of both solution synthesized Cu-DBC and electrochemical synthesized Cu-DBC was revealed by scanning electron microscopy (SEM). Stick-like structures with a width ranging from 20 –100 nm were observed (Figure 7.4b, c).

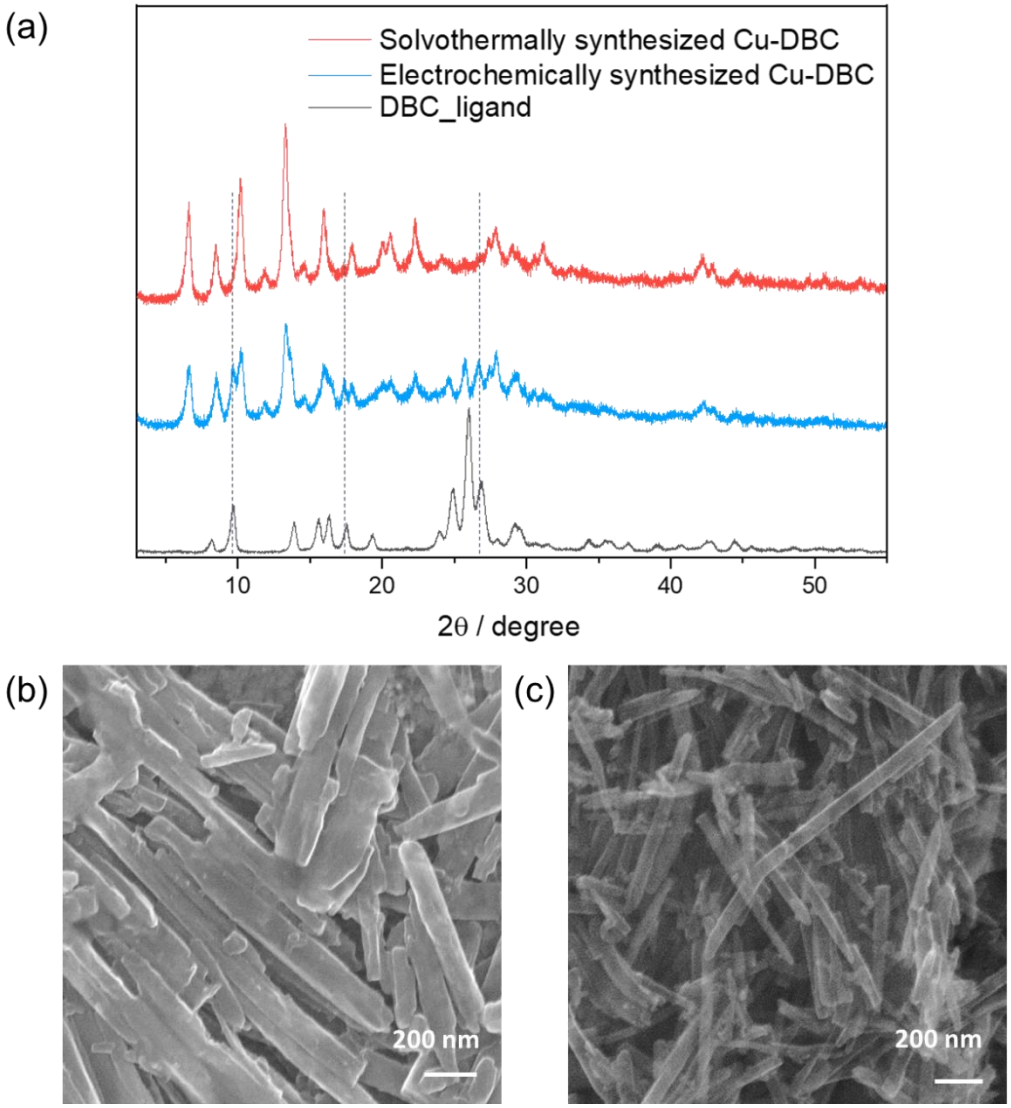

Figure 7. 4: (a) XRD pattern confirming the formation of solution synthesized (blue line) and electrochemically synthesized (red line) Cu-DBC. (b) SEM image of electrochemical synthesized Cu-DBC (c) SEM image of solution synthesized Cu-DBC.

7.3.2 The charge state of Cu

Continuous wave (CW)-EPR measurement was conducted to confirm the redox state of copper in both samples. From Figure 7.5a, the CW-EPR spectrum of solution synthesized Cu-DBC displays a strong signal at g= 2.1, confirming the high spin concentration of paramagnetic Cu^{2+}, and a weak signal at g=2.002 originating from the organic ligand.[21] The electrochemically

synthesized Cu-DBC exhibits only a strong peak at g = 2.002 (Figure 7.5b). The narrow linewidth 0.7 mT aligns with characteristic features observed in organic radicals.[124] The EPR signal from Cu^{2+} ions for the electrochemical-synthesized Cu-DBC was very weak.[229]

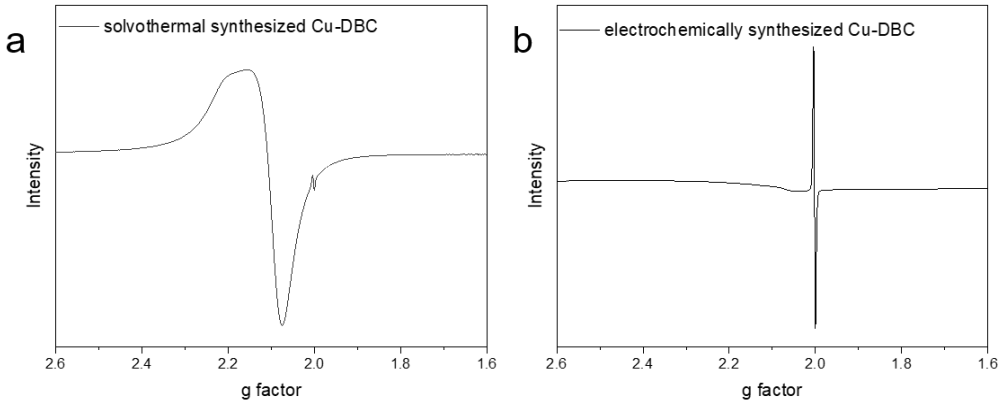

Figure 7. 5**:** CW-EPR spectra of (a) solution-synthesized and (b) electrochemically synthesized Cu-DBC at 80K. The broad peak indicates the presence of Cu^{2+}, the sharp peak indicates organic radicals.

XPS analysis was conducted to confirm the oxidation states difference of Cu in solution synthesized Cu-DBC and electrochemically synthesized Cu-DBC (Figure 7.6). The analysis shows the coexistence of Cu^{2+} and Cu^{+} in Cu-DBC from both synthesis methods. In the solution-synthesized Cu-DBC, the spectrum shows a dominant Cu^{2+} peak, along with strong satellites, indicating that Cu^{2+} ions are dominant in the MOF (Figure 7.6a).[43, 105] In contrast, the electrochemically synthesized Cu-DBC shows a strong peak at about 933.1eV, indicating the dominance of Cu^{+} (Figure 7.6b).[43, 105]

Both solvothermally synthesized and electrochemically synthesized Cu-DBC exhibit the co-existence of Cu^{2+} and Cu^{+}, as demonstrated by CW-EPR and XPS results. Although XPS is a surface-sensitive technique and may not provide precise quantitative analysis, the combined findings of XPS and CW-EPR reveal a decreased amount of Cu^{2+} in electrochemically synthesized Cu-DBC compared to the solvothermally synthesized Cu-DBC. Notably, CW-EPR shows a pronounced strong peak corresponding to an organic radical, suggesting that the

oxidized ligand may reduce Cu ions. This reduction likely establishes an equilibrium between $Cu^{2+}Cu^{2+}$-DBC^{4-} and $Cu^{2+}Cu^{+}$-DBC^{3-} units, facilitating a transition from a Cu^{2+} spin-dominated MOF to one dominated by organic radicals.

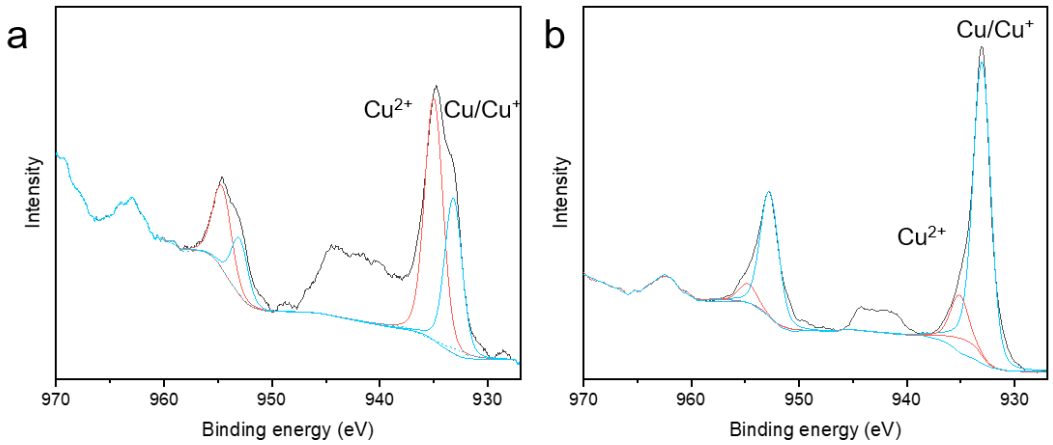

Figure 7. 6: Cu 2p XPS spectra of (a) solution synthesized and (b) electrochemically synthesized Cu-DBC, showing the co-existence of Cu^{+} and Cu^{2+} in both samples. A decreased intensity of the Cu^{2+} peak and satellite features is observed for the electrochemically synthesized Cu-DBC.

Notably, we employed the same electrochemical synthesis method for Cu_3HHTP_2, as discussed in previous chapters. Unlike the distorted diamond structure of Cu-DBC, $Cu_3(HHTP)_2$ exhibits a square-planar configuration within each layer, with the layers held together by π-π interactions (Figure 7.7a). The CW EPR spectrum of the electrochemically synthesized Cu_3HHTP_2 reveals a broad signal attributed to Cu^{2+}, with no detectable signals from organic radicals (Figure 7.7b). XPS results further indicate that Cu^{2+} remains predominant (Figure 7.7c). These findings demonstrate that the electrochemically synthesized Cu-HHTP does not show a significant increase of Cu^{+} or radical formation, confirming the importance of ligand structure in tuning the Cu oxidation state. According to the crystal field theory, the d^9 state in Cu^{2+} prefers a square planar coordination geometry, while the d^{10} state in Cu^{+} prefers tetrahedral geometry.[31, 36] Compared to square planar coordination geometry-based MOFs, the non-planar structure of

DBC and its distorted diamond network binding may minimize structural distortion of the framework during Cu reduction and ligand oxidation.[36] This characteristic could play a role in the charge state change of Cu during MOF formation. The oxidized ligand could possibly reduce Cu ions and finally leads to an equilibrium between Cu^{2+}-DBC^{4-} and Cu^{+}-$DBC^{3-\cdot}$ units thereby facilitating a conversion from a Cu^{2+} spin dominating MOF to an organic radical-dominating MOF.

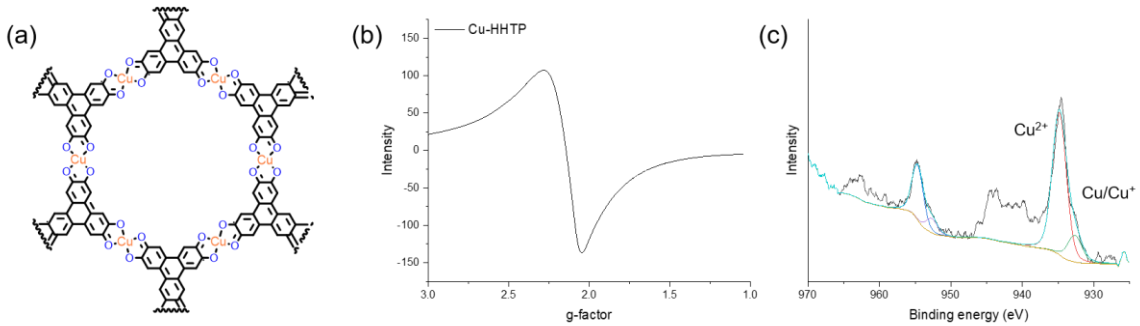

Figure 7. 7: (a) Chemical structure of Cu_3HHTP_2. (b) CW-EPR spectrum of electrochemically synthesized Cu_3HHTP_2, showing a broad Cu^{2+} peak. (c) Cu 2p XPS spectra of electrochemically synthesized Cu_3HHTP_2, showing strong Cu^{2+} peak.

7.3.3 Spin dynamic behavior

These results prompted us to measure the spin behaviour of the electrochemically synthesized Cu-DBC and solvothermally synthesized Cu-DBC using pulse-EPR spectroscopy. The solvothermally synthesized Cu-DBC shows strong paramagnetic behaviour from a more homogeneous dispersion of Cu^{2+}.[29, 223] Such high spin concentration leads to strong increased spin-spin dipolar interactions between electron spins, and thus undetectable spin echo at room temperature.[127, 230] For electrochemically synthesized Cu-DBC, we first measured its relaxation dynamics at room temperature. Each measurement was carried out at the peak of maximum intensity of its echo-detected field-swept (EDFS) spectra (Figure 7.8).

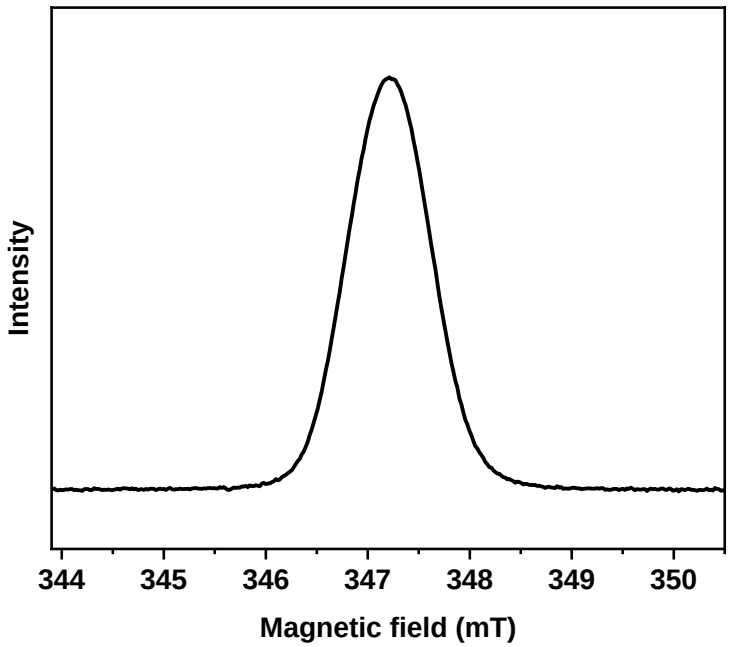

Figure 7. 8: Echo-detected field-swept (EDFS) EPR spectrum of Cu-DBC recorded at room temperature using pulsed EPR.

A two-pulse Hahn echo sequence was performed to measure the phase memory time (T_m) of the electronic spins in Cu-DBC (Figure 7.9a), inversion recovery was performed to measure the spin-lattice relaxation time (T_1) (Figure 7.9b). The Hahn echo decay curve was fitted with a stretched exponential subtraction, and the spin lattice relaxation data was fitted with a bi-exponential fitting, both of which are detailed in the Methodology chapter. The crystalline powder Cu-DBC show room temperature T_1 of 24.5 μs, and T_m of 405 ns without dilution and further optimization. Such relaxation time exceeds many metal-based molecular qubits, which typically function only at low temperatures.[121, 129, 131]

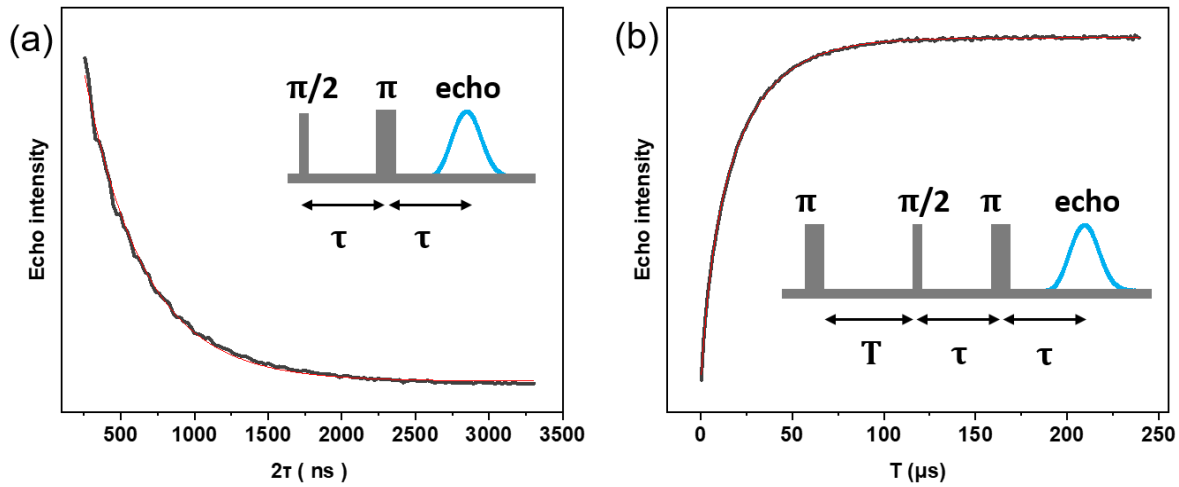

Figure 7.9: (a) Two-pulse Hahn echo decay of Cu-DBC (black line) and stretched exponential decay fit (red line) at room temperature. Inset is the pulse sequence for the Hahn echo decay experiment. (b) Inversion recovery experiment (black line) and biexponential fit (red line) at room temperature for Cu-DBC. Inset is the pulse sequence for the inversion recovery experiment.

Encouraged by the room temperature long coherence times of the Cu-DBC, we further investigated the thermal variations of T_m and T_1 for Cu-DBC. At 5K, the longest T_m around 1.5 μs was detected (Figure 7.10a), and the spin-lattice relaxation time T_1 is about 550 μs (Figure 7.10b). Figure 7.10c shows the T_m and T_1 data extracted from the experimental decay curves, both T_1 and T_m showed temperature dependent behaviour. The much shorter T_m than T_1 throughout all temperatures indicates that the phonon decoherence is not the main limitation of spin coherence.[128, 231]

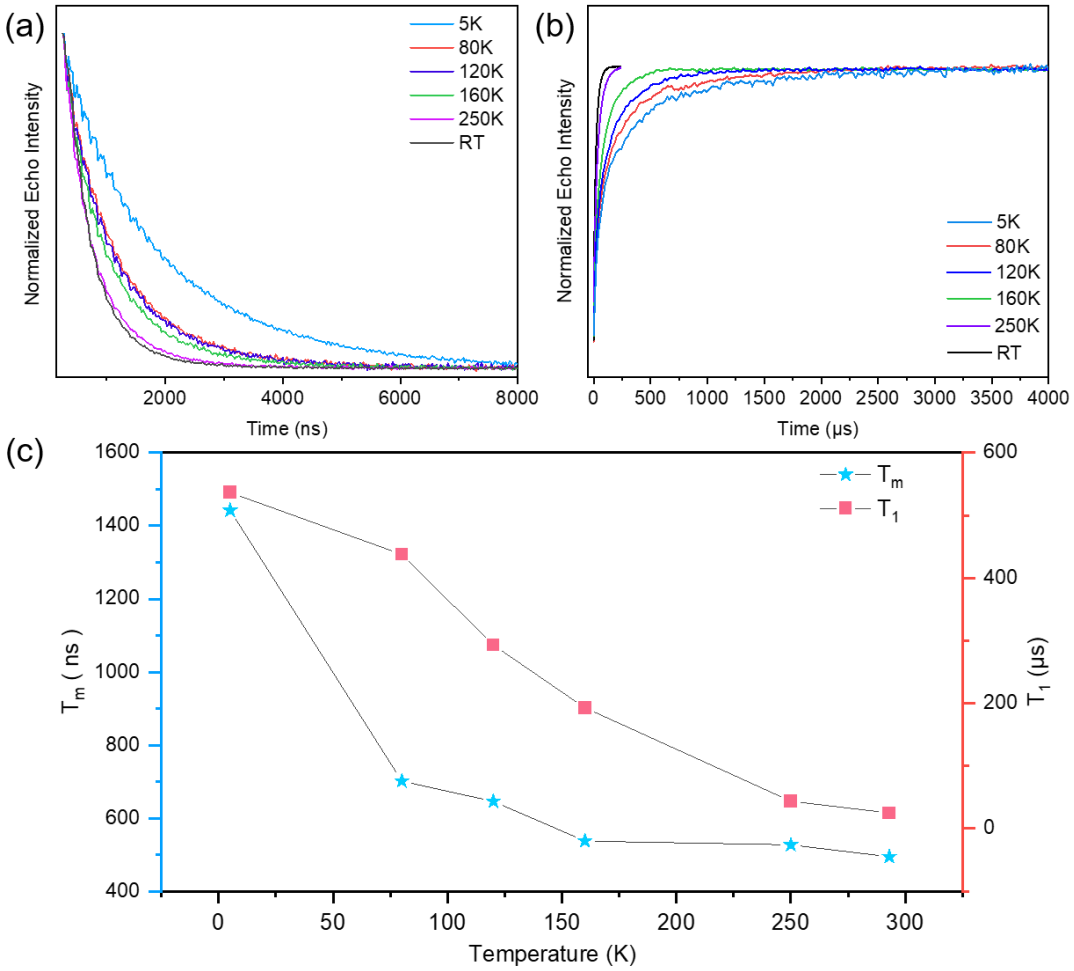

Figure 7. 10: (a) Hahn echo measurements of T_m and (b) Inversion recovery measurements of T_1 at various temperatures. (c) Temperature dependence of T_1 and T_m of Cu-DBC.

To understand decoherence due to nuclear spin coupling in Cu-DBC, combination peak electron spin echo envelope modulation (CP-ESEEM) measurement was performed at room temperature (Figure 7.11a). Combination-peak (CP) ESEEM allows the detailed analysis of the combination frequencies ω by applying a four-pulse sequence.[20, 116] The time domain CP-ESEEM spectrum was transformed to frequency-domain CP-ESEEM spectra. As shown in Figure 7.11b, a strong peak centred at 29.8 MHz, which is the double Larmor frequency of ^{1}H.[126] A weaker peak of ^{13}C was at 7.5 MHz was observed, which is the double frequency of Larmor frequency of ^{13}C.[126] Notably, the $2\omega^{13}$C peak is more intense than the ω^{1}H peak, characteristic of spin delocalisation

over an extended carbon framework of the semiquinone molecule.[126] These results suggest the coupling of electron spins to ^{1}H and ^{13}C nuclei, hence further increases in phase memory times may be possible with isotopic enrichment of ^{2}H and ^{12}C.

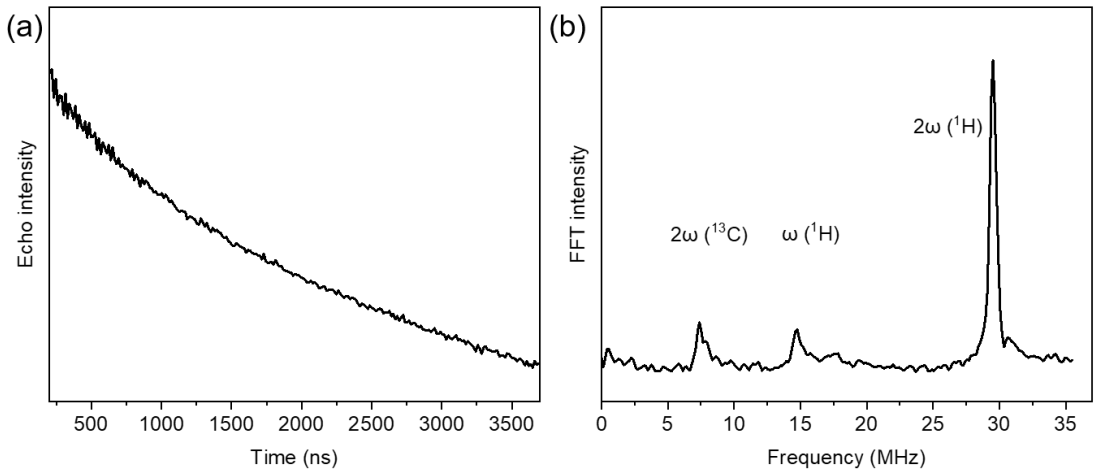

Figure 7. 11: (a) Time-domain CP-ESEEM spectrum of Cu-DBC at 296 K. (b) Frequency-domain CP-ESEEM spectra of Cu-DBC under a field of 343.8 mT.

7.4 Conclusion and outlook

In summary, we found that the non-planar Cu-DBC was a candidate as an organic radical-based MOF. By employing electrochemistry synthesis, the ligand can be oxidized on the electrode and then affect the amount of Cu^{+} and organic radical. The organic radical-based MOF exhibit long room temperature coherence time, thereby making the conductive MOFs qubit candidates. The resulting MOF demonstrates room temperature coherence of 405 ns, demonstrating noteworthy coherence time even without dilution and optimization. We observed coupling of electronic spins with ^{1}H and ^{13}C nuclei at room temperature, leading to decoherence. We demonstrated that electrochemical synthesis is a promising approach for the manipulation of the oxidation state for organic radical and metal, which allows changes of the magnetic property and spin density of the MOF.

Electrochemical synthesis of MOFs provides a promising strategy to tune the oxidation states of metal centres and ligands. However, achieving quantitative control over the ratio of mixed-valence states presents a significant challenge. Another challenge is synthesizing pure Cu-DBC MOF without ligand residues. Furthermore, the inherent air sensitivity of catechol-based ligands adds another layer of complexity, making it difficult to ensure consistent reproducibility across different batches. To address these challenges, future research should prioritize optimizing the purification process and mitigating the air sensitivity of catechol-based ligands, which is a critical barrier to reproducible synthesis. One effective strategy involves performing ligand synthesis and handling under an inert atmosphere, such as argon or nitrogen, to minimize exposure to oxygen and moisture.

Chapter 8

Summary and future look

This chapter begins with a summary of the key results achieved throughout this research and then a discussion of their implications, particularly in the context of structure-property relationships in conductive MOFs. Building on these findings, the chapter concludes with an outlook on future directions.

8.1 Conclusions

This thesis has demonstrated how synthetic control over the orientation, morphology, processability, and redox chemistry of conductive metal–organic frameworks (MOFs) can be leveraged to modulate their electronic and spintronic behaviour. Through a combination of electrochemical and solvothermal methods, the work establishes new strategies for fabricating MOFs with tailored structural features and explores their implications for chemiresistive sensing and spin functionality.

A dual-working-electrode electrochemical method was developed to grow $Cu_3(HHTP)_2$ films with controlled orientation directly on conductive substrates. By tuning the ligand concentration, both face-on and edge-on films were synthesised, revealing highly anisotropic charge transport, with in-plane conductivity surpassing out-of-plane by over three orders of magnitude. The same

method was adapted for device integration, where orientation-dependent performance in ammonia sensing was confirmed, edge-on films offered good sensitivity and reproducibility.

Building on the need for processable and scalable materials, modulator- and surfactant-assisted solvothermal synthesis enabled the preparation of solution-processable $Cu_3(HHTP)_2$ nanomaterials with controlled morphology and excellent colloidal stability. These materials demonstrated effective sensing behaviour when deposited via spray coating. Lastly, a redox-active 3D MOF (Cu-DBC) was synthesised electrochemically to study the formation of ligand-centred radicals and their spin dynamics. Room-temperature spin relaxation times were observed.

The outcomes of this thesis provide valuable insights into how structural and chemical control in MOF synthesis can be used to engineer the electronic and spin properties of conductive MOFs. The orientation-controlled growth of 2D MOF films offers a reproducible route for tuning anisotropic conductivity, which is critical for applications in thin-film electronics. The chemiresistive responses of MOFs were shown to depend on the stacking direction of the 2D films relative to analyte exposure. The development of solution-processable MOF nanocrystals further supports the integration of conductive MOFs into key limitations in scalable devices. Moreover, the redox tuning in conductive MOFs highlight the potential of conductive MOFs as candidates for molecular spintronic applications.

In summary, this thesis emphasizes the pivotal role of synthetic control in tuning the morphology, structure, processability, and redox state of conductive MOFs. Maximizing the potential of 2D c-MOFs will require an integrated approach that combines molecular design, structural precision, and device-level fabrication. Such a strategy will be essential for advancing these materials toward applications in electronics and spintronics.

8.2 Future outlook

This thesis presents new methods for the synthesis and functionalisation of conductive MOFs. While these approaches show significant promise, several limitations have emerged that highlight key areas for future research. The dual-working-electrode method enabled controlled growth of $Cu_3(HHTP)_2$ films but showed limited applicability to other frameworks such as $Cu_3(HHTP)_2$ or metal centres like Zn and Mg, indicating that redox compatibility between the metal and ligand is critical. To improve versatility, future efforts can focus on incorporating external oxidants and refining electrochemical protocols. In the context of 2D MOFs for chemiresistive gas sensing, a better understanding of gas-MOF interactions is essential. In situ characterisation techniques will be important for understanding the sensing mechanisms. For solution-processable MOF nanocrystals, tuning additive concentrations offers a practical route to control particle size, film morphology, and overall sensor performance. Finally, redox-active MOFs such as Cu-DBC face challenges in reproducibility due to the air sensitivity of catechol-based ligands and the presence of residual impurities. These issues underscore the need for synthesis under inert conditions and clean post-synthetic treatments.

Beyond the specific systems studied in this thesis, several broader challenges emerge to advancing the field of 2D conductive MOFs. The first major challenge lies in the presence and control of structural defects. Defects such as edge terminations, vacancies, and stacking faults can significantly affect their properties. However, these defects are often introduced during synthesis and remain poorly understood, limiting the precise structure-property relationship, and reproducibility of material performance. The fabrication of atomically thin 2D MOFs using vacuum growth techniques, such as chemical vapor deposition with scanning tunneling microscopy, offers a promising route to understand the formation and the role of these defects. These approaches enable the growth of monolayer MOFs with well-defined structures, allowing

atomically resolved characterization of metal centre distributions and electronic structures. Such systems might provide critical insight into defect generation mechanisms and their impact on electronic and spintronic properties, establishing a foundation for rational defect control in future synthetic strategies.

The second challenge is the limited availability of high-resolution characterisation techniques capable of resolving these defects at the atomic scale. Most current studies rely on bulk techniques such as PXRD, which provide only averaged structural information and are insufficient to detect local disorder or to distinguish between different types of defect. Advanced imaging and spectroscopy tools-such as scanning transmission electron microscopy (STEM) or tip-enhanced Raman spectroscopy will be essential for mapping defect landscapes and correlating them with physical properties.

The third and closely related challenge is to achieve high-quality single crystals of 2D c-MOFs. Despite recent advances in synthesis methods, most reported materials exhibit small crystal sizes. This is largely due to poor control over nucleation and crystal growth kinetics. As a result, the structures of many 2D π-conjugated MOFs are inferred from simulated PXRD patterns rather than determined directly, obscuring critical features such as interlayer stacking arrangements and pore content. Synthesis under inert or ultra-clean conditions may offer a route to improving crystal quality and facilitating the growth of larger, well-ordered single crystals suitable for detailed structural analysis.Moreover, electrical conductivity between MOF crystallites remains limited. Grain boundaries often act as resistive barriers, disrupting continuous charge transport across the film. Improving inter-grain conductivity is therefore important for fully realising the potential of conductive MOFs in device applications. Strategies such as promoting oriented or epitaxial growth, engineering nanostructures, and designing

percolation pathways can help improve grain alignment and facilitate more efficient charge transport across crystallite interfaces.

Despite progress in both synthesis and characterisation, these challenges also point to the need for the rational design of conjugated ligands. Ligand design offers a powerful route to influence not only the electronic properties of 2D frameworks but also their crystallinity, defect tolerance, and stacking behaviour. Future ligand architectures should be guided by computational models and validated through experiment.

References

1. Fan, W.; Zhang, X.; Kang, Z.; Liu, X.; Sun, D., Isoreticular chemistry within metal–organic frameworks for gas storage and separation. *Coordination chemistry reviews* 2021, *443*, 213968.

2. Sun, N.; Shah, S. S. A.; Lin, Z.; Zheng, Y.-Z.; Jiao, L.; Jiang, H.-L., MOF-Based Electrocatalysts: An Overview from the Perspective of Structural Design. *Chemical Reviews* 2025, *125* (5), 2703-2792.

3. Sun, L.; Campbell, M. G.; Dinca, M., Electrically Conductive Porous Metal-Organic Frameworks. *Angew. Chem., Int. Ed.* 2016, *55* (11), 3566-79.

4. Ko, M.; Mendecki, L.; Mirica, K. A., Conductive two-dimensional metal-organic frameworks as multifunctional materials. *Chem. Commun.* 2018, *54* (57), 7873-7891.

5. Xie, L. S.; Skorupskii, G.; Dincă, M., Electrically conductive metal–organic frameworks. *Chem. Rev.* 2020, *120* (16), 8536-8580.

6. Liu, J.; Chen, Y.; Feng, X.; Dong, R., Conductive 2D Conjugated Metal–Organic Framework Thin Films: Synthesis and Functions for (Opto-) electronics. *Small Struc.* 2022, 2100210.

7. Lu, Y.; Samorì, P.; Feng, X., Rational Construction of Two-Dimensional Conjugated Metal–Organic Frameworks (2D c-MOFs) for Electronics and Beyond. *Accounts of Chemical Research* 2024, *57* (14), 1985-1996.

8. Yan, X.; Su, X.; Chen, J.; Jin, C.; Chen, L., Two-Dimensional Metal-Organic Frameworks Towards Spintronics. *Angewandte Chemie International Edition*, e202305408.

9. Wang, M.; Dong, R.; Feng, X., Two-dimensional conjugated metal–organic frameworks (2D c-MOFs): chemistry and function for MOFtronics. *Chem. Soc. Rev.* 2021, *50* (4), 2764-2793.

10. Furukawa, H.; Cordova, K. E.; O'Keeffe, M.; Yaghi, O. M., The chemistry and applications of metal-organic frameworks. *Science* 2013, *341* (6149), 1230444.

11. Sheberla, D.; Sun, L.; Blood-Forsythe, M. A.; Er, S.; Wade, C. R.; Brozek, C. K.; Aspuru-Guzik, A.; Dinca, M., High electrical conductivity in Ni_3(2,3,6,7,10,11-hexaiminotriphenylene)$_2$, a semiconducting metal-organic graphene analogue. *J. Am. Chem. Soc.* 2014, *136* (25), 8859-62.

12. Hmadeh, M.; Lu, Z.; Liu, Z.; Gándara, F.; Furukawa, H.; Wan, S.; Augustyn, V.; Chang, R.; Liao, L.; Zhou, F.; Perre, E.; Ozolins, V.; Suenaga, K.; Duan, X.; Dunn, B.; Yamamto, Y.; Terasaki, O.; Yaghi, O. M., New Porous Crystals of Extended Metal-Catecholates. *Chem. Mater.* 2012, *24* (18), 3511-3513.

13. Hicks, R., *Stable radicals: fundamentals and applied aspects of odd-electron compounds*. John Wiley & Sons: 2011.

14. Jeong, H.; Park, G.; Jeon, J.; Park, S. S., Fabricating Large-Area Thin Films of 2D Conductive Metal–Organic Frameworks. *Acc. Chem. Res.* 2024, 16726-16731.

15. Johnson, E. M.; Ilic, S.; Morris, A. J., Design strategies for enhanced conductivity in metal–organic frameworks. *ACS Cent. Sci.* 2021, *7* (3), 445-453.

16. Day, R. W.; Bediako, D. K.; Rezaee, M.; Parent, L. R.; Skorupskii, G.; Arguilla, M. Q.; Hendon, C. H.; Stassen, I.; Gianneschi, N. C.; Kim, P., Single crystals of electrically conductive two-dimensional metal–organic frameworks: Structural and electrical transport properties. *ACS Cent. Sci.* 2019, *5* (12), 1959-1964.

17. Lu, C.; Clayville, B.; Choi, J. Y.; Park, J., 2D metal-organic frameworks as an emerging platform with tunable electronic structures. *Chem* 2023, *9* (10), 2757-2770.

18. Mohammad-Pour, G. S.; Hatfield, K. O.; Fairchild, D. C.; Hernandez-Burgos, K.; Rodriguez-Lopez, J.; Uribe-Romo, F. J., A Solid-Solution Approach for Redox Active Metal-

Organic Frameworks with Tunable Redox Conductivity. *J. Am. Chem. Soc.* 2019, *141* (51), 19978-19982.

19. Miner, E. M.; Wang, L.; Dincă, M., Modular O_2 electroreduction activity in triphenylene-based metal–organic frameworks. *Chem. Sci.* 2018, *9* (29), 6286-6291.

20. Sun, L.; Yang, L.; Dou, J.-H.; Li, J.; Skorupskii, G.; Mardini, M.; Tan, K. O.; Chen, T.; Sun, C.; Oppenheim, J. J., Room-temperature quantitative quantum sensing of lithium ions with a radical-embedded metal–organic framework. *J. Am. Chem. Soc.* 2022, *144* (41), 19008-19016.

21. Chen, Y.; Zhu, Q.; Fan, K.; Gu, Y.; Sun, M.; Li, Z.; Zhang, C.; Wu, Y.; Wang, Q.; Xu, S., Successive Storage of Cations and Anions by Ligands of π–d-Conjugated Coordination Polymers Enabling Robust Sodium-Ion Batteries. *Angew. Chem., Int. Ed.* 2021, *133* (34), 18917-18924.

22. Skorupskii, G.; Chanteux, G.; Le, K. N.; Stassen, I.; Hendon, C. H.; Dincă, M., Electrical conductivity through π–π stacking in a two-dimensional porous gallium catecholate metal–organic framework. *Ann. N. Y. Acad. Sci.* 2022, *1518* (1), 226-230.

23. Hinckley, A. C.; Park, J.; Gomes, J.; Carlson, E.; Bao, Z., Air-Stability and Carrier Type in Conductive M_3(Hexaaminobenzene)$_2$, (M = Co, Ni, Cu). *J. Am. Chem. Soc.* 2020, *142* (25), 11123-11130.

24. Pham, H. T.; Choi, J. Y.; Stodolka, M.; Park, J., Maximizing the Potential of Electrically Conductive MOFs. *Acc. Chem. Res.* 2024, *57* (4), 580-589.

25. Meng, Z.; Mirica, K. A., Two-dimensional d-π conjugated metal-organic framework based on hexahydroxytrinaphthylene. *Nano Res.* 2020, *14* (2), 369-375.

26. Chen, T.; Dou, J.-H.; Yang, L.; Sun, C.; Libretto, N. J.; Skorupskii, G.; Miller, J. T.; Dincă, M., Continuous electrical conductivity variation in M_3(hexaiminotriphenylene)$_2$ (M= Co, Ni, Cu) MOF alloys. *J. Am. Chem. Soc.* 2020, *142* (28), 12367-12373.

27. Zhang, X.; Tian, X.; Wu, N.; Zhao, S.; Qin, Y.; Pan, F.; Yue, S.; Ma, X.; Qiao, J.; Xu, W., Metal-organic frameworks with fine-tuned interlayer spacing for microwave absorption. *Sci. Adv.* 2024, *10* (11), eadl6498.

28. Liu, J.; Xing, G.; Chen, L., 2D Conjugated Metal–Organic Frameworks: Defined Synthesis and Tailor-Made Functions. *Acc. Chem. Res.* 2024, *57* (7), 1032-1045.

29. Liu, J.; Zhou, Y.; Xie, Z.; Li, Y.; Liu, Y.; Sun, J.; Ma, Y.; Terasaki, O.; Chen, L., Conjugated copper–catecholate framework electrodes for efficient energy storage. *Angew. Chem., Int. Ed.* 2020, *59* (3), 1081-1086.

30. Skorupskii, G.; Trump, B. A.; Kasel, T. W.; Brown, C. M.; Hendon, C. H.; Dinca, M., Efficient and tunable one-dimensional charge transport in layered lanthanide metal-organic frameworks. *Nat. Chem.* 2020, *12* (2), 131-136.

31. Gütlich, P.; Goodwin, H.; Hendrickson, D. N.; Pierpont, C. G., *Spin Crossover in Transition Metal Compounds II*. 2004; p 63-95.

32. Osterbrink, J.; Walter, P.; Leingang, S.; Pfisterer, H.; Kaifer, E.; Himmel, H. J., Quantitative Electromerism of a Well-defined Mononuclear Copper Complex Through Reversible Intramolecular Metal-Ligand Electron Transfer. *Chem. Eur. J.* 2023, *29* (32), e202300514.

33. Albold, U.; Hoyer, C.; Neuman, N. I.; Sobottka, S.; Hazari, A. S.; Lahiri, G. K.; Sarkar, B., Isolable Cu (I) complexes of extremely electron-poor, completely unreduced o-Quinone and "Di-o-Quinone" ligands stabilized through π–π interactions in the secondary coordination sphere. *Inorg. Chem.* 2019, *58* (6), 3754-3763.

34. Wang, J.; Chen, T.; Jeon, M.; Oppenheim, J. J.; Tan, B.; Kim, J.; Dincă, M., Superior charge transport in Ni-diamine conductive MOFs. *J. Am. Chem. Soc.* 2024, *146*, 20500-20507.

35. Roy, S.; Sarkar, B.; Bubrin, D.; Niemeyer, M.; Zalis, S.; Lahiri, G. K.; Kaim, W., Stabilizing the elusive ortho-quinone/copper (I) oxidation state combination through π/π interaction in an isolated complex. *J. Am. Chem. Soc.* 2008, *130* (46), 15230-15231.

36. Fan, K.; Li, J.; Xu, Y.; Fu, C.; Chen, Y.; Zhang, C.; Zhang, G.; Ma, J.; Zhai, T.; Wang, C., Single crystals of a highly conductive three-dimensional conjugated coordination polymer. *J. Am. Chem. Soc.* 2023, *145* (23), 12682-12690.

37. Ye, S.; Sarkar, B.; Niemeyer, M.; Kaim, W., Mixed-Ligand Copper Complexes with 8-Methylthioquinoline and Triphenylphosphane or the o-Semiquinone/Catecholate Redox System. *Eur. J. Inorg. Chem.* 2005, 4735–4738.

38. Gómez-Herrero, A. C.; Sánchez-Sánchez, C.; Chérioux, F.; Martínez, J. I.; Abad, J.; Floreano, L.; Verdini, A.; Cossaro, A.; Mazaleyrat, E.; Guisset, V., Copper-assisted oxidation of catechols into quinone derivatives. *Chem. Sci.* 2021, *12* (6), 2257-2267.

39. Du, X.; Zhang, J.; Wang, H.; Huang, Z.; Guo, A.; Zhao, L.; Niu, Y.; Li, X.; Wu, B.; Liu, Y., Solid–solid interface growth of conductive metal–organic framework nanowire arrays and their supercapacitor application. *Mater. Chem. Front.* 2020, *4* (1), 243-251.

40. Grange, C. S.; Meijer, A. J.; Ward, M. D., Trinuclear ruthenium dioxolene complexes based on the bridging ligand hexahydroxytriphenylene: electrochemistry, spectroscopy, and near-infrared electrochromic behaviour associated with a reversible seven-membered redox chain. *Dalton Trans.* 2010, *39* (1), 200-211.

41. Nguyen, N. T.; Furukawa, H.; Gándara, F.; Trickett, C. A.; Jeong, H. M.; Cordova, K. E.; Yaghi, O. M., Three-dimensional metal-catecholate frameworks and their ultrahigh proton conductivity. *J. Am. Chem. Soc.* 2015, *137* (49), 15394-15397.

42. Misumi, Y.; Yamaguchi, A.; Zhang, Z.; Matsushita, T.; Wada, N.; Tsuchiizu, M.; Awaga, K., Quantum spin liquid state in a two-dimensional semiconductive metal–organic framework. *J. Am. Chem. Soc.* 2020, *142* (39), 16513-16517.

43. Fan, K.; Zhang, C.; Chen, Y.; Wu, Y.; Wang, C., The chemical states of conjugated coordination polymers. *Chem* 2021, *7* (5), 1224-1243.

44. Jiang, Y.; Oh, I.; Joo, S. H.; Seo, Y.-S.; Lee, S. H.; Seong, W. K.; Kim, Y. J.; Hwang, J.; Kwak, S. K.; Yoo, J.-W., Synthesis of a copper 1, 3, 5-triamino-2, 4, 6-benzenetriol metal–organic framework. *J. Am. Chem. Soc.* 2020, *142* (43), 18346-18354.

45. Campbell, M. G.; Sheberla, D.; Liu, S. F.; Swager, T. M.; Dinca, M., Cu_3(hexaiminotriphenylene)$_2$: an electrically conductive 2D metal-organic framework for chemiresistive sensing. *Angew. Chem., Int. Ed.* 2015, *54* (14), 4349-4352.

46. Song, M.; Jia, J.; Li, P.; Peng, J.; Pang, X.; Qi, M.; Xu, Y.; Chen, L.; Chi, L.; Lu, G., Ligand-Oxidation-Based Anodic Synthesis of Oriented Films of Conductive M-Catecholate Metal–Organic Frameworks with Controllable Thickness. *J. Am. Chem. Soc.* 2023, *145*, 25570-25578.

47. Yang, L.; He, X.; Dincă, M., Triphenylene-bridged trinuclear complexes of Cu: Models for spin interactions in two-dimensional electrically conductive metal–organic frameworks. *J. Am. Chem. Soc.* 2019, *141* (26), 10475-10480.

48. Yang, L.; Dincă, M., Redox Ladder of Ni_3 Complexes with Closed-Shell, Mono-, and Diradical Triphenylene Units: Molecular Models for Conductive 2D MOFs. *Angew. Chem., Int. Ed.* 2021, *133* (44), 23977-23982.

49. Hoshino, N.; Akutagawa, T., A Trinuclear Iron (III) Complex of a Triple Noninnocent Ligand for Spin-Structured Molecular Conductors. *Chem. Eur. J.* 2018, *24* (72), 19323-19331.

50. Sakamoto, R.; Kambe, T.; Tsukada, S.; Takada, K.; Hoshiko, K.; Kitagawa, Y.; Okumura, M.; Nishihara, H., π-conjugated trinuclear group-9 metalladithiolenes with a triphenylene backbone. *Inorg. chem.* 2013, *52* (13), 7411-7416.

51. Intrator, J. A.; Orchanian, N. M.; Clough, A. J.; Haiges, R.; Marinescu, S. C., Electronically-coupled redox centers in trimetallic cobalt complexes. *Dalton Trans.* 2022, *51* (14), 5660-5672.

52. Foster, M. E.; Sohlberg, K.; Allendorf, M. D.; Talin, A. A., Unraveling the semiconducting/metallic discrepancy in $Ni_3(HITP)_2$. *J. Phys. Chem. Lett.* 2018, *9* (3), 481-486.

53. Debela, T. T.; Hendon, C. H., Hydrogenic Defects in Ferromagnetic $Cu_3(HITP)_2$ (HITP≡ 2, 3, 6, 7, 10, 11-Hexaiminotriphenylene), a 2D Metal–Organic Framework. *ACS Mater. Lett.* 2024, *6*, 2698-2702.

54. Roh, H.; Kim, D. H.; Cho, Y.; Jo, Y. M.; Del Alamo, J. A.; Kulik, H. J.; Dincă, M.; Gumyusenge, A., Robust Chemiresistive Behavior in Conductive Polymer/MOF Composites. *Adv. Mater.* 2024, *36*, 2312382.

55. Li, H. Y.; Zhao, S. N.; Zang, S. Q.; Li, J., Functional metal-organic frameworks as effective sensors of gases and volatile compounds. *Chem. Soc. Rev.* 2020, *49* (17), 6364-6401.

56. Sheberla, D.; Bachman, J. C.; Elias, J. S.; Sun, C. J.; Shao-Horn, Y.; Dinca, M., Conductive MOF electrodes for stable supercapacitors with high areal capacitance. *Nat. Mater.* 2017, *16* (2), 220-224.

57. Snook, K. M.; Zasada, L. B.; Chehada, D.; Xiao, D. J., Oxidative control over the morphology of $Cu_3(HHTP)_2$, a 2D conductive metal–organic framework. *Chem. Sci.* 2022, *13* (35), 10472-10478.

58. Hoppe, B.; Hindricks, K. D. J.; Warwas, D. P.; Schulze, H. A.; Mohmeyer, A.; Pinkvos, T. J.; Zailskas, S.; Krey, M. R.; Belke, C.; König, S.; Fröba, M.; Haug, R. J.; Behrens, P., Graphene-like metal–organic frameworks: morphology control, optimization of thin film electrical conductivity and fast sensing applications. *CrystEngComm* 2018, *20* (41), 6458-6471.

59. Chen, J. E.; Yang, Z. J.; Koh, H. U.; Shen, J.; Cai, Y.; Yamauchi, Y.; Yeh, L. H.; Tung, V.; Wu, K. C. W., Current Progress and Scalable Approach toward the Synthesis of 2D Metal–Organic Frameworks. *Adv. Mater. Interfaces* 2022, *9* (13), 2102560.

60. Gittins, J. W.; Balhatchet, C. J.; Fairclough, S. M.; Forse, A. C., Enhancing the energy storage performances of metal–organic frameworks by controlling microstructure. *Chem. Sci.* 2022, *13* (32), 9210-9219.

61. Shan, Z.; Xiao, J. Z.; Wu, M.; Wang, J.; Su, J.; Yao, M. S.; Lu, M.; Wang, R.; Zhang, G., Topologically Tunable Conjugated Metal–Organic Frameworks for Modulating Conductivity and Chemiresistive Properties for NH_3 Sensing. *Angew. Chem., Int. Ed.* 2024, *63* (16), e202401679.

62. Marshall, C. R.; Staudhammer, S. A.; Brozek, C. K., Size control over metal–organic framework porous nanocrystals. *Chem. Sci.* 2019, *10* (41), 9396-9408.

63. Marshall, C. R.; Dvorak, J. P.; Twight, L. P.; Chen, L.; Kadota, K.; Andreeva, A. B.; Overland, A. E.; Ericson, T.; Cozzolino, A. F.; Brozek, C. K., Size-dependent properties of solution-processable conductive MOF nanocrystals. *J. Am. Chem. Soc.* 2022, *144* (13), 5784-5794.

64. Wu, X.; Niu, M.; Tian, X.; Peng, X.; Buenconsej, P. J. S.; Wu, X.; Wang, Y.; Ji, W.; Li, Y.; Qiao, J., Solution-processable $Ni_3(HITP)_2$/MXene heterostructures for ppb-level gas detection. *J. Mater. Chem. A* 2024, *12* (28), 17382-17394.

65. Wang, Z.; Wang, G.; Qi, H.; Wang, M.; Wang, M.; Park, S.; Wang, H.; Yu, M.; Kaiser, U.; Fery, A., Ultrathin two-dimensional conjugated metal–organic framework single-crystalline nanosheets enabled by surfactant-assisted synthesis. *Chem. Sci.* 2020, *11* (29), 7665-7671.

66. Knebel, A.; Bavykina, A.; Datta, S. J.; Sundermann, L.; Garzon-Tovar, L.; Lebedev, Y.; Durini, S.; Ahmad, R.; Kozlov, S. M.; Shterk, G., Solution processable metal–organic

frameworks for mixed matrix membranes using porous liquids. *Nat. Mater.* 2020, *19* (12), 1346-1353.

67. Jo, Y.-M.; Lim, K.; Yoon, J. W.; Jo, Y. K.; Moon, Y. K.; Jang, H. W.; Lee, J.-H., Visible-light-activated type II heterojunction in Cu_3(hexahydroxytriphenylene)$_2$/Fe_2O_3 hybrids for reversible NO_2 sensing: critical role of π–π* transition. *ACS Cent. Sci.* 2021, *7* (7), 1176-1182.

68. Zuo, Q.; Liu, T.; Chen, C.; Ji, Y.; Gong, X.; Mai, Y.; Zhou, Y., Ultrathin metal–organic framework nanosheets with ultrahigh loading of single Pt atoms for efficient visible-light-driven photocatalytic H_2 evolution. *Angew. Chem., Int. Ed.* 2019, *58* (30), 10198-10203.

69. Park, S.; Zhang, Z.; Qi, H.; Liang, B.; Mahmood, J.; Noh, H.-J.; Hambsch, M.; Wang, M.; Wang, M.; Ly, K. H., In-Plane Oriented Two-Dimensional Conjugated Metal–Organic Framework Films for High-Performance Humidity Sensing. *ACS Mater. Lett.* 2022, *4* (6), 1146-1153.

70. Smith, M. K.; Jensen, K. E.; Pivak, P. A.; Mirica, K. A., Direct Self-Assembly of Conductive Nanorods of Metal–Organic Frameworks into Chemiresistive Devices on Shrinkable Polymer Films. *Chem. Mater.* 2016, *28* (15), 5264-5268.

71. Smith, M. K.; Mirica, K. A., Self-Organized Frameworks on Textiles (SOFT): Conductive Fabrics for Simultaneous Sensing, Capture, and Filtration of Gases. *J. Am. Chem. Soc.* 2017, *139* (46), 16759-16767.

72. Yao, M. S.; Lv, X. J.; Fu, Z. H.; Li, W. H.; Deng, W. H.; Wu, G. D.; Xu, G., Layer-by-Layer Assembled Conductive Metal-Organic Framework Nanofilms for Room-Temperature Chemiresistive Sensing. *Angew. Chem., Int. Ed.* 2017, *56* (52), 16510-16514.

73. Ikigaki, K.; Okada, K.; Tokudome, Y.; Toyao, T.; Falcaro, P.; Doonan, C. J.; Takahashi, M., MOF-on-MOF: Oriented Growth of Multiple Layered Thin Films of Metal-Organic Frameworks. *Angew. Chem., Int. Ed.* 2019, *58* (21), 6886-6890.

74. Wu, A.-Q.; Wang, W.-Q.; Zhan, H.-B.; Cao, L.-A.; Ye, X.-L.; Zheng, J.-J.; Kumar, P. N.; Chiranjeevulu, K.; Deng, W.-H.; Wang, G.-E.; Yao, M.-S.; Xu, G., Layer-by-layer assembled dual-ligand conductive MOF nano-films with modulated chemiresistive sensitivity and selectivity. *Nano Res.* 2020, *14* (2), 438-443.

75. Makiura, R.; Motoyama, S.; Umemura, Y.; Yamanaka, H.; Sakata, O.; Kitagawa, H., Surface nano-architecture of a metal-organic framework. *Nat. Mater.* 2010, *9* (7), 565-571.

76. Liu, Y.; Wei, Y.; Liu, M.; Bai, Y.; Wang, X.; Shang, S.; Chen, J.; Liu, Y., Electrochemical Synthesis of Large Area Two-Dimensional Metal-Organic Framework Films on Copper Anodes. *Angew. Chem., Int. Ed.* 2021, *60* (6), 2887-2891.

77. de Lourdes Gonzalez-Juarez, M.; Flores, E.; Martin-Gonzalez, M.; Nandhakumar, I.; Bradshaw, D., Electrochemical deposition and thermoelectric characterisation of a semiconducting 2D metal–organic framework thin film. *J. Mater. Chem. A* 2020, *8* (26), 13197-13206.

78. Campagnol, N.; Van Assche, T.; Boudewijns, T.; Denayer, J.; Binnemans, K.; De Vos, D.; Fransaer, J., High pressure, high temperature electrochemical synthesis of metal–organic frameworks: films of MIL-100 (Fe) and HKUST-1 in different morphologies. *J. Mater. Chem. A* 2013, *1* (19).

79. Zhao, M.; Huang, Y.; Peng, Y.; Huang, Z.; Ma, Q.; Zhang, H., Two-dimensional metal–organic framework nanosheets: synthesis and applications. *Chem. Soc. Rev.* 2018, *47* (16), 6267-6295.

80. Rubio-Gimenez, V.; Galbiati, M.; Castells-Gil, J.; Almora-Barrios, N.; Navarro-Sanchez, J.; Escorcia-Ariza, G.; Mattera, M.; Arnold, T.; Rawle, J.; Tatay, S.; Coronado, E.; Marti-Gastaldo, C., Bottom-Up Fabrication of Semiconductive Metal-Organic Framework Ultrathin Films. *Adv. Mater.* 2018, *30* (10).

81. Zheng, R.; Fu, Z.-H.; Deng, W.-H.; Wen, Y.; Wu, A.-Q.; Ye, X.-L.; Xu, G., The Growth Mechanism of a Conductive MOF Thin Film in Spray-based Layer-by-layer Liquid Phase Epitaxy. *Angew. Chem., Int. Ed.* 2022, *61*, e202212797-e202212803.

82. Zhang, X.; Wan, K.; Subramanian, P.; Xu, M.; Luo, J.; Fransaer, J., Electrochemical deposition of metal–organic framework films and their applications. *J. Mater. Chem. A* 2020, *8* (16), 7569-7587.

83. Liu, Y.; Wei, Y.; Liu, M.; Bai, Y.; Wang, X.; Shang, S.; Chen, J.; Liu, Y., Electrochemical Synthesis of Large Area Two-Dimensional Metal–Organic Framework Films on Copper Anodes. *Angew. Chem., Int. Ed.* 2021, *60* (6), 2887-2891.

84. Yao, M.-S.; Otake, K.-i.; Koganezawa, T.; Ogasawara, M.; Asakawa, H.; Tsujimoto, M.; Xue, Z.-Q.; Li, Y.-H.; Flanders, N. C.; Wang, P., Growth mechanisms and anisotropic softness–dependent conductivity of orientation-controllable metal–organic framework nanofilms. *Proc. Natl. Acad. Sci.* 2023, *120* (40), e2305125120-e2305125127.

85. Stodolka, M.; Choi, J. Y.; Fang, X.; Lu, C.; Pham, H. T.; Check, B.; Park, J., Electrosynthesis of a Nickel-Based Conductive Metal–Organic Framework with Controlled Morphology for Enhanced Capacitance. *ACS Materials Letters* 2023, *6* (1), 49-55.

86. Li, M.; Dinca, M., Reductive electrosynthesis of crystalline metal–organic frameworks. *J. Am. Chem. Soc.* 2011, *133* (33), 12926-12929.

87. Xie, S.; Zhou, Z.; Zhang, X.; Fransaer, J., Cathodic deposition of MOF films: mechanism and applications. *Chem. Soc. Rev.* 2023, *52* (13), 4292-4312.

88. Stock, N.; Biswas, S., Synthesis of metal-organic frameworks (MOFs): routes to various MOF topologies, morphologies, and composites. *Chem. Rev.* 2012, *112* (2), 933-969.

89. Ma, Z.-Z.; Li, Q.-H.; Wang, Z.; Gu, Z.-G.; Zhang, J., Electrically regulating nonlinear optical limiting of metal-organic framework film. *Nat. Commun.* 2022, *13* (1), 6347-6356.

90. Mähringer, A.; Jakowetz, A. C.; Rotter, J. M.; Bohn, B. J.; Stolarczyk, J. K.; Feldmann, J.; Bein, T.; Medina, D. D., Oriented thin films of electroactive triphenylene catecholate-based two-dimensional metal–organic frameworks. *ACS nano* 2019, *13* (6), 6711-6719.

91. Chon, S.; Nakayama, R.; Iwamoto, S.; Kobayashi, S.; Shimizu, R.; Hitosugi, T., Orientation Control of a Two-Dimensional Conductive Metal–Organic Framework Thin Film by a Pyridine Vapor-Assisted Dry Process. *ACS Appl. Mater. Interfaces.* 2023, *15* (48), 56057-56063.

92. Shin, S. H. R.; Tao, J.; Canfield, N. L.; Bowden, M. E.; Heo, J.; Li, D.; Liu, J.; De Yoreo, J. J.; Thallapally, P. K.; Sushko, M. L., Self-Assembly and Oriented Growth of Conductive Ni-CAT-1 Metal-Organic Framework at Solid–Liquid Interfaces. *Adv. Mater. Interf.* 2023, *10* (4), 2202031-2202039.

93. Shin, S. H. R.; Tao, J.; Canfield, N. L.; Bowden, M. E.; Liu, L.; Sivakumar, B. M.; Liu, J.; De Yoreo, J. J.; Thallapally, P. K.; Sushko, M. L., Role of Solvent in the Oriented Growth of Conductive Ni-CAT-1 Metal-Organic Framework at Solid–Liquid Interfaces. *Adv. Mater. Interfaces* 2024, 2301009.

94. Naidek, K. P.; Zuconelli, C. R.; Cruz, O. M.; Ribeiro, R.; Winnischofer, S. M.; Winnischofer, H., Characterization of 2, 3, 6, 7, 10, 11-hexahydroxytriphenylene and its effects on cell viability in human cancer cell lines. *Biochem. Cell Biol.* 2016, *94* (2), 205-211.

95. Wang, Z.; Walter, L. S.; Wang, M.; Petkov, P. S.; Liang, B.; Qi, H.; Nguyen, N. N.; Hambsch, M.; Zhong, H.; Wang, M., Interfacial Synthesis of Layer-Oriented 2D Conjugated Metal–Organic Framework Films toward Directional Charge Transport. *J. Am. Chem. Soc.* 2021, *143* (34), 13624-13632.

96. Liu, J.; Chen, Y.; Huang, X.; Ren, Y.; Hambsch, M.; Bodesheim, D.; Pohl, D.; Li, X.; Deconinck, M.; Zhang, B., On-liquid-gallium surface synthesis of ultrasmooth thin films of conductive metal–organic frameworks. *Nat. Synth.* 2024, 715-726.

97. Potyrailo, R. A., Multivariable Sensors for Ubiquitous Monitoring of Gases in the Era of Internet of Things and Industrial Internet. *Chem. Rev.* 2016, *2016 v.116 no.19* (no. 19), pp. 11877-11923.

98. Meng, Z.; Stolz, R. M.; Mendecki, L.; Mirica, K. A., Electrically-Transduced Chemical Sensors Based on Two-Dimensional Nanomaterials. *Chem. Rev.* 2019, *119* (1), 478-598.

99. Schroeder, V.; Savagatrup, S.; He, M.; Lin, S.; Swager, T. M., Carbon Nanotube Chemical Sensors. *Chem Rev* 2019, *119* (1), 599-663.

100. Fennell, J. F., Jr.; Liu, S. F.; Azzarelli, J. M.; Weis, J. G.; Rochat, S.; Mirica, K. A.; Ravnsbaek, J. B.; Swager, T. M., Nanowire Chemical/Biological Sensors: Status and a Roadmap for the Future. *Angew. Chem., Int. Ed.* 2016, *55* (4), 1266-81.

101. Jo, Y. M.; Jo, Y. K.; Lee, J. H.; Jang, H. W.; Hwang, I. S.; Yoo, D. J., MOF-based chemiresistive gas sensors: toward new functionalities. *Adv. Mater.* 2023, *35* (43), 2206842.

102. Chen, L.; Yu, Q.; Pan, C.; Song, Y.; Dong, H.; Xie, X.; Li, Y.; Liu, J.; Wang, D.; Chen, X., Chemiresistive gas sensors based on electrospun semiconductor metal oxides: A review. *Talanta* 2022, *246*, 123527.

103. Joshi, N.; Hayasaka, T.; Liu, Y.; Liu, H.; Oliveira, O. N., Jr.; Lin, L., A review on chemiresistive room temperature gas sensors based on metal oxide nanostructures, graphene and 2D transition metal dichalcogenides. *Mikrochim Acta* 2018, *185* (4), 213.

104. Yuan, H.; Tao, J.; Li, N.; Karmakar, A.; Tang, C.; Cai, H.; Pennycook, S. J.; Singh, N.; Zhao, D., On-Chip Tailorability of Capacitive Gas Sensors Integrated with Metal-Organic Framework Films. *Angew. Chem., Int. Ed.* 2019, *58* (40), 14089-14094.

105. Park, J.; Hinckley, A. C.; Huang, Z.; Feng, D.; Yakovenko, A. A.; Lee, M.; Chen, S.; Zou, X.; Bao, Z., Synthetic routes for a 2D semiconductive copper hexahydroxybenzene metal–organic framework. *J. Am. Chem. Soc.* 2018, *140* (44), 14533-14537.

106. Benedetto, G.; Mirica, K. A., Conductive Framework Materials for Chemiresistive Detection and Differentiation of Toxic Gases. *Accounts of Chemical Research* 2024, 16759-16767.

107. Lin, Y.; Li, W. H.; Wen, Y.; Wang, G. E.; Ye, X. L.; Xu, G., Layer-by-Layer Growth of Preferred-Oriented MOF Thin Film on Nanowire Array for High-Performance Chemiresistive Sensing. *Angewandte Chemie International Edition* 2021, *60* (49), 25758-25761.

108. Campbell, M. G.; Liu, S. F.; Swager, T. M.; Dinca, M., Chemiresistive Sensor Arrays from Conductive 2D Metal-Organic Frameworks. *J Am Chem Soc* 2015, *137* (43), 13780-3.

109. Eagleton, A. M.; Ko, M.; Stolz, R. M.; Vereshchuk, N.; Meng, Z.; Mendecki, L.; Levenson, A. M.; Huang, C.; MacVeagh, K. C.; Mahdavi-Shakib, A., Fabrication of Multifunctional Electronic Textiles Using Oxidative Restructuring of Copper into a Cu-Based Metal–Organic Framework. *J. Am. Chem. Soc.* 2022, *144* (51), 23297-23312.

110. Stolz, R. M.; Mahdavi-Shakib, A.; Frederick, B. G.; Mirica, K. A., Host–Guest Interactions and Redox Activity in Layered Conductive Metal–Organic Frameworks. *Chem. Mater.* 2020, *32* (18), 7639-7652.

111. Stassen, I.; Dou, J. H.; Hendon, C.; Dinca, M., Chemiresistive Sensing of Ambient CO2 by an Autogenously Hydrated Cu3(hexaiminobenzene)2 Framework. *ACS Cent Sci* 2019, *5* (8), 1425-1431.

112. Rubio-Gimenez, V.; Almora-Barrios, N.; Escorcia-Ariza, G.; Galbiati, M.; Sessolo, M.; Tatay, S.; Marti-Gastaldo, C., Origin of the Chemiresistive Response of Ultrathin Films of Conductive Metal-Organic Frameworks. *Angew Chem Int Ed Engl* 2018, *57* (46), 15086-15090.

113. Aykanat, A.; Meng, Z.; Stolz, R. M.; Morrell, C. T.; Mirica, K. A., Bimetallic Two-Dimensional Metal–Organic Frameworks for the Chemiresistive Detection of Carbon Monoxide. *Angewandte Chemie International Edition* 2022, *61* (6), e202113665.

114. Yao, M. S.; Zheng, J. J.; Wu, A. Q.; Xu, G.; Nagarkar, S. S.; Zhang, G.; Tsujimoto, M.; Sakaki, S.; Horike, S.; Otake, K.; Kitagawa, S., A Dual-Ligand Porous Coordination Polymer Chemiresistor with Modulated Conductivity and Porosity. *Angew Chem Int Ed Engl* 2020, *59* (1), 172-176.

115. Dong, R.; Zhang, Z.; Tranca, D. C.; Zhou, S.; Wang, M.; Adler, P.; Liao, Z.; Liu, F.; Sun, Y.; Shi, W., A coronene-based semiconducting two-dimensional metal-organic framework with ferromagnetic behavior. *Nature communications* 2018, *9* (1), 2637.

116. Stoll, S.; Goldfarb, D., *EPR spectroscopy: fundamentals and methods*. John Wiley & Sons: 2018.

117. Ugale, A.; Ninawe, P.; Jain, A.; Sangole, M.; Mandal, R.; Singh, K.; Ballav, N., Intertwining of Localized (d) and Delocalized (π) Spins in Magnetically Frustrated Two-Dimensional Metal–Organic Frameworks. *Inorganic Chemistry* 2024, *63* (8), 3675-3681.

118. Bon, V.; Brunner, E.; Pöppl, A.; Kaskel, S., Unraveling structure and dynamics in porous frameworks via advanced in situ characterization techniques. *Advanced Functional Materials* 2020, *30* (41), 1907847.

119. Chen, Q.; Adeniran, O.; Liu, Z.-F.; Zhang, Z.; Awaga, K., Graphite-like charge storage mechanism in a 2D π–d conjugated metal–organic framework revealed by stepwise magnetic monitoring. *J. Am. Chem. Soc.* 2023, *145* (2), 1062-1071.

120. Slota, M.; Keerthi, A.; Myers, W. K.; Tretyakov, E.; Baumgarten, M.; Ardavan, A.; Sadeghi, H.; Lambert, C. J.; Narita, A.; Müllen, K., Magnetic edge states and coherent manipulation of graphene nanoribbons. *Nature* 2018, *557* (7707), 691-695.

121. Graham, M. J.; Zadrozny, J. M.; Fataftah, M. S.; Freedman, D. E., Forging solid-state qubit design principles in a molecular furnace. *Chem. Mater.* 2017, *29* (5), 1885-1897.

122. Schweiger, A.; Jeschke, G., *Principles of pulse electron paramagnetic resonance*. Oxford university press: 2001.

123. Mirzoyan, R.; Kazmierczak, N. P.; Hadt, R. G., Deconvolving contributions to decoherence in molecular electron spin qubits: a dynamic ligand field approach. *Chem. Eur. J.* 2021, *27* (37), 9482-9494.

124. Lombardi, F.; Lodi, A.; Ma, J.; Liu, J.; Slota, M.; Narita, A.; Myers, W. K.; Müllen, K.; Feng, X.; Bogani, L., Quantum units from the topological engineering of molecular graphenoids. *Science* 2019, *366* (6469), 1107-1110.

125. Amdur, M. J.; Mullin, K. R.; Waters, M. J.; Puggioni, D.; Wojnar, M. K.; Gu, M.; Sun, L.; Oyala, P. H.; Rondinelli, J. M.; Freedman, D. E., Chemical control of spin–lattice relaxation to discover a room temperature molecular qubit. *Chem. Sci.* 2022, *13* (23), 7034-7045.

126. Chen, J.-S.; Trerayapiwat, K. J.; Sun, L.; Krzyaniak, M. D.; Wasielewski, M. R.; Rajh, T.; Sharifzadeh, S.; Ma, X., Long-lived electronic spin qubits in single-walled carbon nanotubes. *Nat. Commun.* 2023, *14* (1), 848.

127. Gaita-Ariño, A.; Luis, F.; Hill, S.; Coronado, E., Molecular spins for quantum computation. *Nat. Chem.* 2019, *11* (4), 301-309.

128. Zadrozny, J. M.; Niklas, J.; Poluektov, O. G.; Freedman, D. E., Millisecond coherence time in a tunable molecular electronic spin qubit. *ACS Cent. Sci.* 2015, *1* (9), 488-492.

129. Yu, C.-J.; Krzyaniak, M. D.; Fataftah, M. S.; Wasielewski, M. R.; Freedman, D. E., A concentrated array of copper porphyrin candidate qubits. *Chem. Sci.* 2019, *10* (6), 1702-1708.

130. Jellen, M. J.; Ayodele, M. J.; Cantu, A.; Forbes, M. D.; Garcia-Garibay, M. A., 2D arrays of organic qubit candidates embedded into a pillared-paddlewheel metal–organic framework. *J. Am. Chem. Soc.* 2020, *142* (43), 18513-18521.

131. Oanta, A. K.; Collins, K. A.; Evans, A. M.; Pratik, S. M.; Hall, L. A.; Strauss, M. J.; Marder, S. R.; D'Alessandro, D. M.; Rajh, T.; Freedman, D. E., Electronic Spin Qubit Candidates Arrayed within Layered Two-Dimensional Polymers. *J. Am. Chem. Soc.* 2022, *145* (1), 689-696.

132. Zadrozny, J. M.; Gallagher, A. T.; Harris, T. D.; Freedman, D. E., A porous array of clock qubits. *J. Am. Chem. Soc.* 2017, *139* (20), 7089-7094.

133. Yamabayashi, T.; Atzori, M.; Tesi, L.; Cosquer, G.; Santanni, F.; Boulon, M.-E.; Morra, E.; Benci, S.; Torre, R.; Chiesa, M., Scaling up electronic spin qubits into a three-dimensional metal–organic framework. *J. Am. Chem. Soc.* 2018, *140* (38), 12090-12101.

134. Bader, K.; Winkler, M.; van Slageren, J., Tuning of molecular qubits: very long coherence and spin–lattice relaxation times. *Chem. Commun.* 2016, *52* (18), 3623-3626.

135. Follmer, A. H.; Ribson, R. D.; Oyala, P. H.; Chen, G. Y.; Hadt, R. G., Understanding covalent versus spin–orbit coupling contributions to temperature-dependent electron spin relaxation in cupric and vanadyl phthalocyanines. *J. Phys. Chem. A* 2020, *124* (44), 9252-9260.

136. Urtizberea, A.; Natividad, E.; Alonso, P. J.; Andrés, M. A.; Gascón, I.; Goldmann, M.; Roubeau, O., A porphyrin spin qubit and its 2D framework nanosheets. *Adv. Funct. Mater.* 2018, *28* (31), 1801695-1801700.

137. Faust, T. B.; D'Alessandro, D. M., Radicals in metal–organic frameworks. *Rsc Adv.* 2014, *4* (34), 17498-17512.

138. Dou, J. H.; Arguilla, M. Q.; Luo, Y.; Li, J.; Zhang, W.; Sun, L.; Mancuso, J. L.; Yang, L.; Chen, T.; Parent, L. R.; Skorupskii, G.; Libretto, N. J.; Sun, C.; Yang, M. C.; Dip, P. V.; Brignole, E. J.; Miller, J. T.; Kong, J.; Hendon, C. H.; Sun, J.; Dinca, M., Atomically precise single-crystal structures of electrically conducting 2D metal-organic frameworks. *Nat Mater* 2021, *20* (2), 222-228.

139. Lu, Y.; Zhang, Y.; Yang, C.-Y.; Revuelta, S.; Qi, H.; Huang, C.; Jin, W.; Li, Z.; Vega-Mayoral, V.; Liu, Y., Precise tuning of interlayer electronic coupling in layered conductive metal-organic frameworks. *Nature communications* 2022, *13* (1), 7240.

140. Xing, G.; Liu, J.; Zhou, Y.; Fu, S.; Zheng, J.-J.; Su, X.; Gao, X.; Terasaki, O.; Bonn, M.; Wang, H. I., Conjugated Nonplanar Copper-Catecholate Conductive Metal–Organic

Frameworks via Contorted Hexabenzocoronene Ligands for Electrical Conduction. *Journal of the American Chemical Society* 2023, *145* (16), 8979-8987.

141. Lu, Y.; Hu, Z.; Petkov, P.; Fu, S.; Qi, H.; Huang, C.; Liu, Y.; Huang, X.; Wang, M.; Zhang, P., Tunable Charge Transport and Spin Dynamics in Two-Dimensional Conjugated Metal–Organic Frameworks. *J. Am. Chem. Soc.* 2024, *146* (4), 2574-2582.

142. Orihashi, K.; Yamauchi, A.; Inoue, M.; Parmar, B.; Fujiwara, S.; Kimizuka, N.; Asada, M.; Nakamura, T.; Yanai, N., Radical qubits photo-generated in acene-based metal–organic frameworks. *Dalton Trans.* 2024, *53* (3), 872-876.

143. Inoue, M.; Yamauchi, A.; Parmar, B.; Orihashi, K.; Singh, M.; Asada, M.; Nakamura, T.; Yanai, N., Guest-responsive coherence time of radical qubits in a metal–organic framework. *Chem. Commun.* 2024, *60* (48), 6130-6133.

144. Chen, T.; Dou, J.-H.; Yang, L.; Sun, C.; Oppenheim, J. J.; Li, J.; Dincă, M., Dimensionality modulates electrical conductivity in compositionally constant one-, two-, and three-dimensional frameworks. *Journal of the American Chemical Society* 2022, *144* (12), 5583-5593.

145. Huang, X.; Li, Y.; Fu, S.; Ma, C.; Lu, Y.; Wang, M.; Zhang, P.; Li, Z.; He, F.; Huang, C., Control of the Hydroquinone/Benzoquinone Redox State in High-Mobility Semiconducting Conjugated Coordination Polymers. *Angewandte Chemie International Edition* 2024, e202320091.

146. Wang, L.; Sarkar, A.; Grocke, G. L.; Laorenza, D. W.; Cheng, B.; Ritchhart, A.; Filatov, A. S.; Patel, S. N.; Gagliardi, L.; Anderson, J. S., Broad electronic modulation of two-dimensional metal–organic frameworks over four distinct redox states. *Journal of the American Chemical Society* 2023, *145* (15), 8486-8497.

147. Wang, L.; Daru, A.; Jangid, B.; Chen, J.-H.; Jiang, N.; Patel, S. N.; Gagliardi, L.; Anderson, J. S., Aliovalent Substitution Tunes Physical Properties in a Conductive Bis

(dithiolene) Two-Dimensional Metal–Organic Framework. *Journal of the American Chemical Society* 2024, *146* (17), 12063-12073.

148. Wang, L.; Papoular, R. J.; Horwitz, N. E.; Xie, J.; Sarkar, A.; Campisi, D.; Zhao, N.; Cheng, B.; Grocke, G. L.; Ma, T., Linker Redox Mediated Control of Morphology and Properties in Semiconducting Iron-Semiquinoid Coordination Polymers. *Angew. Chem., Int. Ed.* 2022, *61* (45), e202207834.

149. Park, J.; Hinckley, A. C.; Huang, Z.; Chen, G.; Yakovenko, A. A.; Zou, X.; Bao, Z., High thermopower in a Zn-based 3D semiconductive metal–organic framework. *Journal of the American Chemical Society* 2020, *142* (49), 20531-20535.

150. Wu, X.; Qiu, Y.; Chen, Z.; Guan, B.; Hao, X.; Rykov, A. I.; Sun, Y.; Liu, L.; Zou, Y.; Sun, J., Paramagnetic Conducting Metal–Organic Frameworks with Three-Dimensional Structure. *Angewandte Chemie International Edition* 2020, *59* (47), 20873-20878.

151. Fan, K.; Fu, C.; Chen, Y.; Zhang, C.; Zhang, G.; Guan, L.; Mao, M.; Ma, J.; Hu, W.; Wang, C., Framework dimensional control boosting charge storage in conjugated coordination polymers. *Advanced Science* 2023, *10* (5), 2205760.

152. Zhang, Y.; Dong, L.-Z.; Li, S.; Huang, X.; Chang, J.-N.; Wang, J.-H.; Zhou, J.; Li, S.-L.; Lan, Y.-Q., Coordination environment dependent selectivity of single-site-Cu enriched crystalline porous catalysts in CO_2 reduction to CH_4. *Nat. Commun.* 2021, *12* (1), 1-9.

153. Nath, A.; Asha, K.; Mandal, S., Conductive Metal-Organic Frameworks: Electronic Structure and Electrochemical Applications. *Chem. Eur. J.* 2021, *27* (45), 11482-11538.

154. Qi, M.; Zhou, Y.; Lv, Y.; Chen, W.; Su, X.; Zhang, T.; Xing, G.; Xu, G.; Terasaki, O.; Chen, L., Direct construction of 2d conductive metal–organic frameworks from a nonplanar ligand: in situ scholl reaction and topological modulation. *J. Am. Chem. Soc.* 2022, *145* (5), 2739-2744.

155. Su, X.; Zhong, Z.; Yan, X.; Zhang, T.; Wang, C.; Wang, Y. X.; Xu, G.; Chen, L., Facile Synthesis of Metallosalphen-Based 2D Conductive Metal-Organic Frameworks for NO2 Sensing: Metal Coordination Induced Planarization. *Angewandte Chemie International Edition* 2023, *62* (22), e202302645.

156. Zhang, J.; Zhou, G.; Un, H.-I.; Zheng, F.; Jastrzembski, K.; Wang, M.; Guo, Q.; Mücke, D.; Qi, H.; Lu, Y., Wavy Two-Dimensional Conjugated Metal–Organic Framework with Metallic Charge Transport. *Journal of the American Chemical Society* 2023, *145* (43), 23630-23638.

157. Sengupta, D.; Melix, P.; Bose, S.; Duncan, J.; Wang, X.; Mian, M. R.; Kirlikovali, K. O.; Joodaki, F.; Islamoglu, T.; Yildirim, T., Air-stable Cu (I) metal–organic framework for hydrogen storage. *Journal of the American Chemical Society* 2023, *145* (37), 20492-20502.

158. Yabuuchi, Y.; Furukawa, H.; Carsch, K. M.; Klein, R. A.; Tkachenko, N. V.; Huang, A. J.; Cheng, Y.; Taddei, K. M.; Novak, E.; Brown, C. M., Geometric Tuning of Coordinatively Unsaturated Copper (I) Sites in Metal–Organic Frameworks for Ambient-Temperature Hydrogen Storage. *Journal of the American Chemical Society* 2024.

159. Bard, A. J.; Faulkner, L. R.; White, H. S., *Electrochemical methods: fundamentals and applications*. John Wiley & Sons: 2022.

160. Rafiee, M.; Abrams, D. J.; Cardinale, L.; Goss, Z.; Romero-Arenas, A.; Stahl, S. S., Cyclic voltammetry and chronoamperometry: mechanistic tools for organic electrosynthesis. *Chemical Society Reviews* 2024.

161. Li, W.; Lefferts, M. J.; Wang, Y.; Lister, A. M.; Forssberg, A.; Chen, R.; Wang, L.; Castell, M. R., Chemiresistive Polymer Percolation Network Gas Sensor Created with a Nanosphere Template. *Advanced Materials Interfaces* 2023, *10* (8), 2202042.

162. Egerton, R. F., *Physical principles of electron microscopy*. Springer: 2005; Vol. 56.

163. Lanza, M., *Conductive atomic force microscopy: applications in nanomaterials*. John Wiley & Sons: 2017.

164. Speakman, S., Basics of X-ray Diffraction. *Massachusetts Institute of Technology* 2016.

165. Perkampus, H.-H., *UV-VIS Spectroscopy and its Applications*. Springer Science & Business Media: 2013.

166. Sever, M. J.; Wilker, J. J., Visible absorption spectra of metal–catecholate and metal–tironate complexes. *Dalton Trans.* 2004, (7), 1061-1072.

167. Engelhard, M. H.; Droubay, T. C.; Du, Y. *X-ray photoelectron spectroscopy applications*; Pacific Northwest National Lab.(PNNL), Richland, WA (United States …: 2017.

168. Hanna, L.; Lockard, J. V., From IR to x-rays: gaining molecular level insights on metal-organic frameworks through spectroscopy. *Journal of Physics: Condensed Matter* 2019, *31* (48), 483001.

169. Moreno-Pineda, E.; Wernsdorfer, W., Measuring molecular magnets for quantum technologies. *Nature Reviews Physics* 2021, *3* (9), 645-659.

170. Roessler, M. M.; Salvadori, E., Principles and applications of EPR spectroscopy in the chemical sciences. *Chemical Society Reviews* 2018, *47* (8), 2534-2553.

171. Liu, J.; Song, X.; Zhang, T.; Liu, S.; Wen, H.; Chen, L., 2D Conductive Metal-Organic Frameworks: An Emerging Platform for Electrochemical Energy Storage. *Angew Chem Int Ed Engl* 2020.

172. Stolz, R. M.; Kolln, A. F.; Rocha, B. C.; Brinks, A.; Eagleton, A. M.; Mendecki, L.; Vashisth, H.; Mirica, K. A., Epitaxial Self-Assembly of Interfaces of 2D Metal–Organic Frameworks for Electroanalytical Detection of Neurotransmitters. *ACS Nano* 2022, *16*, 13869-13883.

173. Xiao, Y.; Wu, Z.; Zhang, Q.; Li, P.; Yu, H.; Lu, G., Oxygen-assisted cathodic deposition of copper-carboxylate metal–organic framework films. *Cryst. Growth Des.* 2020, *20* (6), 3997-4004.

174. Behboudikhiavi, S.; Chanteux, G.; Babu, B.; Faniel, S.; Marlec, F.; Robert, K.; Magnin, D.; Lucaccioni, F.; Omale, J. O.; Apostol, P., Direct Electrodeposition of Electrically Conducting $Ni_3(HITP)_2$ MOF Nanostructures for Micro-Supercapacitor Integration. *Small* 2024, 2401509.

175. Han, J.; He, X.; Liu, J.; Ming, R.; Lin, M.; Li, H.; Zhou, X.; Deng, H., Determining factors in the growth of MOF single crystals unveiled by in situ interface imaging. *Chem* 2022.

176. Gu, F.; Shu, S.; Patrick, C. E.; Castell, M. R., Scanning Tunneling Microscopy of Bimetallic Ni/Co-HITP Metal–Organic Framework Monolayers. *The Journal of Physical Chemistry C* 2024.

177. Gerke, R. H., A Summary of Electrode Potentials. *Chemical Reviews* 1925, *1* (4), 377-395.

178. Zhou, S.; Shekhah, O.; Jia, J.; Czaban-Jóźwiak, J.; Bhatt, P. M.; Ramírez, A.; Gascon, J.; Eddaoudi, M., Electrochemical synthesis of continuous metal–organic framework membranes for separation of hydrocarbons. *Nature Energy* 2021, *6* (9), 882-891.

179. de Lourdes Gonzalez-Juarez, M.; Flores, E.; Martin-Gonzalez, M.; Nandhakumar, I.; Bradshaw, D., Electrochemical deposition and thermoelectric characterisation of a semiconducting 2-D metal–organic framework thin film. *Journal of Materials Chemistry A* 2020, *8* (26), 13197-13206.

180. Giannazzo, F.; Greco, G.; Roccaforte, F.; Mahata, C.; Lanza, M., *Electrical Atomic Force Microscopy for Nanoelectronics*. 2019; p 303-350.

181. Pan, Y.; Sun, W.; Chen, J.; Lin, Y.; Chen, Y.-J.; Wen, Z.; Xu, G., Mass transport control over a conductive MOF 3D thin film to improve gas sensing. *Journal of Materials Chemistry A* 2024, *12* (39), 26902-26908.

182. Yao, M. S.; Lv, X. J.; Fu, Z. H.; Li, W. H.; Deng, W. H.; Wu, G. D.; Xu, G., Layer-by-layer assembled conductive metal–organic framework nanofilms for room-temperature chemiresistive sensing. *Angewandte Chemie* 2017, *129* (52), 16737-16741.

183. Lee, T.; Kim, J. O.; Park, C.; Kim, H.; Kim, M.; Park, H.; Kim, I.; Ko, J.; Pak, K.; Choi, S. Q., Large-area synthesis of ultrathin, flexible, and transparent conductive metal–organic framework thin films via a microfluidic-based solution shearing process. *Advanced Materials* 2022, *34* (12), 2107696.

184. Armitage, B. I.; Murugappan, K.; Lefferts, M. J.; Cowsik, A.; Castell, M. R., Conducting polymer percolation gas sensor on a flexible substrate. *Journal of Materials Chemistry C* 2020, *8* (36), 12669-12676.

185. Huang, C.; Shang, X.; Zhou, X.; Zhang, Z.; Huang, X.; Lu, Y.; Wang, M.; Löffler, M.; Liao, Z.; Qi, H., Hierarchical conductive metal-organic framework films enabling efficient interfacial mass transfer. *Nature Communications* 2023, *14* (1), 3850.

186. Wang, L.; Xu, F.; Zhang, C.; Wageh, S.; Al-Hartomy, O. A.; Zhang, B.; Yang, T.; Zhang, H., Chemiresistive gas sensor based on Mo0. 5W0. 5S2 alloy nanoparticles with good selectivity and ppb-level limit of detection to ammonia. *Microchimica Acta* 2023, *190* (8), 283.

187. Meng, Z.; Stolz, R. M.; De Moraes, L. S.; Jones, C. G.; Eagleton, A. M.; Nelson, H. M.; Mirica, K. A., Gas-Induced Electrical and Magnetic Modulation of Two-Dimensional Conductive Metal–Organic Framework. *Angewandte Chemie International Edition* 2024, e202404290.

188. Sun, C.; Yang, L.; Ortuño, M. A.; Wright, A. M.; Chen, T.; Head, A. R.; López, N.; Dincă, M., Spectroscopic Evidence of Hyponitrite Radical Intermediate in NO

Disproportionation at a MOF-Supported Mononuclear Copper Site. *Angewandte Chemie International Edition* 2021, *60* (14), 7845-7850.

189. Liu, L.; Dong, J.; Liu, J.; Liang, Q.; Song, Y.; Li, W.; Lei, S.; Hu, W., High-Quality Two-Dimensional Metal-Organic Framework Nanofilms for Nonvolatile Memristive Switching. *Small Struct.* 2021, *2* (4), 2000077.

190. Chen, J.; Yang, H.; Fu, H.; He, H.; Zeng, Q.; Li, X., Electrochemical oxidation mechanisms for selective products due to C–O and C–C cleavages of β-O-4 linkages in lignin model compounds. *Physical Chemistry Chemical Physics* 2020, *22* (20), 11508-11518.

191. Jo, Y. M.; Jo, Y. K.; Lee, J. H.; Jang, H. W.; Hwang, I. S.; Yoo, D. J., MOF-based chemiresistive gas sensors: toward new functionalities. *Adv. Mater.* 2023, *35* (43), 2206842-2206873.

192. Ko, M.; Mendecki, L.; Mirica, K. A., Conductive two-dimensional metal-organic frameworks as multifunctional materials. *Chem. Commun.* 2018, *54* (57), 7873-7891.

193. Xiong, D.; Deng, X.; Cao, Z.; Tao, S.; Song, Z.; Xiao, X.; Deng, W.; Hou, H.; Zou, G.; Ji, X., 2D metal–organic frameworks for electrochemical energy storage. *Energy Environ. Mat.* 2023, *6* (6), e12521.

194. Wang, X.; Zhang, X.; He, A.; Guo, J.; Liu, Z., Toward Enhancing Performance of Electromagnetic Wave Absorption for Conductive Metal–Organic Frameworks: Nanostructure Engineering or Crystal Morphology Controlling. *Inorg. Chem.* 2024, *63* (15), 6948-6956.

195. Campbell, M. G.; Sheberla, D.; Liu, S. F.; Swager, T. M.; Dincă, M., Cu_3(hexaiminotriphenylene)$_2$: an electrically conductive 2D metal–organic framework for chemiresistive sensing. *Angew. Chem., Int. Ed.* 2015, *54* (14), 4349-4352.

196. Koo, W. T.; Kim, S. J.; Jang, J. S.; Kim, D. H.; Kim, I. D., Catalytic Metal Nanoparticles Embedded in Conductive Metal-Organic Frameworks for Chemiresistors: Highly Active and Conductive Porous Materials. *Adv. Sci.* 2019, *6* (21), 1900250-1900260.

197. More, M. S.; Bodkhe, G. A.; Singh, F.; Dole, B. N.; Tsai, M.-L.; Hianik, T.; Shirsat, M. D., Chemiresistive and chem-FET Sensor: π-d conjugated metal-organic framework for ultra-sensitive and selective carbon monoxide detection. *Synth. Met.* 2023, *296*.

198. Jo, Y. M.; Lim, K.; Yoon, J. W.; Jo, Y. K.; Moon, Y. K.; Jang, H. W.; Lee, J. H., Visible-Light-Activated Type II Heterojunction in Cu_3(hexahydroxytriphenylene)$_2$/Fe_2O_3 Hybrids for Reversible NO_2 Sensing: Critical Role of pi-pi* Transition. *ACS Cent. Sci.* 2021, *7* (7), 1176-1182.

199. Campbell, M. G.; Liu, S. F.; Swager, T. M.; Dinca, M., Chemiresistive sensor arrays from conductive 2D metal–organic frameworks. *J. Am. Chem. Soc.* 2015, *137* (43), 13780-13783.

200. Park, C.; Baek, J. W.; Shin, E.; Kim, I.-D., Two-Dimensional Electrically Conductive Metal–Organic Frameworks as Chemiresistive Sensors. *ACS Nanoscience Au* 2023, *3* (5), 353-374.

201. Xie, Y.; Wu, X.; Shi, Y.; Peng, Y.; Zhou, H.; Wu, X.; Ma, J.; Jin, J.; Pi, Y.; Pang, H., Recent Progress in 2D Metal-Organic Framework-Related Materials. *Small* 2024, *20* (1), 2305548.

202. Yao, M.-S.; Lv, X.-J.; Fu, Z.-H.; Li, W.-H.; Deng, W.-H.; Wu, G.-D.; Xu, G., Layer-by-Layer Assembled Conductive Metal–Organic Framework Nanofilms for Room-Temperature Chemiresistive Sensing. *Angew. Chem., Int. Ed.* 2017, *56* (52), 16510-16514.

203. Wu, A.-Q.; Wang, W.-Q.; Zhan, H.-B.; Cao, L.-A.; Ye, X.-L.; Zheng, J.-J.; Kumar, P. N.; Chiranjeevulu, K.; Deng, W.-H.; Wang, G.-E.; Yao, M.-S.; Xu, G., Layer-by-layer assembled dual-ligand conductive MOF nano-films with modulated chemiresistive sensitivity and selectivity. *Nano Res.* 2021, *14* (2), 438-443.

204. Mähringer, A.; Jakowetz, A. C.; Rotter, J. M.; Bohn, B. J.; Stolarczyk, J. K.; Feldmann, J.; Bein, T.; Medina, D. D., Oriented Thin Films of Electroactive Triphenylene Catecholate-Based Two-Dimensional Metal–Organic Frameworks. *ACS Nano* 2019, *13* (6), 6711-6719.

205. Li, P.; Shi, X.; Wu, Y.; Song, M.; Lai, Y.; Yu, H.; Lu, G., Cathodic synthesis of a Cu-catecholate metal–organic framework. *CrystEngComm.* 2021, *23* (8), 1828-1835.

206. Song, M.; Jia, J.; Li, P.; Peng, J.; Pang, X.; Qi, M.; Xu, Y.; Chen, L.; Chi, L.; Lu, G., Ligand-Oxidation-Based Anodic Synthesis of Oriented Films of Conductive M-Catecholate Metal–Organic Frameworks with Controllable Thickness. *J. Am. Chem. Soc.* 2023, *145* (47), 25570-25578.

207. Sun, C.; Wang, W.; Mu, X.; Zhang, Y.; Wang, Y.; Ma, C.; Jia, Z.; Zhu, J.; Wang, C., Tuning the Electrical Conductivity of a Flexible Fabric-Based Cu-HHTP Film through a Novel Redox Interaction between the Guest–Host System. *ACS Appl. Mater. Interfaces* 2022, *14* (48), 54266-54275.

208. Zhang, F.; Jiao, C.; Shang, Y.; Cao, S.; Sun, R.; Lu, X.; Yan, Z.; Zeng, J., In Situ Growth of Conductive Metal–Organic Framework onto Cu2O for Highly Selective and Humidity-Independent Hydrogen Sulfide Detection in Food Quality Assessment. *ACS Sensors* 2024, *9* (3), 1310-1320.

209. Chen, X.; Lu, Y.; Dong, J.; Ma, L.; Yi, Z.; Wang, Y.; Wang, L.; Wang, S.; Zhao, Y.; Huang, J.; Liu, Y., Ultrafast In Situ Synthesis of Large-Area Conductive Metal–Organic Frameworks on Substrates for Flexible Chemiresistive Sensing. *ACS Appl. Mater. Interfaces* 2020, *12* (51), 57235-57244.

210. Zhang, W.; Wu, X.; Peng, X.; Tian, Y.; Yuan, H., Solution Processable Metal–Organic Frameworks: Synthesis Strategy and Applications. *Adv. Mater.* 2025, *37* (1), 2412708.

211. Hoppe, B.; Hindricks, K. D. J.; Warwas, D. P.; Schulze, H. A.; Mohmeyer, A.; Pinkvos, T. J.; Zailskas, S.; Krey, M. R.; Belke, C.; König, S.; Fröba, M.; Haug, R. J.; Behrens, P.,

Graphene-like metal–organic frameworks: morphology control, optimization of thin film electrical conductivity and fast sensing applications. *CrystEngComm.* 2018, *20* (41), 6458-6471.

212. Wu, X.; Niu, M.; Tian, X.; Peng, X.; Buenconsej, P. J. S.; Wu, X.; Wang, Y.; Ji, W.; Li, Y.; Qiao, J.; Tao, J.; Zhang, M.; Xiao, S.; Yuan, H., Solution-processable $Ni_3(HITP)_2$/MXene heterostructures for ppb-level gas detection. *J. Mater. Chem. A* 2024, *12* (28), 17382-17394.

213. Wu, X.; Tian, X.; Zhang, W.; Peng, X.; Zhou, S.; Buenconsejo, P. J. S.; Li, Y.; Xiao, S.; Tao, J.; Zhang, M.; Yuan, H., Solution-Processable MOF-on-MOF System Constructed via Template-Assisted Growth for Ultratrace H_2S Detection. *Angew. Chem., Int. Ed.* 2024, (n/a), e202410411-e202410423.

214. Huang, C.; Sun, W.; Jin, Y.; Guo, Q.; Mücke, D.; Chu, X.; Liao, Z.; Chandrasekhar, N.; Huang, X.; Lu, Y.; Chen, G.; Wang, M.; Liu, J.; Zhang, G.; Yu, M.; Qi, H.; Kaiser, U.; Xu, G.; Feng, X.; Dong, R., A General Synthesis of Nanostructured Conductive Metal–Organic Frameworks from Insulating MOF Precursors for Supercapacitors and Chemiresistive Sensors. *Angew. Chem., Int. Ed.* 2024, *63* (3), e202313591-e202313599.

215. Wang, Z.; Wang, G.; Qi, H.; Wang, M.; Wang, M.; Park, S.; Wang, H.; Yu, M.; Kaiser, U.; Fery, A.; Zhou, S.; Dong, R.; Feng, X., Ultrathin two-dimensional conjugated metal–organic framework single-crystalline nanosheets enabled by surfactant-assisted synthesis. *Chem. Sci.* 2020, *11* (29), 7665-7671.

216. Hu, M.-L.; Masoomi, M. Y.; Morsali, A., Template strategies with MOFs. *Coord. Chem. Rev.* 2019, *387*, 415-435.

217. Borodko, Y.; Habas, S. E.; Koebel, M.; Yang, P.; Frei, H.; Somorjai, G. A., Probing the Interaction of Poly (vinylpyrrolidone) with Platinum Nanocrystals by UV− Raman and FTIR. *J. Phys. Chem. B.* 2006, *110* (46), 23052-23059.

218. Zhao, M.; Wang, Y.; Ma, Q.; Huang, Y.; Zhang, X.; Ping, J.; Zhang, Z.; Lu, Q.; Yu, Y.; Xu, H., Ultrathin 2D metal–organic framework nanosheets. *Adv. Mater.* 2015, *27* (45), 7372-7378.

219. Wasielewski, M. R.; Forbes, M. D.; Frank, N. L.; Kowalski, K.; Scholes, G. D.; Yuen-Zhou, J.; Baldo, M. A.; Freedman, D. E.; Goldsmith, R. H.; Goodson III, T., Exploiting chemistry and molecular systems for quantum information science. *Nat. Rev. Chem.* 2020, *4* (9), 490-504.

220. Lunghi, A.; Sanvito, S., How do phonons relax molecular spins? *Sci. Adv.* 2019, *5* (9), eaax7163-7170.

221. Atzori, M.; Sessoli, R., The second quantum revolution: role and challenges of molecular chemistry. *J. Am. Chem. Soc.* 2019, *141* (29), 11339-11352.

222. Monni, N.; Angotzi, M. S.; Oggianu, M.; Sahadevan, S. A.; Mercuri, M. L., Redox-active benzoquinones as challenging “non-innocent” linkers to construct 2D frameworks and nanostructures with tunable physical properties. *J. Mater. Chem. C* 2022, *10* (5), 1548-1572.

223. Liu, Y.-Y.; Zhu, H.-L.; Zhao, Z.-H.; Huang, N.-Y.; Liao, P.-Q.; Chen, X.-M., Insight into the Effect of the d-Orbital Energy of Copper Ions in Metal–Organic Frameworks on the Selectivity of Electroreduction of CO2 to CH4. *Acs Catal.* 2022, *12* (5), 2749-2755.

224. Hussain, G.; Silvester, D. S., Comparison of voltammetric techniques for ammonia sensing in ionic liquids. *Electroanalysis* 2018, *30* (1), 75-83.

225. Baluta, S.; Meloni, F.; Halicka, K.; Szyszka, A.; Zucca, A.; Pilo, M. I.; Cabaj, J., Differential pulse voltammetry and chronoamperometry as analytical tools for epinephrine detection using a tyrosinase-based electrochemical biosensor. *RSC Adv.* 2022, *12* (39), 25342-25353.

226. Scholz, F., Voltammetric techniques of analysis: the essentials. *ChemTexts* 2015, *1* (4), 17.

227. Baluta, S.; Meloni, F.; Halicka, K.; Szyszka, A.; Zucca, A.; Pilo, M. I.; Cabaj, J., Differential pulse voltammetry and chronoamperometry as analytical tools for epinephrine detection using a tyrosinase-based electrochemical biosensor. *RSC advances* 2022, *12* (39), 25342-25353.

228. Pezzella, A.; Crescenzi, O.; Panzella, L.; Napolitano, A.; Land, E. J.; Barone, V.; d'Ischia, M., Free radical coupling of o-semiquinones uncovered. *J. Am. Chem. Soc.* 2013, *135* (32), 12142-12149.

229. Najder-Kozdrowska, L.; Pilawa, B.; Więckowski, A. B.; Buszman, E.; Wrześniok, D., Influence of copper (II) ions on radicals in DOPA–melanin. *Appl. Magn. Reson.* 2009, *36* (1), 81-88.

230. Warner, M.; Din, S.; Tupitsyn, I. S.; Morley, G. W.; Stoneham, A. M.; Gardener, J. A.; Wu, Z.; Fisher, A. J.; Heutz, S.; Kay, C. W., Potential for spin-based information processing in a thin-film molecular semiconductor. *Nature* 2013, *503* (7477), 504-508.

231. Escalera-Moreno, L.; Gaita-Ariño, A.; Coronado, E., Decoherence from dipolar interspin interactions in molecular spin qubits. *Phys. Rev. B* 2019, *100* (6), 064405-064414.